SILICON WAFER-CONTAMINANT INTERACTIONS IN DILUTE HYDROFLUORIC ACID SOLUTIONS AND RELATED FUNDAMENTALS IN COLLOID AND INTERFACE SCIENCE

By

ZHAN CHEN

A DISSERTATION PRESENTED TO THE GRADUATE SCHOOL
OF THE UNIVERSITY OF FLORIDA IN PARTIAL FULFILLMENT
OF THE REQUIREMENTS FOR THE DEGREE OF
DOCTOR OF PHILOSOPHY

UNIVERSITY OF FLORIDA

2000

This work is dedicated to my family

ACKNOWLEDGMENTS

I would like to express my sincere thanks to my advisor, Dr. Rajiv K. Singh, for his guidance, trust, and encouragement during the course of the study. Without his guidance I would be still floundering to find the way; without his trust and encouragement I could not obtain the maximum freedom a student could get to indulge myself in what interests me. I am also grateful to Dr. Cammy R. Abernathy, Dr. Stephen J. Pearton, Dr. Hassan El-Shall and Dr. Dinesh O. Shah for serving as committee members and supervising my study.

I would like to acknowledge Jamie Rhodes who gave me tremendous help during my transition from a Chinese undergraduate student to an American graduate student. I am also grateful to Dr. Kumar and Dr. Craciun for their constant help and instructive discussions. Special thanks are also due to Dr. Sankar of the Department of Aerospace Engineering, who taught me finite element method, and to Dr. Ladd of the Department of Chemical Engineering, who encouraged my challenging the classic treatment on electrostatic interaction in colloid system. I would also like to thank Dr. Rabinovich and Mr. Joshua Adler of the Engineering Research Center, who taught me the surface force measurements with the atomic force microscope and shared their valuable knowledge with me. Dr. Vos of IMEC and Dr. Hobbs of Motorola are highly appreciated for their help on surface metal contamination measurements.

It is always a pleasure to mention the people in our group with whom I shared warm friendship and memorable life. Special thanks are due to them: Anu, Anupam, Deepika, Don, Dong-Gu, Frank, Hui, Joshua, Kyu-Gong, Kyo-Se, Michael, Nabil, Seung-Mahn, Srinivas, Uday, and secretary Margaret.

Financial support of this work by Ashland Chemical Company is greatly appreciated. I would also like to thank Zach and Dr. Gassett of Ashland Chemical Company for providing electronic grade chemicals.

Finally, I wish to convey my sincere gratitude to my parents for encouraging me to pursue graduate study overseas. I would also like to thank Juehua Gao for her support and encouragement on finishing this dissertation.

TABLE OF CONTENTS

Page

ACKNOWLEDGMENTS iii

ABSTRACT viii

CHAPTERS

1 INTRODUCTION 1

2 LITERATURE REVIEW 6

Particle Deposition 6
Metal Contamination 11
Surface Roughening 14

3 MECHANISM AND PREVENTION OF PARTICLE DEPOSITION ONTO SILICON WAFER SURFACE FROM HF SOLUTIONS 24

Introduction 24
Experimental 25
Results and Discussion 27
Summary 33

4 SILICON-SILICON NITRIDE SURFACE INTERACTIONS 41

Introduction 41
Experimental 46
Results and Discussion 47
Summary 69

5 PREFERENTIAL DEPOSITION OF COPPER ONTO SILICON WAFER SURFACE FROM HF SOLUTION 111

Introduction 111
Experimental 114
Results and Discussion 115
Summary 118

6 NOVEL IN SITU TECHNIQUE TO CHARACTERIZE COPPER OUTPLATING FROM HF SOLUTIONS ONTO SILICON SURFACES 129

Introduction 129
Experimental 131
Results and Discussion 132
Summary 138

7 SURFACTANT EFFECTS ON COPPER OUTPLATING ONTO SILICON SURFACE FROM HF SOLUTION 146

Introduction 146
Experimental 148
Results and Discussion 149
Summary 157

8 GENERAL SOLUTION FOR POISSON-BOLTZMANN EQUATION IN SEMI-INFINITE PLANAR SYMMETRY 170

Introduction 170
Methods 174
Results and Discussion 179
Summary 183

9 LIKE-CHARGE ELECTROSTATIC ATTRACTION IN CONFINED COLLOIDAL SYSTEMS 188

Introduction 188
Theory 192
Summary 210

10 CONCLUSIONS AND FUTURE WORK 229

APPENDIX

NOVEL METHOD TO FORM A POROUS SILICON LAYER AND ITS APPLICATION ON COPPER SENSING 235

REFERENCES 245

BIOGRAPHICAL SKETCH 257

Abstract of Dissertation Presented to the Graduate School
of the University of Florida in Partial Fulfillment of the
Requirements for the Degree of Doctor of Philosophy

SILICON WAFER-CONTAMINANT INTERACTIONS IN DILUTE HYDROFLUORIC ACID SOLUTIONS AND RELATED FUNDAMENTALS IN COLLOID AND INTERFACE SCIENCE

By

ZHAN CHEN

December 2000

Chairperson: Dr. Rajiv K. Singh
Major Department: Materials Science and Engineering

With the continuous decrease in device size, it becomes more and more important to have a contamination-free silicon wafer surface. Hydrofluoric acid is inevitably involved in silicon wafer wet cleaning. However, during dilute hydrofluoric acid (DHF) cleaning, particles and noble metals tend to deposit on the silicon wafer surface and the surface roughness could increase. In this study, the mechanisms of particle deposition, noble metal outplating, and the effects of additives were investigated.

Particle deposition from DHF solution onto bare silicon surfaces is due to the large van der Waals interaction between silicon and particles. Additives which can increase electrostatic interaction will reduce particle redeposition, and their effectiveness correlates well with the zeta-potential changes on both silicon surface and particles. Direct force measurements between a silicon surface and a silicon nitride surface reveal

that additives not only change electrostatic interaction, but change adhesion forces of particles on silicon surfaces also.

Nobel metal ions, especially copper ions, tend to deposit on bare silicon surfaces in DHF solution. The nucleation stage of copper deposition is critical and copper preferrentially deposits on surfaces with high defect densities. A novel technique to detect copper outplating in situ was established. Some additives may increase copper deposition due to the formation of copper complex and the subsequent adsorption of the copper complex on silicon surfaces. Some additive reduces copper outplating significantly. Their effects were discussed.

Some fundamental aspects of colloid and interface science have been studied as well, including the approximate and numerical solutions of the electric potential distribution near a planar surface in the presence of highly asymmetric electrolytes. More importantly, the surface interaction in a confined/concentrated system was studied and a theory was established. The mysterious long range attractive force between two like-charged surfaces can be explained explicitly by this theory, and the electrostatic interaction in DLVO theory is just a special case of this theory after confinement is removed.

CHAPTER 1
INTRODUCTION

The development of ultra large-scale integrated circuits (ULSIs) technology is continuously challenged by the presence of various contaminants such as particles, metals and organic molecules. The yield of ULSIs is noticeably low compared to other industrial products. It is mainly due to random structural defects caused by particle adhesion on the wafer. Among all failures, the ones caused by particles increase with the increase of circuit integrity. For 64M DRAM it exceeds 90% of all failures [Hat94] (Figure 1-1). It has been believed that particles with diameters larger than 1/10 of the feature size may cause device failure. Moreover, the hitherto unimportant very low densities of metallic and organic contaminants are coming to exert great influences on device performance [Hat98]. Table 1-1 lists the requirements of metallic contamination [Hen99].

Silicon wafer ultra-clean technology is one of the most critical technologies in ULSI fabrication. RCA cleaning is a conventional wet cleaning process invented 30 years ago [Ker70] and is still widely used now. RCA cleaning basically contains two steps. One is the so called SC-1 step using an ammonium hydroxide and hydrogen peroxide aqueous mixture ($NH_4OH : H_2O_2 : H_2O = 1 : 1 : 5$) at elevated temperatures (70 - 90 °C). It possesses excellent particle removal ability, but it may cause metal ion deposition since the solution is basic. The other step is SC-2 containing a hydrochloride and hydrogen

Table 1-1. Stringent metallic contamination requirements.

Year of introduction	**1997**	**1999**	**2001**	**2003**
Device generation	**250nm**	**180nm**	**150nm**	**130nm**
Wafer				
Diameter (mm)	200	300	300	300
Critical surface metals[a](at/cm^2)	$<2.5\times10^{10}$	$<1.3\times10^{10}$	$<1.0\times10^{10}$	$<7.5\times10^{9}$
Other surface metals[b](at/cm^2)	$<1.0\times10^{11}$	$<1.0\times10^{11}$	$<1.0\times10^{11}$	$<1.0\times10^{11}$
Total bulk ion (at/cm^2)	$<3.0\times10^{10}$	$<1.0\times10^{10}$	$<1.0\times10^{10}$	$<1.0\times10^{10}$
DRAM				
Front end of line				
Critical surface metals[c](at/cm^2)	$<5.0\times10^{9}$	$<4.0\times10^{9}$	$<3.0\times10^{9}$	$<2.0\times10^{9}$
Other surface metals[d](at/cm^2)	$<5.0\times10^{10}$	$<2.5\times10^{10}$	$<2.0\times10^{10}$	$<1.5\times10^{10}$
Back end of line				
Metals[e](at/cm^2)	$<1.0\times10^{11}$	$<5.0\times10^{10}$	$<4.0\times10^{10}$	$<2.0\times10^{10}$
Ultra pure water				
Silica (ppt)	100	50	50	10
Critical metals (ppt)	25	20	15	10
Liquid chemicals				
Fe, Cu in H_2O_2, HF, NH_4OH(ppt, each)	<500	<250	<200	<150
Other metals (ppt, each)	<1000	<500	<400	<300

[a] Ca, Co, Cu, Cr, Fe, K, Mo, Mn, Na, Ni [b] Al, Ti, V, Zn [c] Ca, Co, Cu, Cr, Fe, K, Mo, Mn, Na, Ni, W [d] Al, Ti, V, Zn, Ba, Sr, Ta [e] K, Li, Na

peroxide aqueous mixture, which is used to remove metal ions deposited on the wafer surface. Prior to SC-1 cleaning, a highly oxidizing sulfuric acid and hydrogen peroxide mixture (H_2SO_4 : H_2O_2 = 4 : 1) at 120 - 150°C may be employed to remove organic

residues on wafer surfaces. After SC-2 cleaning, wafers are covered by a thin oxide layer. It is removed by a dilute hydrofluoric acid (DHF) cleaning. These are the typical steps in the RCA cleaning processes.

Many modifications have been done on the RCA clean by choosing different mixture ratio and different working temperatures. Realize Inc. employed dilute SC-1 solution ($NH_4OH : H_2O_2 : H_2O = 0.05 : 1 : 5$ at 80°C) to decrease surface roughness and cost [Rea92]. Itano et al. [Ita96] proposed room temperature SC-1 cleaning to increase bath lifetimes and minimize exhaust air formation. Hashimoto Chemical Corporation proposed a whole room temperature cleaning procedure including using surfactants and megasonics [Has95a]. Ultra-dilute RCA cleans were also proposed in which a chemical ratio as low as $NH_4OH : H_2O_2 : H_2O = 1 : 5 : 1000$ was used [Tus97].

Heyns et al. [Hey93] and Meuris et al. [Meu95] realized that the particle cleaning efficiency of the RCA process was due to the oxidizing and subsequent etching of a sacrificial surface layer about 2 nm in thickness, while the surface roughening was also due to the coexistence of oxidizing and etching chemicals. Based on this argument they proposed a new wet cleaning concept, the IMEC clean, which separates the wafer oxidization and etching stage. The first step is to grow a 1.5-2 nm thick chemical oxide layer, and then the second step is to remove the chemical layer with HF-based etching agents. Contaminants are removed with the sacrificial layer.

Regardless of the versatility of the combination of procedures, HF-based etching agents are always involved in wet cleaning. During the real fabrication process, the recycled HF-based etching agents are degraded continuously because of the accumulation

of contaminants. Thus the cleaning efficiency decreases with the increase of repeated recycling. Contaminants such as particles, organic and inorganic chemicals will degrade the device yield and performance. Surface roughening also has a detrimental effect on device performance. In order to obtain a perfect wafer surface, additives have been used in hydrofluoric acid solution to minimize these problems. In Chapter 2, a review on previous work is presented.

One aspect of this study is to understand the fundamentals of silicon-contaminant interactions in hydrofluoric acid solution and the effects of additives to improve the quality of HF cleaning. In Chapter 3, the mechanism of particle deposition and the effects of surfactants are discussed. The particle deposition is caused by large van der Waals attraction of the silicon surface. The surfactant efficiency is found to correlate with the zeta-potential change quite well. In Chapter 4, the interaction between a silicon surface and a silicon nitride surface is studied in detail with the atomic force microscope. The direct force measurements revealed that the surfactants not only change the electrostatic force, but also the adhesion force. The force-distance curves can be simulated with the classic DLVO theory, except for the formation of monolayered surface film when some surfactants were used. The mechanism of copper preferential deposition onto silicon surface from DHF solution is discussed in Chapter 5. The preferential deposition is caused by defect-enhanced nucleation. A novel technique to characterize copper outplating in situ is presented in Chapter 6. The open circuit potential of a silicon electrode in HF solution is a function of surface copper contamination. The sensing mechanism is explained with mixed potential theory. Surfactants have been frequently

employed to minimize particle re-deposition in HF cleaning. However the surfactant effects on copper outplating had not been studied in detail previously. Therefore they are discussed in Chapter 7.

The other aspect of this study was purely theoretical. Since silicon surface-particle interactions are within the framework of DLVO theory, named after Derjaguin, Landau, Verwey and Overbeek, which describes surface interactions as the summation of electrostatic and van der Waals interactions and has become the classic theory in colloid and interface science, some details not accounted for so far in the theory were investigated. Chapter 8 deals with the potential distribution near a surface with the presence of highly asymmetrical electrolytes. Approximate analytical expressions are obtained for semi-infinite planar surface with better accuracy and greater simplicity than previous expressions. The accuracy of the approximation is evaluated numerically with finite element method. Chapter 9 theoretically reveals a very interesting phenomenon in the colloidal system: long-range attraction between two like-charged surfaces. This kind of attraction has been experimentally observed by other people, but DLVO theory cannot explain it. A new theory is established in Chapter 9 which includes DLVO theory as a special case. With this new theory, the puzzling long-range electrostatic attractions between like-charged surfaces are clearly understood.

Chapter 10 gives a summary to the whole study. This dissertation is ended with an appendix in which a novel method to produce a porous silicon layer is included.

CHAPTER 2
LITERATURE REVIEW

During dilute hydrofluoric acid treatment, the chemical or native oxide layers are removed from silicon wafer surfaces. However, bare silicon is susceptible to particle deposition and noble metal pitting such as copper, silver, gold and platinum. Surface roughness is also increased by hydrofluoric acid solution etching on silicon. Particle contamination, metal contamination and surface roughening would degrade device yield and performance [Tak98, Hat98, Ver92].

Particle Deposition

Mechanism

In solution, particle deposition is governed by the dispersion and electrostatic interactions between the wafer and particles [Sai89, Sai93, Ita90, Ita92, Ita93, Ita95, Ita96, Ita98, Ril93a, Ril93b, Don93]. Dispersion force is an induced dipole - induced dipole interaction in nature. For a molecular pair, the dispersion energy is inversely proportional to the sixth power of the distance between two molecules. The dispersion energy of two macroscopic bodies could be calculated by integrating all all the molecule pair interactions of the two bodies [Ham37]. The interaction energy for a sphere and a semi-infinite slab is inversely proportional to the separation distance [Isr92].

Most materials, upon coming into contact with a solution, gain surface charges by ionization of the surface, adsorption of ions onto the surface, or ionic dissolution. The charged surface influences the ion distribution in the solution, attracting opposite charges and repelling same charges. While the charges in the solution themselves are under the thermal motion, a tendency to break any ordered structure to a random one. An electric double layer structure is thus formed under the balance of electrostatic interaction between the charged surface and the ions in the solution and thermal motion of ions in the solution. When two charged surfaces in solution approach each other, the ions between them in the solution have to change their distribution accordingly. Therefore the system energy is changed. This is the electrical interaction of two charged macroscopic bodies in solution.

The total interaction of two macroscopic bodies in solution is therefore the summation of their dispersion interaction and electrical interaction. Figure 2-1 gives a schematic representation of the particle-plate interaction based on DLVO theory. It is a complex function of material characteristics, geometry, surface potential, temperature, electrolyte charges and concentrations, and separation distance. For most cases in an aqueous system the dispersion interaction is attractive, while the electrical interaction could be attractive or repulsive depending on the signs of surface charges[Der87, Ver48].

Saito et al. [Sai89, Sai93] found that the zeta-potentials of particles and wafers were responsible for particle deposition on silicon surfaces in HF solution. Itano et al. [Ita96] correlated the number of deposited particles with the zeta-potentials of silicon wafer and different particles (PSL, SiO_2, Si_3N_4). They found that the zeta potentials of

silicon are always negative in the pH range between 3 and 11, while zeta-potentials are positive for PSL, SiO_2 and Si_3N_4 particles when pH is low (<5). There were more deposited particles low pH than in high pH because of attractive electrical interaction. They also found the particle deposition increased with the increase of ionic strength in solution [Ita95], which further verified that the electrical interaction played an important role in particle deposition. They measured the pH of 0.5%HF solution to be 3.3; then they measured zeta-potentials of Si, PSL, SiO_2 and Si_3N_4 particles in pH 3.3 HCl solution. At this pH the Si particle zeta potential was -23mV, PSL particle zeta-potential 39mV, SiO_2 particle zeta-potential 7mV, and Si_3N_4 particle zeta-potential 43 mV. Therefore they attributed the susceptibility of particle deposition on silicon wafer surfaces in dilute hydrofluoric acid solution(DHF) to the attractive electrostatic interaction.

Riley et al. [Ril93a] considered the particle deposition from bulk solution onto wafer surfaces as a flux under particle concentration gradient and potential energy gradient; the latter were due to dispersion and electrostatic interactions between particles and the wafer. Calculations revealed the linear dependence of the number of deposited particles with submersion time. It was proved by experiments in many cases. The wafers they used were covered with a thin layer of oxide. Under this condition they found that the particles would not deposit on the wafers as long as the wafer and particles possessed the charges of the same sign, even when their surface potentials were as low as several millivolts.

However, not all experimental results support this mechanism. Riley et al. proposed a second mechanism [Ril93b] to explain those results which could not be

covered by their first mechanism. They noticed that in cases of inactive bulk deposition predicted by their first mechanism, deposition on hydrophilic surfaces did occur, and the deposition was not time dependent. Furthermore, this time-independent deposition was directly proportional to the bulk contamination level. Thus, they concluded that such deposition was due to the particles in remaining liquid film after wafers withdrew from the bath. They calculated the film volume, thus particle number, using the coating flow theory and found that the calculations were in accordance with experiment results.

Vos et al. [Vos98] found the pH of 0.5% HF was 1.9 and silicon particle zeta-potential at this pH was positive. Zeta-potentials of Si_3N_4 and SiO_2 were also positive. So the Si_3N_4 particles have a small tendency, if any, to deposit on both silicon and silicon oxide surfaces. However, they found Si_3N_4 particles deposited more on silicon oxide surfaces, although few particles were found on silicon surfaces. Therefore, they also reached the conclusion that the deposition was due to the thin film covered on hydrophilic surfaces when withdrawn from the bath. During DI water rinse, the surface potentials of both wafer and particles changed much quicker than the diffusion of particles into bulk solution. Thus the deposition happened.

Prevention of Particle Deposition

Since particle deposition is highly influenced by the electrostatic interaction, any method which can increase the electrostatic repulsion between the wafer and particles is expected to decrease particle deposition. Saito et al. [Sai89, Sai93] used anionic surfactants to change the wafer and particle zeta-potentials. Five different anionic surfactants were selected. They were tri-(2-hydroxy ethyl) ammonium dodecylbenzene

sulfonate, tri-(2-hydroxy ethyl) ammonium dodecyl sulfate, 2-hydroxy ethyl ammonium octyl sulfate, ammonium perfluoroalkyl sulfonate, and ammonium perfluoroalkyl carboxylate. Surfactants were active in diluted HF as well as in pure water. After surfactants were added, the zeta-potentials of both particles and wafer increased negatively, and the particle deposition decreases. They found the zeta-potential of silicon in 0.5% HF to be about zero, which was contradict to the results of Itano et al. [Ita95, Ita96, Ita98, Ohm93].

Itano et al. [Ita95, Ita98] examined nine surfactants, among which three were anionic, three nonionic, and three cationic. They found that nonionic surfactants did not decrease particle deposition. Anionic surfactants did alleviate particle deposition. For cationic surfactants, they found that if wafers were pre-treated to cover a thin layer of cationic surfactants and then contacted with particle slurry, particle deposition was decreased. However, if no such pre-treatment was used, no decrease in particle deposition was observed. They speculated that this was mainly because particle deposition happened before the sign reversal of silicon surface zeta-potential from negative to positive after cationic surfactant addition.

Hashimoto Chemical Corporation [Has95b] supplies HF with surfactant. It shows good particle control.

In order to minimize particle deposition on hydrophilic surfaces due to the thin film that is formed with the wafer after it is withdrawn from the bath, Vos et al. [Vos98] employed a dilute HCl rinse instead of a pure water rinse. By doing this the zeta-potentials of the wafer and particles remain positive, therefore; deposition during the

rinse stage would be minimized. They also showed that isopropyl alcohol(IPA) made a limited improvement on particle deposition in HF cleaning.

Metal Contamination

Kern et al. Have identified three basic mechanisms by which metals contaminate wafers: physisorption, precipitation of insoluble metal complexes, and deposition of free metal species [Ker91]. In dilute HF solution metal ions which have lower reduction potential than Si, such as Be^{2+}, Mg^{2+}, Ca^{2+}, Al^{3+}, Ti^{4+}, Cd^{2+}, Fe^{3+}, Co^{2+}, Ni^{2+}, Zn^{2+}, Sn^{2+}, Pb^{2+}, and Bi^{3+}, will not deposit on silicon surfaces, since the solution is acidic and these metal ions exist in the form of water complexed ions. But ions with higher reduction potential will be reduced by silicon and cause pitting on silicon surfaces. These ions are Cu^{2+}, Hg^{2+}, Ag^{+}, Pt^{2+}, and Au^{2+}[Chu97, Ohm93a]. From the variety of metals only a few are widely spread and form the main impurities of device production. The most frequently met metal impurities are iron, nickel and copper [Gra95]. Therefore copper is the most detrimental impurity in dilute HF cleaning.

Mechanism

Copper deposition on silicon surfaces is the result of the redox reaction between the Cu^{2+} ions and the silicon atom, in which Cu^{2+} is reduced to Cu and Si(0) is oxidized to Si(IV) in the form of complex with F^- in HF solution [Chu97].

$$2Cu^{2+} + Si + 6HF \rightarrow 2Cu + H_2SiF_6 + 4H^+ \quad (2\text{-}1)$$

Kern et al. [Ker90] considered that H^+ present in a HF solution can compete for the oxidation of Si, and that this competing reaction is a re-oxidation of the metal which is coupled with the reduction of hydrogen ions. The Nernst equation for the re-oxidation of Cu^{+2} ion is described as

$$E = E^{0}_{Cu^{2+}/Cu} - \frac{RT}{nF}\ln\left(\frac{\left[Cu^{2+}\right]}{\left[H^{+}\right]^{2}}\right) \quad (2\text{-}2)$$

where the partial pressure of H_2 is 1 atm. Thus, there is a threshold contamination level above which the potential becomes more favorable for the reduction of metallic species than the reduction of the H^+ ions. The calculation of this level for a metal ion where E = 0 is designated as the threshold level. It was calculated [Chu97] that the threshold level for Cu^{2+} in 49% HF solution was 1.6×10^{-6} ppb.

The electron transfer between silicon wafer and Cu^{+2} could also be understood by electron energy level consideration [Obe94]. The Fermi level of bare silicon is lower than redox potential of Cu^{2+}/Cu pair. Thus electrons will transfer from the silicon conduction band to the empty Cu^{2+} energy state. It also infers that n-type silicon has severer pitting by Cu^{2+} than p-type silicon since the potential difference between n-type silicon Fermi level and Cu^{2+}/Cu redox potential is greater than that of p-type. Experimental results have confirmed this statement [Cac92]. Another parameters affecting copper deposition on silicon surfaces are silicon doping level [Uem95, Tee95](Figure 2-2), illumination [Tee95, Tee96a, Tee96b, Tee96c](Figure 2-3), and anionic species [Aom93, Der93] (Figure 2-4).

Nanometer-sized metal particles on wafer surfaces were observed by Chyan et al. [Chy96a] using AFM. Bedge et al. [Bed93] reported EXAFS results showing copper crystals tens to hundreds of angstroms in size existed on silicon surfaces after copper spiking, while Hayami et al. [Hay95] observed molecule-like copper TRXRF signals.

Prevention of Copper Deposition

One method to prevent copper deposition from dilute HF solution onto silicon surfaces is by adding an oxidizing agent to prevent Cu^{2+} from being reduced by silicon. H_2O_2 was used and showed good results. Studies on HF / H_2O_2 / H_2O clean were carried out extensively [Shi91, Ohm91, Ohm93b, Obe94, Chu97]. However, the stability of H_2O_2 is a well-known problem for the stability, and the decomposition of H_2O_2 also increases the light point defects (LPDs) on silicon surface [Eva85, Wei76, Sch93, Hey93].

It was reported that adding HCl in HF solution alleviated copper deposition [Chu97]. Rotondaro et al. [Rot95] compared the effect of HCl to that of HNO_3 and found that the acids used seemed to have no difference. Figure 2-5 shows their results. They concluded that the reduction of copper deposition was related to the reduction of the pH of the solution. But Aomi et al.[Aom93] and Ohmi et al. [Ohm93a] found that when adding Cl^- or Br^- up to100ppm copper deposition increased drastically (Figure 2-6). It was believed that trace amounts of halogen ions catalyzed Cu^{2+} reduction by a halogen-bridged electron transfer pathway [Nag95], and Cl^- promoted the nucleation of copper deposition [Mor94, Der93]. Teerlinck et al. [Tee96b, Tee96c] showed that at low HCl concentration (10ppm) copper deposition increased, while at high concentration (0.5M) copper deposition decreased greatly (Figure 2-3). They explained the prevention of

copper deposition at high HCl concentration by copper chloride complex formation

$$Cu^{+} + nCl^{-} \Leftrightarrow CuCl_n^{1-n} \quad (2\text{-}3)$$

$$Cu + Cu^{2+} + 2nCl^{-} \Leftrightarrow 2CuCl_n^{1-n} \quad (2\text{-}4)$$

Another method to minimize copper deposition from HF solution onto silicon surfaces is by surfactant addition [Kaw89, Ohm93b]. Adsorbed surfactant molecules could form a passivation layer on silicon surfaces. Micelles in the solution could immobilize the metal ions [Ouy88, Blo82]. Furthermore, the micelle-metal ion complex decreases the redox potential of metal by decreasing free metal ions [Obe94].

Shimono et al. proposed to use Au-poly-Si as an adsorbent to purify HF solution during ULSI manufacturing [Shi93].

Surface Roughening

One of advantages of HF cleaning is that it provides a hydrogen passivated surface. This surface is covered by about 90% hydrogen [Yab86, Gru86, Bur88, Dum91, Zaz89, Tho89]. It has high stability against oxidation [Mor89, Gra90, Bjo95] with low density of surface states [Yab86]. However, HF clean can increase surface roughness [Bur88, Cha88, Lju93] which has great impact on the integrity of thin gate oxide as well as the channel electron mobility [Ohm91b, Ohm92, Miy92]. Figure 2-7 shows the roughness change after DHF clean [Lju93].

Mechanism

An increase in silicon surface roughness by noble metal pitting is well known. Cations such as Cu^{2+} can oxidize Si(0) to Si(IV); the latter are complexed with F^- and dissolves into solution, according to equation (2-1), and leaves pitting on the surface. On the other hand, the deposited copper enhanced silicon oxidation, thus; etching by HF was also enhanced. Microfacets of (111) like surface structures can be formed in (100) surface [Gra91]. The decomposition of H_2O_2 can also contribute to surface roughening, as described before.

Another mechanism of surface roughening is due to HF etching on silicon surfaces. Although it appears that HF solution does not etch silicon, it does to some extent. The HF etching rate on silicon is about 1000 times slower than that on silica and it can be modeled as follows [Ver93]:

$$R = 0.0119[HF] + 0.0025[H_2F_2] + 0.0356[F^-] + 0.267[HF_2^-] \quad (2\text{-}5)$$

where the unit of the etching rate is nm/min, and the unit of concentration is mole/L. In HF cleaning the roughness increase is caused by nonuniform etching off the top molecular layers of silicon surfaces after native or chemical oxide is removed. It is worth mentioning that a direct correlation between surface roughness and the amount of adsorbed C contamination was found. But the authors did not offer the explanation [Bjo95].

Prevention of Surface Roughening

Any method to decrease metal deposition will decrease roughening. Here only the methods to prevent surface roughening caused by nonuniform etching will be discussed.

Buffered HF solution (BHF, $NH_4OH + HF + H_2O$) can give atomically flat (111) silicon surfaces [Cha86, Jac91, Dum92, Bec90, Hes91, Kim91, Itay92], but it will cause roughening on (100) surface and makes thermodynamically stable (111) microfacets [Kik90, Itay95, Dur93]. Surfactants were added to improve surface flatness [Miy94]. HF/ethanol mixture was reported to give improved surface flatness [Pro88, Pro91, Gar92].

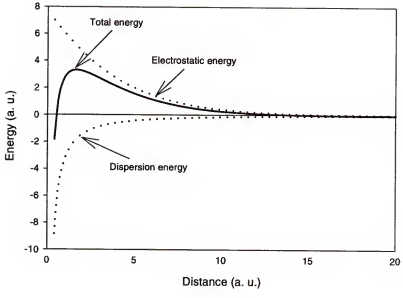

Figure 2-1. Schematic representation of particle-wafer interaction based on DLVO theory. The total interaction is the summation of electrostatic and van der Waals interactions. Enough repulsive electrostatic interaction will cause a energy barrier when two surfaces approaching.

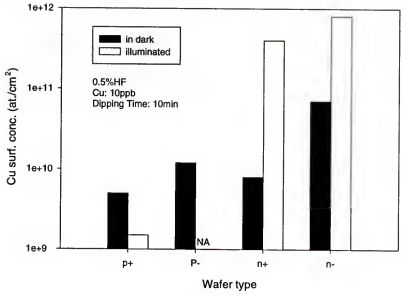

Figure 2-2. Copper deposition on different wafers [Tee95]. The amount of surface copper contamination is a function of doping type, doping level and illumination. Under illumination n-type wafers show higher contamination than p-type waters.

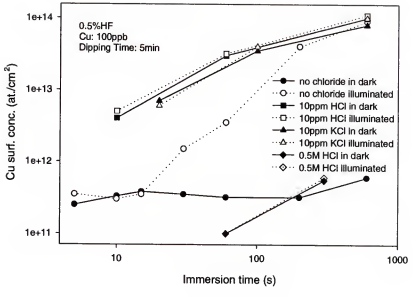

Figure 2-3. Copper deposition under different conditions [Tee96c]. Both illumination and low concentration of chloride ions will increase copper contamination. 0.5 M HCl can reduce copper contamination significantly.

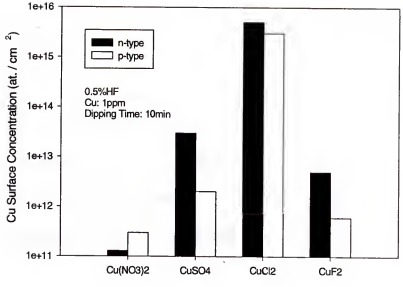

Figure 2-4. Anion effect on copper deposition [Aom93]. A little amount of chloride ions can significantly increase copper contamination on both n and p-type silicon wafers.

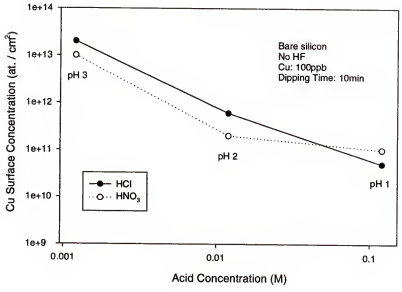

Figure 2-5. Copper deposition in different acidic solution [Rot95]. With the decrease of pH in HF bath, the amount of copper deposited on silicon surface is also decreased.

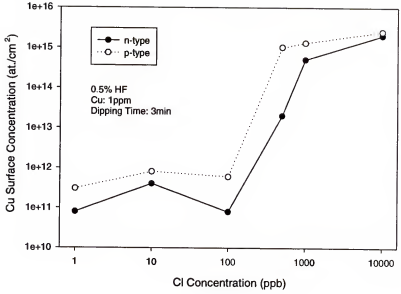

Figure 2-6. Chloride ion effect on copper deposition [Aom93]. 1-10 ppm level of chloride ions will increases copper deposition on both n and p-type silicon wafers.

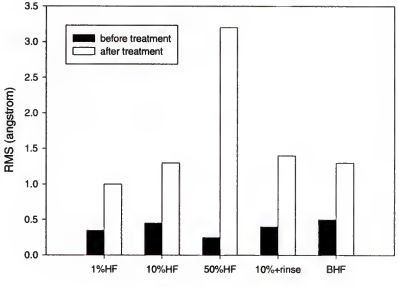

Figure 2-7. Roughness changes after HF treatment [Lju93]. The RMS roughness will increase after HF treatment, and the roughness increases with the increasing of HF concentration.

CHAPTER 3
MECHANISM AND PREVENTION OF PARTICLE DEPOSITION ONTO SILICON WAFER SURFACE FROM HF SOLUTIONS

Introduction

With the semiconductor industry moving to smaller and smaller dimensions, removing particulate contamination has become extremely critical [Hat94]. Silicon wafer ultra-cleaning is thus a vital area in semiconductor processing. The most widely used cleaning method is RCA based wet chemical clean [Ker70], which removes organic residue, particles and metal ions on wafer surfaces. A RCA-cleaned wafer has a chemical oxide layer about 1-2 nm in thickness on the surface. Dilute HF clean is employed to remove this layer and to obtain a totally hydrogen-passivated bare silicon surface, which has high stability against oxidation [Mor89, Gra90] with low density of surface states [Yab86]. However, during HF cleaning particles in the bath tend to redeposit onto bare silicon surface [Ohm93a, Ita96].

The mechanism of bare silicon wafer contamination by particles has been discussed previously [Ohm93a, Ita96, Sai93]. It was considered that the electrostatic interaction between particles and wafers played a key role in particle deposition/removal. The pH value at 0.5 wt. % HF to be 3.3 was reported and zeta-potentials at pH 3.3 adjusted with HCl were measured [Ohm93a, Ita96]. It was found that the zeta-potential of

bare silicon at pH 3.3 was negative (about –23 mV) while most particles were positively charged at this pH. Therefore, the susceptibility of a bare silicon wafer to be contaminated by particles was explained based on attractive electrical interaction between silicon wafer and particles. In more general discussions on the particle deposition Spielman et al. [Spi74] and Riley et al. [Ril93a] considered the deposition as diffusion of particles from bulk solution to surface under a potential caused by electrical double layer interaction and dispersion attraction.

The present authors calculated and measured the 0.5 wt. % HF solution pH to be about 1.9 and conducted all the zeta-potential measurements in 0.5 wt. % HF solution. It turned out that silicon was slightly positively charged in 0.5 wt. % HF solution. Particle deposition onto bare silicon was attributed to the large dispersion interaction between silicon wafer and particles. Seventeen surfactants from different types (cationic, anionic, amphoteric, and nonionic) were selected to study their effectiveness in preventing particles from depositing on silicon wafer surface in 0.5 wt. % HF cleaning. It was found that particle deposition correlated well with the product of particle and silicon zeta-potentials.

Experimental

N-type (100) silicon wafers (Silicon Quest International) were subjected to SC-1 cleaning before dipped into 0.5 wt.% HF (GB grade, Ashland Chemical Company) solutions containing 200 ppm silicon nitride particles (Alfa Aesar) with 0.3 micron mean diameter and 1 wt. % surfactant for 10 minutes. Seventeen cationic, anionic, amphoteric,

or nonionic surfactants were studied respectively. After DI water rinse the wafers were analyzed using a Jeol 6400 SEM. At least four random positions were examined on each wafer piece and 60x and 6000x magnification photos were taken at each position. The surface particles were counted statistically from the photos. Surfactant efficiency was defined as

$$Eff\,(\%) = \frac{n_0 - n_s}{n_0} \times 100 \qquad (3\text{-}1)$$

where n_0 is the surface particle density after dipping into 0.5 wt. % HF bath and n_s the surface particle density after dipping into 0.5 wt. % HF with surfactant. This Efficiency value describes how well the surfactant can prevent particle deposition, with Eff greater than zero representing decreased particle deposition and less than zero representing increased particle deposition compared with the case without surfactant added.

The zeta-potentials of the silicon nitride particles in the same solutions were measured using a Brookhaven Zeta Plus. Ten time measurements were repeated for each slurry. The silicon zeta potentials were obtained by measuring silicon powders (Atlantic Equipment Engineers) with mean diameter 5 micron dispersed in solutions at the same conditions as silicon nitride particles. The pH was measured using a HF resistant pH probe from Fisher Scientific.

Results and Discussion

The pH of 0.5 wt. % HF Aqueous Solution

The pH of 0.5 wt. % HF solution was calculated according to following equilibria [Iup82, War71]:

$$HF = H^+ + F^- \qquad K_1 = 6.85 \times 10^{-4}\ mol/l \qquad (3\text{-}2)$$

$$HF + F^- = HF_2^- \qquad K_2 = 3.963\ \ l/mol \qquad (3\text{-}3)$$

$$2HF = H_2F_2 \qquad K_3 = 2.7\ \ l/mol \qquad (3\text{-}4)$$

Figure 3-1 plots the concentration changes of different species in HF solution as a function of total HF concentration, and Figure 3-2 is the plot of pH as a function of HF concentration. It shows that HF is indeed a weak acid and when HF concentration is 0.5 wt. % (0.25M) the pH value is 1.92. The measured value was 1.86 ± 0.10. It is at odds with the previously reported value [Ohm93a, Ita96].

The Silicon and Silicon Nitride Zeta-Potentials

Figure 3-3 is the plot of silicon zeta-potential as a function of pH. The solution initially was 0.5 wt. % HF solution but the pH is adjusted with HCl or NaOH. In 0.5 wt. % HF silicon zeta-potential was measured to be 6.0 ± 2.0 mV. It is clear that in this solution bare silicon is slightly positively charged. The zeta-potential at pH 3 is about –20mV, which is in agreement with previous results [Ita96, Sai93]. After pH 3 the zeta-potentials do not change much, but when the pH is less than 2, the zeta-potential becomes positive and increases significantly with the decrease of pH. The isoelectric point of silicon therefore is about pH 2. The plot of zeta-potential change of silicon nitride as a

function of pH is plotted in Figure 3-4. The plot suggests that silicon nitride has an isoelectric point at about pH 5 and at pH 2 it is highly positively charged. It should be noted that during zeta-potential measurements no supporting electrolyte was added except 0.5% HF, in which the totally dissociated molecules are about 0.01M (pH =1.92). Adjusting pH will not change the ionic strength significantly; the change is about twofold at most.

Surfactant Efficiency

Table 3-1 lists the zeta-potentials of silicon and silicon nitride in 0.5 wt. % HF + 1 wt. % surfactant solutions as well as the efficiency of the surfactant. The correlation between zeta-potentials and the surfactant efficiency is plotted in Figure 3-5. From this figure it is known that as long as the product of silicon and silicon nitride zeta-potentials is greater than 360 mV^2, which is the value in pure 0.5 wt. % HF solution, the surfactant will decrease particle deposition.

Mechanism of Particle Deposition onto Bare Silicon Surface

The above results indicate that the susceptibility of particle deposition onto bare silicon surface cannot be attributed to attractive electrical interaction. If one compares the Hamaker constants of silicon and silicon oxide, it will be clear that silicon has more strong dispersion interaction with particles than that of silicon oxide. Some related Hamaker constants are listed in Table 3-2, where A_{11} denotes the Hamaker constant of a macroscopic matter interacting with the same kind of macroscopic matter in vacuum. Figure 3-6 plots the calculated results of dispersion energies between a 300 nm silicon nitride particle and silicon, silicon oxide and TEFLON surfaces, respectively. The

Table 3-1. Surfactant efficiency and zeta-potentials

Surfactant	**Si ζ-potential (mV)**	**Si_3N_4 ζ-potential (mV)**	**Eff(%)**
0.5 % HF	6.0 ± 2.0	58.0 ± 3.0	0
Anionic A	-22.7 ± 2.2	-51.7 ± 6.4	62.2 ± 15.9
Anionic B	-30.1 ± 2.7	-32.6 ± 2.5	30.2 ± 33.1
Anionic C	-38.7 ± 2.3	-18.5 ± 3.5	74.1 ± 18.5
Nonionic A	5.0 ± 1.5	8.2 ± 3.4	-345 ± 197
Nonionic B	9.3 ± 1.6	19.7 ± 3.0	-725 ± 310
Nonionic C	4.3 ± 1.7	20.2 ± 3.5	-493 ± 227
Nonionic D	6.8 ± 1.8	20.4 ± 4.4	-816 ± 358
Cationic A	22.7 ± 1.7	22.3 ± 3.0	59.5 ± 31.1
Cationic B	4.2 ± 1.8	21.4 ± 2.4	-729 ± 81
Cationic C	26.6 ± 3.6	25.6 ± 2.7	90.8 ± 8.1
Cationic D	38.1 ± 3.7	26.2 ± 7.7	36.8 ± 30.5
Cationic E	58.4 ± 2.8	44.2 ± 9.7	84.4 ± 12.1
Cationic F	48.2 ± 3.4	55.2 ± 7.2	74.4 ± 15.4
Cationic G	28.8 ± 2.7	20.4 ± 3.2	80.5 ± 12.5
Cationic H	31.3 ± 3.2	6.2 ± 1.5	75.8 ± 16.9
Amphoteric A	13.7 ± 2.0	26.0 ± 3.8	-150 ± 108
Amphoteric B	13.8 ± 1.2	31.9 ± 9.3	70.6 ± 17.0

Table 3-2. Hamaker constants A_{11} for some selected materials

Materials	A_{11} ($\times 10^{20}$ J)	Ref.
Water	4.35	[Bar72]
Silicon	25.5	[Bar72]
Oxides	10.6 - 15.5	[Vis72]
TEFLON	7.3*	[Hou80]

* Calculated from A_{121} with Eq. 6.

calculation is according to [Gre81]:

$$V = -\frac{A_{123}a}{6d}\left(\frac{1}{1+14d/\lambda}\right) \qquad (3\text{-}5)$$

where a is the particle diameter; d the separation distance; λ the characteristic wavelength of the interaction, often assumed to be about 100 nm and A_{123} the Hamaker constant of dispersion interaction between two macroscopic matters 1 and 3 across the media 2. A_{123} is usually approximated as [Ros88]:

$$A_{123} \approx \left(\sqrt{A_{11}} - \sqrt{A_{22}}\right)\left(\sqrt{A_{33}} - \sqrt{A_{22}}\right) \qquad (3\text{-}6)$$

Figure 3-6 shows that at any distance the London-Van de Waals interactions between bare silicon and particles are stronger than those between silicon oxide or TEFLON and particles, as long as they cannot be neglected. This attractive interaction is much stronger when particles approach silicon surface compared with the other two cases. It is the reason why in DHF cleaning particles in the cleaning bath will be easily deposited onto bare silicon surface. It is also worthwhile to mention that surface

hydrophobicity is not the cause of particle deposition in DHF cleaning step. TEFLON is hydrophobic and it is widely used as non-sticky coatings.

Mechanism of the Correlation Between Zeta-Potentials and the Surfactant Efficiency

Figure 3-5 demonstrated that the correlation between particle deposition and the product of zeta-potentials is very good. Intuitively this result is easy to understand, but not so obvious if one considers the electrical interaction energies of overlapped double layers. Equations 3-7 and 3-8 are the electrical interaction energies between a charged silicon plate and a charged spherical particle in surface potential constant and surface charge constant cases, respectively [Hog66, Der87]:

$$\Delta G_{E,cp} = \pi \varepsilon a \begin{bmatrix} \left(\Phi_{0,Si} + \Phi_{0,p}\right)^2 \ln\left(1 + \exp(-\kappa d)\right) \\ + \left(\Phi_{0,Si} - \Phi_{0,p}\right)^2 \ln\left(1 - \exp(-\kappa d)\right) \end{bmatrix} \quad (3\text{-}7)$$

$$\Delta G_{E,cc} = -\pi \varepsilon a \begin{bmatrix} \left(\Phi_{0,Si} + \Phi_{0,p}\right)^2 \ln\left(1 - \exp(-\kappa d)\right) \\ + \left(\Phi_{0,Si} - \Phi_{0,p}\right)^2 \ln\left(1 + \exp(-\kappa d)\right) \end{bmatrix} \quad (3\text{-}8)$$

where ϵ is dielectric constant of the media, a the particle diameter, Φ_0 the surface potential κ the inverse Debye length, d the separation distance, and the subscript *cp* denotes constant potential, *cc* constant charge, *Si* silicon and *p* particle. These two equations are exact only in linear region of Poisson-Boltzmann equation, i.e., surface potential less than 25 mV in room temperature. Nevertheless, they are good

approximations even when surface potentials are greater than 25 mV but less than 50 - 60 mV [Hog66]. The above equations do not indicate unequivocally the relation between the product of surface potentials and the electrical interaction energy.

The results in Figure 3 can be understood by using linear superposition approximation (LSA) when calculating the electrical interaction energy. Linear superposition approximation states that the potential distribution in overlapping double layers is just the summation of potential distributions in the two isolated double layers. It was pointed out that LSA was the leading term in an appropriate expansion for the interaction at large separation [Lev51]. The potential distribution in a planar double layer with low surface potential is

$$\Phi(x) = \Phi_0 \exp(-\kappa x) \qquad (3\text{-}9)$$

Thus the potential distribution in overlapping planar double layers, according to LSA, is

$$\Phi(x) = \Phi_{0,1} \exp(-\kappa x) + \Phi_{0,2} \exp\left(-\kappa(d-x)\right) \qquad (3\text{-}10)$$

Starting from Eq. 3-10 one can derive the expression of electrical interaction energy between a silicon plate and a spherical particle. The method can be found in detail from Ref. [Der87]. The expression is

$$\Delta G_{E,LSA} = 4\pi\varepsilon a \Phi_{0,Si} \Phi_{0,p} \exp(-\kappa d) \qquad (3\text{-}11)$$

The above equation reveals that the electrical interaction energy is proportional to the product of surface potentials.

It can be shown analytically that the LSA energy is in between of the constant surface and constant potential energies at small separations, and the three energies overlap at large separations. It is always true that

$$\Delta G_{E,cc} > \Delta G_{E,LSA} > \Delta G_{E,cp} \qquad (3\text{-}12)$$

In order to keep our discussion concise, only an example is given to illustrate Eq. 3-12. Figure 3-7 plots the calculated results of the three energies against separation distance. The calculation is done with the conditions that silicon surface potential is 20 mV, the surface potential of a silicon nitride particle is 40 mV, the electrolyte concentration is 0.01M and at room temperature. It verifies Eq. 3-12 and shows that Eq. 3-11 is a good approximation. Although zeta-potentials were different from surface potentials, it is a usual practice to use zeta-potential to do the calculations as long as the accuracy requirement is not so strict. Therefore the electrical interaction energy is determined by the product of zeta-potentials, given other parameters being the same.

Summary

The pH value in 0.5 wt. % HF is 1.9 and in this solution the bare silicon surface is slightly positively charged. Particle deposition in DHF cleaning is due to the large dispersion interaction between silicon and particles. Surfactants can be used to minimize particle deposition in DHF cleaning. The efficiency of a surfactant is correlated with its capability to increase the value of the product of silicon and particle zeta-potentials. This correlation can be understood with linear superposition approximation during the calculation of electrical interaction between silicon and particles. This work can be served as the foundation of additive selection to minimize particle deposition in general. This experiment also proves that linear superposition approximation is applicable in daily practice.

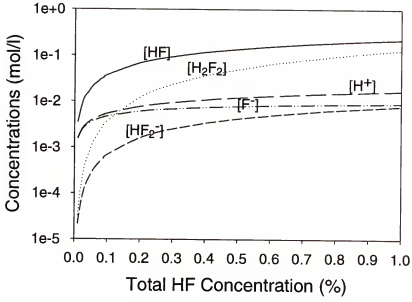

Figure 3-1. The plots of concentrations of different species in HF solution as functions of total HF concentration. The HF is a weak acid, it is only partially dissociated even in the solution with concentration as low as 0.1 wt. % total HF.

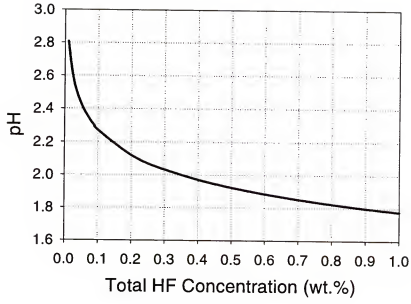

Figure 3-2. The plot of pH value as a function of total HF concentration. At 0.5% HF concentration the pH value of the solution is 1.92. The measured value is 1.86 ± 0.1.

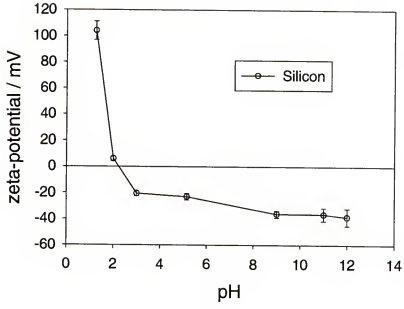

Figure 3-3. The plot of silicon zeta-potential as a function of pH. The isoelectric point is about pH 2. When pH value less than pH 2 the silicon zeta-potential changes drastically with the change of pH. After pH greater than 2 the silicon zeta-potential changes slowly with the pH.

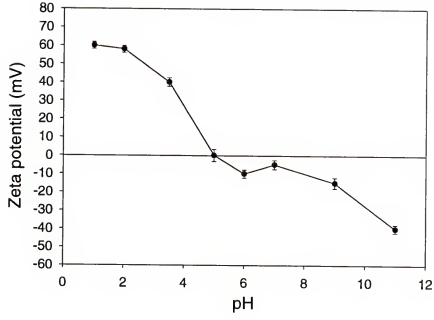

Figure 3-4. The plot of silicon nitride particle zeta-potential as a function of pH. The isoelectric point is about pH 5. At pH 2 silicon nitride is highly positively charged.

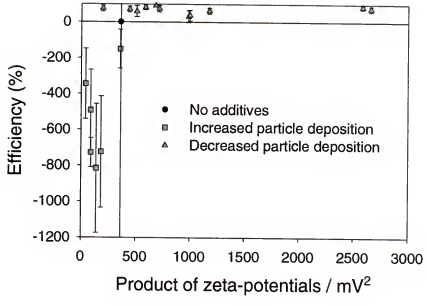

Figure 3-5. The plot of surfactant efficiency versus the product of silicon and silicon nitride particle zeta-potentials. As long as the surfactant increases the value of the product of silicon and silicon nitride zeta-potentials, it is effective in decreasing silicon nitride particle deposition on silicon wafer from HF solution.

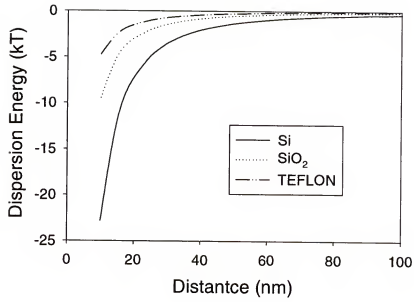

Figure 3-6. The plot of van der Waals interaction between a silicon nitride particle and different plates as functions of separation distances. Silicon surface has stronger van der Waals interaction with particles than silicon dioxide or TEFLON surfaces. ($A_{11}(SiO_2)$ = 11 E-20 J, $A_{11}(Si_3N_4)$ = 13 E-20 J, λ = 100 nm, a = 300 nm).

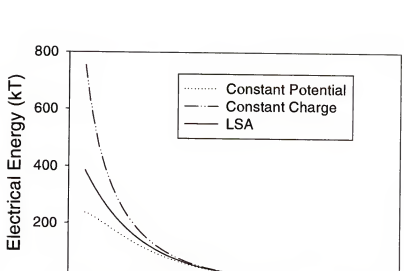

Figure 3-7. Plot of electrical interaction energies between a spherical particle and a plate as functions of normalized separation distances. The energy calculated with linear superposition approximation lies in between those calculated under constant charge and constant potential conditions. ($\Phi_{0,Si}$ =20 mV, $\Phi_{0,p}$ =40 mV, ϵ = 78 × 8.854E-12 F/m, a = 300 nm).

CHAPTER 4
SILICON-SILICON NITRIDE SURFACE INTERACTIONS

Introduction

In Chapter 3 we have demonstrated from zeta-potential and particle deposition experiments that the susceptibility of a bare silicon surface attracting particles was due to the large dispersion interactions, not electrostatic attractions, between a silicon surface and particles in a 0.5% HF solution. It has also been shown that the particle deposition can be reduced by adding certain surfactants into the dilute HF bath. The mechanism was attributed to the increased electrostatic repulsion between a silicon surface and particles. In this study, direct surface forces between a silicon surface and an AFM silicon nitride tip were measured in order to (i) confirm our previous results and (ii) to study if there was any force other than dispersion force and electrostatic force responsible for the attraction or repulsion between a silicon surface and particles.

The atomic force microscope (AFM), invented by Binnig et al.[Bin86], is a versatile tool for not only imaging but also probing nanomechanical properties and measuring surface forces. In the AFM force measurement the sample is moved up and down by applying a voltage to a piezoelectric translator to generate stable motion on sub-angstrom scale. The AFM probe, which is composed of a cantilever and a sharp tip, is fixed above the sample surface. When a sample approaches the tip, surface force makes

the cantilever deflect, and the force can be measured by recording the deflection of the cantilever accordingly. The optical level technique is used to measure the deflection of the cantilever. A laser beam from a laser diode is focused onto the end of the cantilever. The position of the reflected beam is monitored by a multiple segment photodiode known as a position sensitive detector (PSD). The backside of the cantilever is usually coated with a thin layer of gold to enhance its reflectivity. All cantilever deflections are then monitored by the PSD output. The z-position resolution is typically 0.1 Å but it is often limited by thermal vibration of the cantilever. The amplitude of thermal noise, N, can be calculated by [But95a]

$$N = \sqrt{\frac{4k_B T}{3k}} \qquad (4\text{-}1)$$

where k_B is the Boltzmann constant, T is the temperature and k is the cantilever spring constant. The force detection limit, f, can then be accessed by

$$f = \sqrt{\frac{4}{3}k_B T k} \qquad (4\text{-}2)$$

For example, the thermal noise of a cantilever deflection with a 0.12 N/m spring constant is 2 Å and the force detection limit is 25 pN.

The cantilever is usually formed by one or more beams of silicon or silicon nitride with 100 to 500 μ in length and about 0.5 to 5 μ in thickness. For the most widely used silicon nitride AFM probe, the cantilever is V-shaped to increase lateral stiffness. The tip is square pyramidal in construction but may have a rounded apex. The apex of the tip can

be approximated as a hemisphere with radius in a few tenth to hundreds of nanometers [Dru94]. Therefore, the total force of interaction can be analyzed quantitatively. The spring constant of the cantilever can be calculated theoretically [Sad93] or measured experimentally [Sen94]. An approximate spring constant can be obtained from the vendor. The term "tip" is usually interchangeable with the term "probe" in the literature, which means the combination of the cantilever and the actual sharp tip on the cantilever.

The direct output of a force measurement is a curve of PSD voltage versus sample position, as shown schematically in Figure 4-1. At large sample-tip separation the sample movement will not cause cantilever to deflect. Thus, the PSD voltage will not change with sample position. It defines a zero-force line. It is the region 1 in Figure 4-1. When sample moves close enough to the tip and the tip senses the surface force, the cantilever will deflect according to the force it senses. It is shown as the region 2 in Figure 4-1. When the tip is in contact with the sample and the sample continues to move toward the tip, then the tip deflection is the same as sample movement and the PSD voltage - sample position curve shows a straight diagonal line. It is the region 3 in Figure 4-1 and widely known as "contact region". When the sample withdraws and if there is a large adhesion force, then the free end of the tip moves with the sample until reach the position at which the spring force is large enough to pull the tip back (region 4 in Figure 4-1). This results in a sudden "jump-off" of the tip. Tip instability can also happen when a sample approaches the tip and the surface force is attractive. If the tip experiences a force gradient that equals to or exceeds its cantilever spring constant, then the tip will jump to the next location where the force gradient is less than the cantilever spring constant, or

jump onto the surface directly [Dur94]. The location where "jump-in" happens can then be calculated by using the criterion

$$\frac{dF}{dD} = k \qquad (4\text{-}3)$$

where D is the separation distance.

To obtain the force-distance curve, the PSD voltages need to be converted to the force and the sample position to the separation distance. The calibration of PSD voltage and cantilever deflection is done by the instrument vendor. Therefore, the force can be obtained by multiplying the deflection of the cantilever with its spring constant. The zero separation distance is at the location of the interception of the zero-force line and the contact region line, as shown in Figure 4-1. The other separation distances are obtained from sample position by shifting the zero-separation position and adding the deflection of the cantilever.

Surface force measurements with the AFM have gained increasing importance in the last decades. Weisenhorn et al. measured the forces between an AFM tip and a mica surface in air and in water, and found that the adhesion force was greatly reduced in water comparing to that in air [Wei89]. Mate et al. showed that by using AFM one could measure the thickness of the adsorbed molecular layers down to a thickness of 2 nm [Mat89]. Butt studied with AFM the electrostatic, van der Waals, and hydration forces in electrolyte aqueous solutions[But91]. Measuring adhesion, attraction, and repulsion between surfaces in liquids was also done by Weisenhorn et al. [Wei92]. Electrical double layer interactions of surfaces immersed in 2:1 calcium electrolyte were

investigated using both a surface force apparatus and AFM [Kek93]. Lin et al. reported local characterization of surface acid-base properties by employing AFM force measurements [Lin93]. Senden et al. also studied surface chemistry and tip-sample interactions in AFM [Sen95]. Direct visualization of CTAB hemimicelles on a graphite surface was done with the aid of AFM force measurements [Man94]. All of the above-mentioned works utilized only commercially available AFM tips to measure surface forces.

Recently there is a tendency to attach a spherical particle on the AFM tip to measure surface forces in order to provide accurately determined surface geometry and to increase surface forces. Ducker and his co-workers pioneered this technique [Duc91]. Since our previous work was dealing with silicon nitride particles and no ideal spherical silicon nitride particles were available to attach onto the AFM tip, in this study we just use commercially available silicon nitride tips to measure surface forces. Although in doing so we may sacrifice some accuracy, it has been shown that using a plain AFM tip carefully can still provide satisfactory results [Dru94]. For more detailed discussion on AFM force measurements, one should refer to the reviews by Butt et al. and Prater et al. [But95b, Pra95].

In this study, we measured surface forces between a silicon nitride tip and a bare silicon surface in air and in an aqueous solution with pH about 2. The forces with the presence of different surfactants were also studied. The surfactants we studied were a cationic surfactant, an anionic surfactant, and a nonionic surfactant. It was found that the attractive force between the silicon nitride tip and the silicon surface was much larger in

air than that in aqueous solution, that silicon-silicon nitride attraction in pH 2 aqueous solution was indeed caused by van de Waals forces, that by adding ionic surfactants the van de Waals force can be overcome and adhesion force eliminated, and that the cationic and nonionic surfactants formed layered structures on the surfaces. Mathematical simulation of the experimental results suggests that the silicon-silicon nitride intersurface forces can be described well by DLVO theory.

Experimental

The instrument was a Digital Instruments SPM nanoscope III. The liquid cell and the silicon nitride tips were all from Digital Instruments also. The 2 in. N-type Silicon (100) CZ wafers with 1 ~ 10 Ohm·cm resistivity were from Silicon Quest International. The surfactants used were a tetradecyl trimethyl ammonium bromide, CTAB, a secondary sulfonate salt, and a mixture of ethoxylated long chain alcohols, L12-8, with 8 unit ethoxylated lauryl alcohol being the main component.

Silicon pieces 1.3 × 1.3 cm^2 in size were cut from the 2 in. wafers. They were subject to an SC-1 clean to remove particulate contaminations, then rinsed with deionized water (DIW). The chemical oxide on silicon surface was removed by a 10 min 0.5 wt. % HF bath dipping. The silicon nitride tips were dipped into 0.5 wt. % HF bath for 12 hours to remove the ill-adhered gold coating then DIW rinsed before mounted on the liquid cell. The solutions were prepared with DIW and the pH's were adjusted with HCl to 1.87 ~ 1.90. The solutions also contained 0.1% HF in order to prevent oxide formation on the silicon surface. The surfactant concentrations in the solutions were 0 ppm, 10 ppm, 50

ppm, 100 ppm, 500 ppm, 1000 ppm, 5000 ppm, and 1 wt. %. The silicon sample was mounted on the sample holder right after HF dipping and DIW rinse. Then the force measurements in air were finished within 20 min and the solutions were injected into the cell. The measurements were done, starting from the low surfactant concentration. After each solution the cell was rinsed by injecting 50 ml DIW. The force was measured in different locations and at least 10 measurements were randomly recorded. It should be noted that the results presented in the following sections are typical results from repeated measurements, and if any conclusion is drawn, it is based on the statistical analysis of all the results obtained, not only those graphed in the figures.

Results and Discussion

Silicon - Silicon Nitride Surface Interactions in Air and in Water Without Surfactant

The typical curves of silicon -silicon nitride surface interaction are plotted in Figure 4-2. In the figure both the PSD voltage-sample position curve and the force-separation curve are plotted, since the former are the direct measured results but are not convenient to compare among themselves. The latter force results are more widely known but are indirectly obtained with the possibility of increasing error. The values of spring constant and effective tip radius used to transform PSD voltages to force were 0.12 nN/μ and 500 nm, respectively. The spring constant value used was given by the vendor. Although it may vary from tip to tip, it does not deviate too far from this average value due to increased accuracy of today's microfabrication technique. The effective radius was obtained by trail-and-error until all the theoretical fits are self-consistent. They will be

discussed later. More importantly, all experiments were done with the same tip. Thus the inaccuracy of these parameters will not hinder the validity of cross-comparison. Usually AFM force measurement is more accurate from the approaching direction, since the retracting direction often involves adhesion forces which always cause tip instability. Thus the approaching curve at short separation is especially presented for each solution and may reveal more detailed information.

The approaching curve in Figure 4-2 shows a long range attractive force starting at about 100 nm from the silicon surface. It clearly indicates the particle magnet nature of a bare silicon surface. This is the reason why oxide-free silicon wafer is susceptible to particulate contamination. The long range attractive force cannot be attributed to the van der Waals force only, since usually van der Waals force become essentially zero after 20 nm separation. There must be some other force that plays a predominant role in the apparent attractive force. One possibility is that the force is an electrostatic force. If the silicon surface and the silicon nitride surface are oppositely charged, the electrostatic interaction between them is attractive. Furthermore, since the surrounding medium is air, the electrostatic force will not be effectively screened so that the interaction range becomes quite long in comparison to the case of an electrolyte solution. There is a phenomenon closely analogous to this scenario: when CTAB powders are put into a TEFLON beaker, some of them just jump onto the side wall of the beaker. In this case the electrostatic attraction is so strong that it can pick up powders from centimeters away. Therefore, we postulate that the long range attractive force between a silicon surface and a silicon nitride surface in air is due to electrostatic interaction.

The retracting curve in the same figure shows a very large adhesion force. Similar results were also observed by other people [Mar87, Wei89]. The large adhesion force in air was attributed to capillary force. Water molecules condense on almost any surface in room temperature to form a very thin water layer. When the tip touches the sample surface, the water layers between the two surface forms a neck with negative curvature. Thus, the capillary force is in the direction to keep the two surfaces to be close. If the two surfaces are immersed into water, then the capillary force should vanish and the adhesion force be greatly reduced. This is shown by the retracting line in DIW (Figure 4-3), in which the normalized adhesion force is reduced significantly. This is also one reason why wet cleaning dominates over dry cleaning in semiconductor processing.

The approaching curve in Figure 4-3 shows a repulsive force at long separation between silicon and silicon nitride surfaces. At short separation the force becomes attractive and the tip suddenly jumps onto the silicon surface. This can be understood by combining van der Waals force and the electrostatic force. From the Figures 3-3 and 3-4 in Chapter 3, the zeta-potential of silicon at pH 6 is about -30 mV, and the zeta-potential of silicon nitride is about -10 mV. In DIW the pH value is about 6 because of the dissolution of carbon dioxide from surrounding environment. Therefore, the electrostatic interaction between a silicon surface and a silicon nitride surface is repulsive at long separation. At short separation, the van de Waals interaction becomes dominant so that the total interaction force is attractive. It should be noted that the zeta-potential values from Figure 3-3 and Figure 3-4 may not be equal to those in DIW because the ionic strength is different in the two cases. However, we would expect more negative values in

DIW as the screening effect would be less. At short separation the attractive van der Waals is predominant so that the total force becomes attractive and causes a maximum force barrier at the turning point.

The silicon-silicon nitride surface interaction changes significantly when pH decreases to 2, which is the isoelectric point of silicon. At this pH the measured silicon zeta-potential is 6 mV and silicon nitride zeta-potential is 60 mV. No repulsive force was observed on the approaching line of Figure 4-4. This is because the electrostatic force is so small that in all of the interaction range the van der Waals force predominates. The retracting line also shows an adhesion force. Statistical analysis suggests that the adhesion force in pH 2 solution is greater than in DIW. However, the reason is not known. As it has been pointed out, the pH value of 0.5 wt. % HF solution is about 2. Thus, the results shown in Figure 4-4 reveal one of the drawbacks of dilute HF cleaning. In this solution the silicon surface attracts particles easily. Once a particle is on the silicon surface, it cannot be removed easily because there is an adhesion force to overcome. The process of particle attachment-detachment on a silicon surface is not reversible. That is why the control of particle redeposition onto silicon wafer surface is one of the critical issues during dilute HF cleaning.

Silicon-Silicon Nitride Surface Interactions in Water with Surfactant

After surfactants were added to the solution, the interactions between silicon and silicon nitride surfaces were changed significantly. The effect of cationic surfactant CTAB with pH fixed about 2 is shown from Figure 4- 5 to Figure 4-11. It can be seen from the figures that with the increasing of CTAB concentration every approaching curve

shows a "jump-in" near the surface after a force barrier. When CTAB concentration is less than 500 ppm, the force is attractive until the tip touches the surface. From the 500 ppm CTAB concentration, the force after "jump-in" is repulsive all the way to the surface. The "jump-in" seems to result from the breaking of a surface film structure. A similar observation was also shown in the work of Manne et al. [Man94] but was not discussed. The jump-in distances in our study were slightly vary from 2 to 3 nm.

The retracting curves show an adhesion force for CTAB concentration less than 500 ppm, and the retracting curves overlap with approaching lines when CTAB concentration is equal to or greater than 500 ppm. They suggest that at low concentration (less than 500 ppm) CTAB cannot prevent a particle from depositing because there is barely any force barrier. More importantly, if a particle is attached on the surface, it requires a quite large force to detach it due to the large adhesion force. The attachment - detachment is not a reversible process; as long as a particle overcomes the barrier by thermal motion it will stick to the surface and will be difficult to remove. In other words, attachment of a particle is easier than detachment. At high concentrations (starting from 500 ppm) CTAB can effectively prevent particle deposition, since there is no attractive force and adhesion force. Particle deposition tests presented in Chapter 3 showed that 1 wt. % CTAB had about 90 % silicon nitride particle removal efficiency.

The adhesion force is difficult to analyze quantitatively. First of all, the contact area cannot be easily defined, as revealed by Hertz model[Her81], DMT model [Der75], and JKR model [Joh71] for instances. The contact area is highly dependent on the surface forces as well as the applied force. If the forces are not clearly known, the contact area

cannot be predicted. Furthermore, all the models are dealing with viscoelastic deformation during contact. If plastic deformation occurs, then these models are not applicable. Secondly, the interfacial energies are not generally available. Even if the contact area is known, it still requires the knowledge of interfacial energy to evaluate adhesion. The interfacial energy itself between a solid and a liquid or gas is a challenging task to evaluate. In fact, people measure interfacial energy by measuring adhesion force. Thirdly, surface roughness will influence adhesion force greatly. It is reported that even small surface asperities can significantly reduce adhesion [Tab77]. Finally the tip may move on the surface during retraction, causing ill-defined geometry and contact area. These are the reasons that the adhesion force in AFM force measurements the adhesion force generally gives a large deviation, and only the trends of the adhesion can be discussed.

The normalized adhesion force between silicon and silicon nitride as a function of CTAB concentration is plotted in Figure 4-12. It shows that the adhesion force is reduced significantly. Before CTAB is added, the measured adhesion force is 3.72 ± 1.44 nN/μ. After adding CTAB the adhesion force becomes about 0.7 nN/μ, and it does not change much at low CTAB concentrations (up to 100 ppm). The adhesion force suddenly drops to zero when CTAB concentration changes from 100 ppm to 500 ppm and remain zero after 500 ppm concentration. Note that the critical micelle concentration (CMC) of this CTAB is about 1210 ppm at room temperature [Muk71].

The curves of silicon-silicon nitride interaction with the presence of different amounts of anionic surfactant at pH about 2 are shown from Figure 4-13 to Figure 4-19.

In 10 ppm surfactant concentration solution the interaction is attractive. The attraction starts at about 10 nm separation from the surface, as shown on approaching curve in Figure 4-13(C), which is very similar to the case in pH 1.88 solution without surfactant (Figure 4-4(C)). However, the adhesion force suggested by the retracting curve (Figure 4-13(A and B)) is much greater than that in pH 1.88 solution without surfactant. It suggests that the adsorbed anionic surfactant molecules at low concentration level can increase silicon nitride-like particle contamination of silicon wafers.

After the anionic concentration increases above 10 ppm, the approaching and retracting lines overlap, suggesting a reversible process. In all of the interaction range the force is repulsive, and the adhesion force is not observed. It indicates that this surfactant is very effective in preventing a silicon nitride-like particle from depositing on a silicon wafer surface. Even if a particle of this kind is attached on the silicon wafer surface, it is easy to remove, as there is no adhesion force between silicon and silicon nitride surface with the presence of no less than 50 ppm of this anionic surfactant. The results of particle deposition tests in Chapter 3 showed that this surfactant is effective in preventing silicon nitride particle deposition at 1 wt. % concentration. Both the particle deposition test results and AFM force measurement results agree with each other quite well. It is interesting to note that in this surfactant solution, the surface film structure is not observed. The normalized adhesion force change as a function of the anionic surfactant concentration is plotted in Figure 4-20. It clearly shows that the adhesion decreases suddenly to zero when concentration increases from 10 ppm to 50 ppm. The CMC of this surfactant is 350 ppm.

The effect of the nonionic surfactant L12-8 on silicon - silicon nitride interaction as a function of concentration is shown in the series of figures from Figure 4-21 to Figure 4-27. When the concentration is not more than 50 ppm, the attracting lines in Figure 4-21 and Figure 4-22 show that the interaction is always attractive, which is similar to the cases in 1.88 pH solution (Figure 4-4(C)) and 10 ppm anionic surfactant solution (Figure 4-13(C)). After the concentration exceeds 50 ppm a secondary force barrier is clearly observed at about 4.5 nm separation as a jump-in of the tip. The attractive force is no longer observed as long as the force barrier appears. The adhesion force is always shown in the concentration range from 10 ppm to 1%. Therefore, this surfactant is not effective in preventing silicon nitride-like particles from depositing on silicon wafer surface. As long as a particle overcome the force barrier, it will stick to the surface because of the existence of an adhesion force, and not be easily removed. This result is in accordance with the particle deposition results presented in Chapter 3.

The adhesion force, however, shows significant change with the change in the nonionic surfactant concentration. The plot of normalized adhesion force versus surfactant concentration is shown in Figure 4-28. The surfactant is actually a mixture of surfactants where the mean component is 8 unit ethoxylated lauryl alcohol (C12E8). The CMC of C12E8 is about 37 ppm. When the surfactant concentration is in the range of 10 to 50 ppm, the adhesion force is very large, about 17 nN/μ, and does not change with concentration. When the surfactant concentration is in the range of 50 to 500 ppm, the adhesion force decreases to about 1 nN/μ. When the concentration is greater than 500 ppm, the adhesion force does not change with concentration, remaining at about 1 nN/μ.

Now we can discuss a general behavior of adhesion force based on all the experiments presented above. As long as there is a repulsive force, or an increased repulsive force on the approaching curve, then the adhesion force on the retracting curve will be reduced. For example, let us look the DIW (Figure 4-3) and pH 1.88 solution (Figure 4-4) cases. In DIW the approaching curve shows some repulsion while in the pH 1.88 solution the whole interaction is attractive. As a consequence, the adhesion in pH 1.88 solution is greater than that in DIW. Another example is associated with the cationic surfactant. Below 500 ppm surfactant concentration there is an attractive force on the approaching curve and above this concentration the approaching curve shows no attractive force. The adhesion force also disappears above this concentration. A third example is related to the anionic surfactant, at which only 10 ppm shows an adhesion force. Only at this concentration is the attractive force shown on the approaching curve. A last example can be found in the nonionic surfactant solution. The adhesion force is greatly reduced when the attractive force on the approaching curve vanishes. Therefore, we can conclude that the presence of a repulsive force will decrease adhesion.

Formation and Properties of Surfactant Film on Surfaces

The film-like structures near the surface in the cationic solution and nonionic solution are of particular importance. They may relate to the properties of the self-assembling surfactant layers on the surface. Before we discuss the formation of surface films, we will discuss the adsorption of the surfactants on the silicon and silicon nitride surfaces. The zeta-potential results presented in Chapter 3 can serve this purpose. Table 4-1 lists the zeta-potentials of interest. The silicon nitride zeta-potential in pH 1.92

solution is about 60 mV and in 1 wt. % CTAB pH 1.88 solution is about 44 mV, thus the cationic surfactant does adsorb on a silicon nitride surface appreciably in an aqueous solution with pH about 2. The silicon zeta-potential in this solution increases from 6 mV to 58 mV after adding 1 wt. % CTAB, indicating that CTAB is adsorbed on the silicon surface also. However, the nonionic surfactant L12-8 changes the zeta-potential of silicon nitride but dose not change the zeta-potential of silicon. Thus, it is clear that L12-8 adsorbs on silicon nitride surface, but whether it is adsorbed on silicon surface from zeta-potential data is not certain. As for the anionic surfactant, it is adsorbed on both surfaces, since the zeta-potentials of both surfaces are changed after adding 1 wt. % surfactant.

Table 4-1. Zeta-potentials of silicon and silicon nitride surface in different solutions.

Solution	Silicon	Silicon nitride
DIW	-30 mV	-10 mV
pH 1.90 solution	6 ± 2 mV	60 ± 3 mV
1 wt. % CTAB pH 1.90 solution	58 ± 3 mV	44 ± 10 mV
1 wt. % anionic surfactant pH 1.90 solution	39 ± 2 mV	18 ± 3 mV
1 wt. % L12-8 pH 1.90 solution	7 ± 2 mV	20 ± 4 mV

A typical approaching curve at short distances in CTAB solution is shown in Figure 4-29. The repulsive force before the jump-in decays exponentially, suggesting the electrostatic nature of this force. The three parameter regression, $y = y_0 + a*\exp(b*x)$,

gives a satisfactory fit with $r^2 = 0.94$. The jump-in happens at about 2.5 nm separation. This observation can be understood by considering a film structure present between the silicon and silicon nitride surfaces. It has certain rigidity; before the true surfaces touch one another, the film acts as an integral part of the true solid surface and the electrostatic repulsion was observed. When the tip comes closer and touches the CTAB film, it breaks causing a sudden jump-in of the tip. The tip continuously approaches the silicon surface and senses a hydration-type repulsive force until it eventually touches the solid surface and Born repulsion takes place.

The film thickness is defined by the jump-in distance and the breaking force is given by the difference between the force at jump-in and the minimum force, as shown in Figure 4-29. The film thickness does not change with the CTAB concentration (Figure 4-30). We can access the stretched length of a CTAB molecule based on bond lengths and the angles between atoms. A typical sp^3 C-C bond is 1.54 nm and C-N bond is 1.47 nm, and the ideal angle between two sp^3 C-C bonds is 108.5° [Crc97]. Therefore the CTAB molecule stretched length is about 1.9 nm. The average film thickness is about 2.2 nm, close to the length of a stretched molecule. Thus the film can be regarded as a monolayer of CTAB on silicon-silicon nitride interface. Note that the CMC of the CTAB is about 1210 ppm. This indicates that the surface layer forms very easily; it begins to appear far below the concentration at which micelles form in the bulk solution. In fact the CTAB concentration is two orders of magnitude lower than the critical micelle concentration.. The film density increases slightly with the increase of CTAB bulk concentration, as suggested by the plot of the normalized breaking force of the film as a function of bulk

concentration (Figure 4-31), which shows that the required breaking force increases slightly as the bulk concentration increases.

The approaching curve at short separation distances in nonionic surfactant, L12-8, is graphed in Figure 4-32, which shows an elastic deformation of the film structure starting from 6 nm separation and structure breakdown at about 3 nm separation, at which the tip jumps directly onto the silicon surface. The regression analysis in the elastic deformation region gives a straight line with $r^2 = 0.95$. The breaking force is given by the difference between the force at jump-in and the minimum force, and the film thickness by the separation at which the force is half of the breaking force, as shown in Figure 4-32. The film thickness-L12-8 concentration plot is given in Figure 4-33, on which there is a sudden change between 50 and 100 ppm concentrations. Before 50 ppm no film structure is observed, and after 100 ppm the film is formed with relatively same thickness. For comparison, the 37 ppm vertical line is included in the graph, which is the CMC of C12E8. Therefore, we can roughly state that the film structure forms with the formation of bulk micelles. The adhesion force between silicon and silicon nitride surfaces is also plotted in the figure. It is interesting to notice that the adhesion force is inversely correlated with the surface film formation. Unfortunately, the reason for this correlation is not yet known. The average film thickness is about 5 nm and the stretched C12E8 molecule length is calculated to be 4.5 nm. Thus the film may also be a monolayer. We have already discussed that L12-8 does not change the zeta-potential of a silicon surface. Therefore, the monolayer is probably on the silicon nitride surface. The breaking force-concentration curve in Figure 4-34 shows that once the film is formed the required

breaking force of the film does not change with the change of L12-8 bulk concentration, indicating the film density dose not change.

It should also be pointed out that the breaking force for the nonionic film is significantly greater than that for the cationic film. This suggests that the attractive interactions among the nonionic surfactant molecules are greater than those among the cationic surfactant molecules. This can be understood by considering a possible repulsive electrostatic interaction among the heads of the cationic surfactant molecules. Although the CTAB molecules are not totally dissociated (the value of ~ 20% dissociation was reported for hexadecyltrimethlyammonium bromide [Pas88], the positively charged film must have electrostatic repulsive force in the film itself.

There is no surface film structure observed in the anionic surfactant solution, probably because that the anionic surfactant is a secondary sulfonate. This means the hydrophilic head is not on the end of the hydrophobic chain and standing side-by-side of the chain is precluded.

Simulations of Silicon-Silicon Nitride Interactions

The AFM force measurement data can be analyzed quantitatively under the guide of DLVO theory [Der87, Ver48], which states that the total surface force is the sum of van der Waals force and the electrostatic force. Generally speaking, DLVO theory is in accordance quantitatively with the force - distance relation at large separation measured with the AFM. However, DLVO theory is based on the continuum assumption, so it is no suprise to see the theory fails at the separation of several molecule diameters. Steric forces are some of the most common forces not included by DLVO theory. The steric

forces are due to the adsorbed molecules on the surface. Before two surfaces touch each other the adsorbed molecules are already in close contact. So a repulsive force is shown. The sensing of film structures discussed above is a good example for steric forces.

Near the hydrophilic surfaces there are always hydration layers. When such two surfaces come close, the water of hydration will be excluded from the surfaces, causing repulsive forces. They are known as hydration forces [Isr92]. When the two approaching surfaces are hydrophobic an attractive force other than van der Waals force may be observed. The origin of this attractive force is not well understood, but it is postulated to be related to the hydrogen-bond structure change near the surface [Isr92]. Oscillatory force with approximately the periodicity of the solvent molecule was also observed [Osh92]. Such force is referred to structural force. The above-mentioned non-DLVO forces are still not clearly known. Therefore, we only simulate the DLVO forces in this study.

We need to know surface potentials, Hamaker constants, cantilever spring constant and effective radius of the tip to simulate the experimental data. The values of surface potentials are not available so we will use zeta-potential to approximate surface potential. The surface potential is the potential located at the surface and the zeta-potential is the potential located at the hydrodynamic slip plane. It is usually believed to be at about 0.5 nm from the surface, just outside the first adsorbed hydrated-ions layer. The potential profile between the surface and the slip plane is treated as a linear decay, while beyond the slip plane it is exponential decay, as modeled by Gouy-Chapman diffuse layer model [Gou10, Cha13]. If no specifically adsorbed ions are present, the

difference between surface potential and zeta-potential is not much. However, if specifically adsorbed ions are present, the difference can be great; even resulting in charge reversal. The closely adsorbed layer acts as an integral part of the surface when the separation is not too small. Therefore, using zeta-potential to replace surface potential is not only appropriate but necessary.

One good example in showing the use of zeta-potentials is the silicon-silicon nitride interaction in pH 2 aqueous solution. The zeta-potential of silicon is about zero. There are no specifically adsorbed ions in the solution. Thus, it is appropriate to treat the surface potential to be about zero too. The electrostatic interaction is negligible, resulting in attractive interaction. This is the reason why the silicon wafer attracts particles so easily in 0.5% HF solution. When anionic surfactant is added into the pH 2 solution, the surfactant molecules are adsorbed onto both surfaces, and the sign of the zeta-potentials is reversed. In this case the zeta-potential differs greatly from surface potential. However, when considering electrostatic interaction, the zeta-potentials should be used because the adsorbed layers are integral parts of the surfaces. Thus, we observed repulsive interaction and the particle deposition test showed decreased particle deposition. Here the use of zeta-potential is necessary. Although the adsorbed molecules may alter the dissociation of Si-OH or Si-NH groups on the surface, which is the cause of surface charge and surface potential, the dissociation of these groups themselves cannot result in reversed surface potential since the pH is kept constant.

The cantilever spring constant is taken as 0.12 nN/μ, the value provided by the vendor, without further calibration. The remaining parameters are Hamaker constants and

effective tip radius. First we conduct a simulation on the data obtained in pH 2 aqueous solution, since the Hamaker constant for silicon -silicon nitride interaction in water medium has been calculated based on optical data to be ~ 6.8E-20 J [Hou80, Sen95]. Following the satisfactory fitting of the data the effective tip radius is then obtained. Then we simulate other experimental data for which the Hamaker constant may not be known. All simulations are considered satisfactory when self-consist results are obtained.

Following Derjaguin et al. we use the electrostatic force formula derived from linearized Poisson - Boltzmann equation and Derjaguin approximation. The electrostatic interaction free energy at constant charge condition between a spherical particle with radius R and a plate, $\Delta G_{S\text{-}P}^{cc}$ is [Der87]

$$\Delta G_{S-P}^{cc} = \varepsilon \pi R \left\{ \begin{array}{l} 2\Phi_{10}\Phi_{20} \ln\left[\coth\left(\frac{1}{2}\kappa D\right)\right] \\ -\left(\Phi_{10}^2 + \Phi_{20}^2\right)\ln\left[1-\exp(-2\kappa D)\right] \end{array} \right\} \qquad (4\text{-}4)$$

where Φ_{10} and Φ_{20} are surface potentials of spheres 1 and 2, respectively, at infinite separation, ϵ is the permittivity of the medium, D is the separation distance and

$$\kappa = \sqrt{\frac{2z^2q^2n_0}{\varepsilon kT}} \qquad (4\text{-}5)$$

Z is the valence of the z-z symmetrical electrolyte, q the unit charge, n_0 the bulk concentration of the electrolyte, k the Boltzmann constant, and T the absolute temperature. The electrostatic interaction free energy at constant potential condition between a spherical particle with radius R and a plate, $\Delta G_{S\text{-}P}^{cp}$ is [Der87]

$$\Delta G_{S-P}^{cp} = \varepsilon\pi R \begin{Bmatrix} 2\Phi_{10}\Phi_{20}\ln\left[\coth\left(\frac{1}{2}\kappa D\right)\right] \\ +\left(\Phi_{10}^2+\Phi_{20}^2\right)\ln\left[1-\exp(-2\kappa D)\right] \end{Bmatrix} \qquad (4\text{-}6)$$

There is also an expression of interaction energy related to the assumption that the interacting potential is the linear summation of two isolated potentials. It is known as Linear Superposition Assumption (LSA) and is valid for large separation distances.

$$\Delta G_{S-P}^{LSA} = 4\pi\varepsilon R\Phi_{10}\Phi_{20}\exp(-\kappa D) \qquad (4\text{-}7)$$

For a detailed derivation of Eq.4-7, one should refer to Chapter 3 or reference [Der87].

From the expression of interaction energies, we can derive the interaction force yielding

$$F = -\frac{d\Delta G}{dD} \qquad (4\text{-}8)$$

Therefore, the forces under different conditions are

$$F_{S-P}^{cc} = \frac{\varepsilon\kappa\pi R}{\sinh(\kappa D)}\left[2\Phi_{10}\Phi_{20}+\left(\Phi_{10}^2+\Phi_{20}^2\right)\exp(-\kappa D)\right] \qquad (4\text{-}9)$$

for constant charge condition, and

$$F_{S-P}^{cp} = \frac{\varepsilon\kappa\pi R}{\sinh(\kappa D)}\left[2\Phi_{10}\Phi_{20}-\left(\Phi_{10}^2+\Phi_{20}^2\right)\exp(-\kappa D)\right] \qquad (4\text{-}10)$$

for constant potential condition, and

$$F_{S-P}^{LSA} = 4\varepsilon\kappa\pi R\Phi_{10}\Phi_{20}\exp(-\kappa D) \qquad (4\text{-}11)$$

for LSA assumption. Consequently, the force gradients are

$$\frac{dF_{S-P}^{cc}}{dD} = -\frac{\varepsilon\kappa^2\pi R}{\sinh(\kappa D)}\left[2\Phi_{10}\Phi_{20}\coth(\kappa D)+\left(\Phi_{10}^2+\Phi_{20}^2\right)\operatorname{csc}h(\kappa D)\right] \qquad (4\text{-}12)$$

$$\frac{dF_{S-P}^{cp}}{dD} = -\frac{\varepsilon\kappa^2\pi R}{\sinh(\kappa D)}\left[2\Phi_{10}\Phi_{20}\coth(\kappa D) - \left(\Phi_{10}^2 + \Phi_{20}^2\right)\operatorname{csch}(\kappa D)\right] \quad (4\text{-}13)$$

$$\frac{dF_{S-P}^{LSA}}{dD} = -4\varepsilon\kappa^2\pi R\Phi_{10}\Phi_{20}\exp(-\kappa D) \quad (4\text{-}14)$$

for constant charge, constant potential and LSA, respectively.

The non-retarded van der Waals interaction energy, W, between a sphere with radius R and a plate is given by Hamaker [Ham37]:

$$W = -\frac{AR}{6D} \quad (4\text{-}15)$$

for D << R, where A is the Hamaker constant. Strictly speaking, for macroscopic bodies immersed in water the retardation effect should be considered. The retardation effect is caused by the finite transport velocity of an electromagnetic field. The time required for the electromagnetic from one matter can be comparable with the period of the dipole fluctuation itself. Therefore, when a modulated electromagnetic field comes back to the matter from the other matter, the field then encounters a different polarization state, causing reduced attraction [Isr92].

The expressions of retarded van der Waals interactions are not available for all geometries. The difficulty arises from that the convenient expression of retarded interaction between molecules over the entire range of separation distances is not available. Nevertheless, empirical expressions for retarded van der Waals interactions involving plates and/or spheres were reported [Gre81]. For sphere-plate interaction the expression is

$$W_{S-P} = -\frac{AR}{6D}\left(\frac{1}{1+14\frac{D}{\lambda}}\right) \qquad (3\text{-}16)$$

where λ is the characteristic wavelength of the interaction, often assumed to be about 100 nm. It comes from the electromagnetic field propagation distance during one rotation of a Bohr electron. In this study, the separation distances in consideration are mostly not more than 10 nm. It turned out that the difference between the expressions (4-15) and (4-16) are comparable with the experimental noise. Therefore we will neglect the retardation effect during our simulations. The van der Waals force between a sphere and a plate is then

$$F_{S-P}^{vdw} = -\frac{AR}{6D^2} \qquad (4\text{-}17)$$

the force gradient is

$$\frac{dF_{S-P}^{vdw}}{dD} = \frac{AR}{3D^3} \qquad (4\text{-}18)$$

Therefore, the experimental data can be simulated by combining the electrostatic force (Eqs.(4-9), (3-10), or (4-11)) and the van der Waals force (Eq.(4-17)), and the theoretical jump-in distance can be obtained from Eqs.(4-3), (4-12), (4-13), (4-14), and (4-18).

The force-separation distance curve in approaching direction in pH 2 solution is graphed in Figure 4-35 along with the simulated curves. The surface potentials are 6 mV for silicon and 60 mV for silicon nitride (Table 4-1). The Hamaker constant is 6.8E-20 J. The background electrolyte is 1-1 type and the concentration is 1E-2 M since it is pH 2 solution. The tip effective radius is 500 nm. It shows that the constant potential

simulation fits the experimental quite well. The calculated jump-in distance based on constant potential condition is 5.0 nm, also in agreement with the experimental results. Constant potential condition states that during interaction the surface potentials remain the same. It usually applies to the surfaces on which the ion exchange equilibrium is very fast. In pH 2 solution the ions responsible for charging the silicon and silicon nitride surfaces are protons, and the dissociation/ association of SiO-H or SiN-H groups are fast reactions. Therefore, the surface potentials keep constant during interaction.

The plot of force versus separation distance in approaching direction in DIW is shown in Figure 4-36. In this case, constant charge fitting gives the best results. This could be due to very low proton concentration in DIW. The background electrolyte is not 1E-7 M but 1E-5 M due to possible contamination by dissolved carbon dioxide and by the ion leaching from container walls. The electrolyte concentration value we used here is comparable with that reported by Larsen et al. [Lar97]. The Hamaker constant is still 6.8E-20 J. The surface potentials are -15 mV and -35 mV for silicon and silicon nitride, respectively. The surface potentials used were slightly larger than the measured zeta-potential. This could be due to the screening effect of electrolytes, since the zeta-potentials were all measured in 1E-2 M electrolyte solutions. The effective tip radius remains 500 nm. The calculated jump-in distance is 3.0 nm and agrees well with the experimental data.

The force-separation distance data in air can also be simulated, too. The Hamaker constant was reported as 16.84E-20 J [Sen95] for silicon - silicon nitride interaction in air. Figure 4-37 shows that the van der Waals force calculated from Eqs.4-8 and 4-16 are

too small compared with the experimental data, suggesting that the large attractive force cannot be attributed to van der Waals interaction. Therefore, there must be an attractive electrostatic interaction. The electrostatic interaction in air can be simulated as follows. The saturated water pressure in air at 20°C is 2.3388 KPa [Crc97], which is 1E-3 M. From the water dissociation constant, the ration of dissociation is calculated to be 2E-9. Thus, the concentration of totally dissociated water is 2E-12M in saturated air. Assuming the humidity is 50%, then the dissociated water is 1E-12M. Considering water as the only electrolyte, the electrolyte concentration is 1E-12M, corresponding to a Debye length of 34.34μ. The surface potentials were determined when they gave close fit with the experimental data. By this way the value of -1 V and 1 V were chosen. The fitting is according to constant potential formulation. This simulation shows that the large attractive force between silicon and silicon nitride surfaces in air is not due to van der Waals interaction, but electrostatic interaction, although the selections of surface potentials are quite arbitrary and the values we used were not necessarily the correct values.

The simulation of force-separation distance relation in 1 % cationic surfactant pH 1.90 solution is plotted in Figure 4-38. In this solution the electrolyte concentration is about 3E-2 M. The zeta-potentials are listed in Table 3-1. It was found that no simulation was satisfactory if the zero separation did not shift. Therefore a shift of 2.2 nm was adopted which is the average thickness of the cationic surface film. It means that at large separation the adsorbed surface film acts as an integral part of the surface. The fitting requires a Hamaker constant lower than 6.8E-20 J. It is reasonable since the adsorbed

surfactant molecules decrease van der Waals interaction between the two surfaces. Similar observation has been reported recently [Duc97]. Here the value of 5E-20 J of the Hamaker constant gives fairly good agreement between the fitting curve and the experimental data. The fitting curve in Figure 4-38 also suggests that during the interaction neither the surface potential nor the surface charge keeps constant, showing an intermediate mechanism. This means that when two surfaces approach, the surface film begins to dismantle because a certain amount of surface discharging occurs in this process and the film is in the location of positive charges. Therefore, the surface film structure is not seen in this solution. In this case the better fitting is given by the LSA curve. This also verifies that the application of LSA in Chapter 3 is appropriate.

However, the surface charges remain constant when the two surfaces approach each other in 1 % anionic surfactant pH 1.88 solution, as shown in Figure 4-39. The electrolyte concentration is about 4E-2 M and the Hamaker constant is 2E-20 J. The zeta-potentials in Table 4-1 were used to simulate the results. Compared with the cationic surfactant solution case, the constant surface charge boundary condition in anionic surfactant solution is very reasonable. The original zeta-potentials of the two surfaces are positive in pH 1.88 solution. After the anionic surfactant is added, the zeta-potentials are reversed. This is because anionic surfactant molecules adsorbed onto the surfaces. More importantly, the interactions between the anionic surfactant molecules and the positively charged surfaces are naturally stronger than those between the cationic surfactant molecules and the positively charged surfaces. If the adsorption of anionic molecules is strong enough, these molecules will not dissociate from the surfaces when the two

surfaces approaches. Therefore a constant charge condition is reached. Since the adsorbed molecules attach to the surface more strongly than cationic surfactant molecules, then there could be more anionic surfactant molecules on the surface, resulting in a further decrease in the van der Waals interaction.

Summary

In this study the silicon-silicon nitride surface interactions were investigated with AFM surface force measurements. The two surfaces show strong attraction in air, and this attraction is electrostatic in nature. An very large adhesion force is also shown in air. It implies that bare silicon wafers are easily contaminated by silicon nitride-like particles in air. The force measurements in solution generally showed reduced attraction and adhesion, suggesting that the particulate contaminants are easier to remove in solution than in air. In other words, wet cleaning is inherently better than dry cleaning. In pH 2 solution silicon nitride particles can be easily attracted by a silicon surface due to van der Waals interaction and the lack of electrostatic repulsion. After the particles are attached on the silicon surface, they are not easily detached because of the existence of an adhesion force. The attaching/detaching process is not reversible.

When CTAB is present in the solution, the attractive force gradually changes to repulsive force and the adhesion force vanishes with the increase of CTAB concentration. CTAB concentration should be not less than 500 ppm in order to prevent silicon nitride particle contamination on silicon wafer surface. CTAB forms a monolayer film on the silicon surface even when the bulk concentration is as low as 12.5 ppm. The film

structure does not change significantly with the increase of CTAB bulk concentration. The repulsive forces have two origins: the steric repulsion from the surface film structure and the electrostatic force. The steric force alone dose not effectively prevent particle deposition. The simulation results of the DLVO forces show that the CTAB molecules not only increase electrostatic repulsion, but decrease van der Waals interaction also.

The anionic surfactant is very effective in modulating silicon-silicon nitride surface interaction in pH 2 solution. Although at very low concentration the anionic surfactant increases attractive and adhesion forces, it eliminates the adhesion force and changes the attraction force to repulsion force after the bulk concentration is 50 ppm. No surface film structure was observed. This may be due to the structure of this anionic surfactant: the head group is in the middle of the hydrophobic chain. The simulation suggests that the anionic molecules adsorb strongly on the surfaces and the van der Waals interaction is further reduced.

In the whole concentration range of interest the nonionic surfactant L12-8 does not help prevent particle deposition. The surfactant does not introduce any electrostatic repulsive force. After the concentration reaches CMC, a monolayered surface structure forms on silicon nitride surface. The film introduces steric repulsive force and decreases adhesion force, but the adhesion force is still present. Once the surface film is formed, it does not change significantly with the increase of surfactant bulk concentration. The film is stronger than that formed by CTAB.

In general, the silicon-silicon nitride system in pH 2 solution with/without surfactant can be described by classic DLVO theory with the addition of steric forces. All

the three conditions, constant charge, constant potential, and intermediate (LSA), can be encountered. An interesting finding is that as long as the attraction is decreased or the repulsion is increased in approaching direction, the adhesion in retracting direction is decreased. It suggests that an additive which decreases particle deposition also help in particle removal.

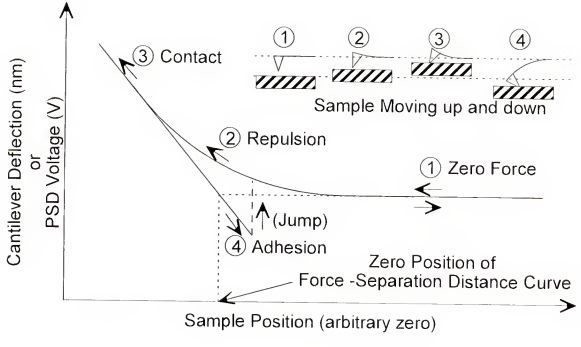

Figure 4-1. Schematic representation of cantilever deflection during sample approaching and retracting beneath a AFM tip.

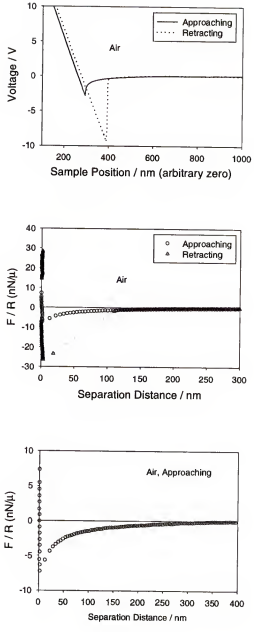

Figure 4-2. Silicon nitride tip-silicon surface interaction in air. Both approaching curve and retracting curve show strong attraction. The retracting curve shows clearly that a strong adhesion force is present. A)(top) Plots of PSD voltage versus sample position; B)(middle) Plots of the normalized force versus separation distance; C)(bottom) Plots of the normalized force versus separation distance when the sample approaches the tip.

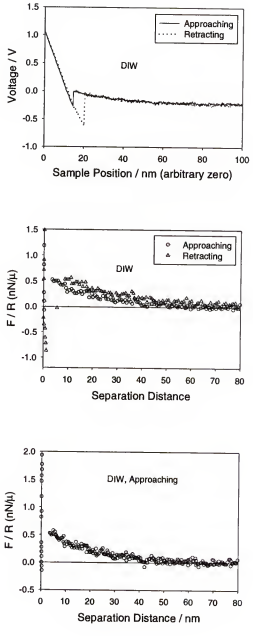

Figure 4-3. Silicon nitride tip-silicon surface interaction in deionized water. Both approaching curve and retracting curve show repulsion at long distance and attraction at short distance. The "jump-in" and "jump-off" of the tip are clearly shown. The adhesion is evident on retracting curve. A)(top) Plots of PSD voltage versus sample position; B)(middle) Plots of the normalized force versus separation distance; C)(bottom) Plots of the normalized force versus separation distance when the sample approaches the tip.

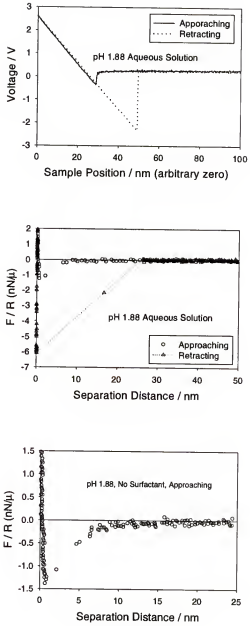

Figure 4-4. Silicon nitride tip-silicon surface interaction in pH 1.88 aqueous solution. Both approaching curve and retracting curve show attraction in the whole interaction range. The adhesion is stronger than that in DIW. A)(top) Plots of PSD voltage versus sample position; B)(middle) Plots of the normalized force versus separation distance; C)(bottom) Plots of the normalized force versus separation distance when the sample approaches the tip.

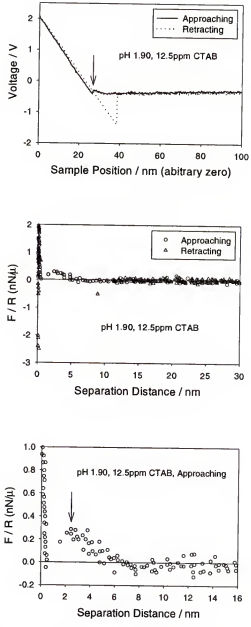

Figure 4-5. Silicon nitride tip-silicon surface interaction in 12.5 ppm CTAB pH 1.90 aqueous solution. The approaching curve shows a force barrier. The maximum of the barrier indicated by an arrow is located at about 2.5 nm from the silicon surface. The retracting curve shows clearly that an adhesion force is present. A)(top) Plots of PSD voltage versus sample position; B)(middle) Plots of the normalized force versus separation distance; C)(bottom) Plots of the normalized force versus separation distance when the sample approaches the tip.

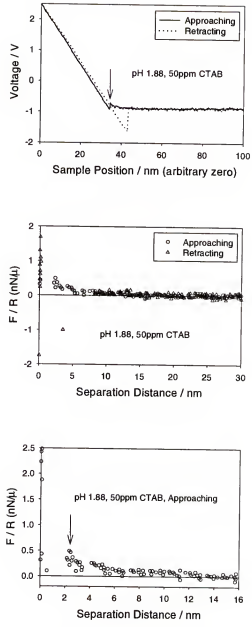

Figure 4-6. Silicon nitride tip-silicon surface interaction in 50 ppm CTAB pH 1.88 aqueous solution. The approaching curve shows a force barrier. The maximum of the barrier indicated by an arrow is located at about 2.5 nm from the silicon surface. The retracting curve shows clearly that an adhesion force is present. A)(top) Plots of PSD voltage versus sample position; B)(middle) Plots of the normalized force versus separation distance; C)(bottom) Plots of the normalized force versus separation distance when the sample approaches the tip.

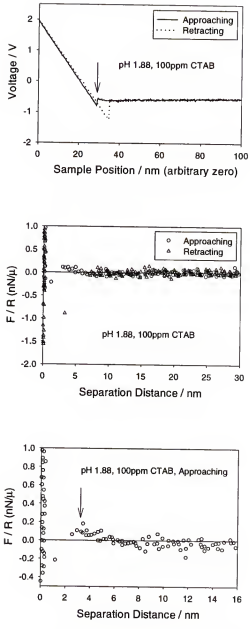

Figure 4-7. Silicon nitride tip-silicon surface interaction in 100 ppm CTAB pH 1.88 aqueous solution. The approaching curve shows a force barrier. The maximum of the barrier indicated by an arrow is located at about 3.2 nm from the silicon surface. The retracting curve shows clearly that an adhesion force is present. A)(top) Plots of PSD voltage versus sample position; B)(middle) Plots of the normalized force versus separation distance; C)(bottom) Plots of the normalized force versus separation distance when the sample approaches the tip.

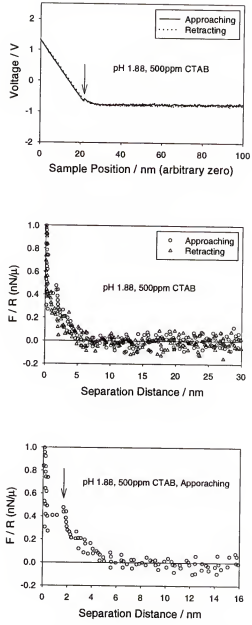

Figure 4-8. Silicon nitride tip-silicon surface interaction in 500 ppm CTAB pH 1.88 aqueous solution. The approaching curve shows a secondary force barrier. The maximum of the barrier indicated by an arrow is located at about 2.0 nm from the silicon surface. The adhesion force on retracting curve is vanished. A)(top) Plots of PSD voltage versus sample position; B)(middle) Plots of the normalized force versus separation distance; C)(bottom) Plots of the normalized force versus separation distance when the sample approaches the tip.

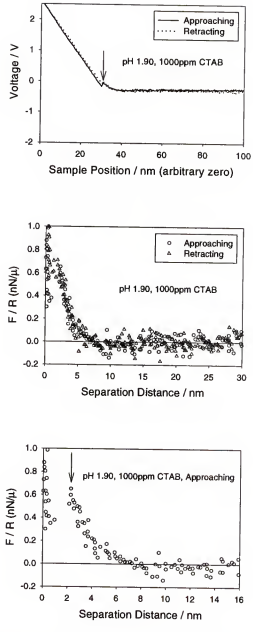

Figure 4-9. Silicon nitride tip-silicon surface interaction in 1000 ppm CTAB pH 1.90 aqueous solution. The approaching curve shows a secondary force barrier. The maximum of the barrier indicated by an arrow is located at about 2.5 nm from the silicon surface. The adhesion force on retracting curve is vanished. A)(top) Plots of PSD voltage versus sample position; B)(middle) Plots of the normalized force versus separation distance; C)(bottom) Plots of the normalized force versus separation distance when the sample approaches the tip.

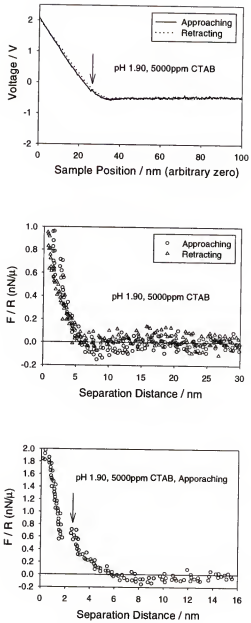

Figure 4-10. Silicon nitride tip-silicon surface interaction in 5000 ppm CTAB pH 1.90 aqueous solution. The approaching curve shows a secondary force barrier. The maximum of the barrier indicated by an arrow is located at about 3.0 nm from the silicon surface. The adhesion force on retracting curve is vanished. A)(top) Plots of PSD voltage versus sample position; B)(middle) Plots of the normalized force versus separation distance; C)(bottom) Plots of the normalized force versus separation distance when the sample approaches the tip.

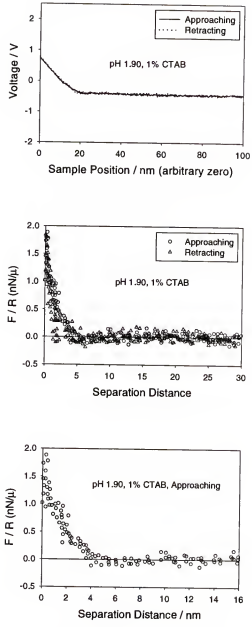

Figure 4-11. Silicon nitride tip-silicon surface interaction in 1% CTAB pH 1.90 aqueous solution. The secondary force barrier is vanished on the approaching curve, and only a exponentially increasing force is present when the two surfaces approach one another. The adhesion force on retracting curve is vanished. A)(top) Plots of PSD voltage versus sample position; B)(middle) Plots of the normalized force versus separation distance; C)(bottom) Plots of the normalized force versus separation distance when the sample approaches the tip.

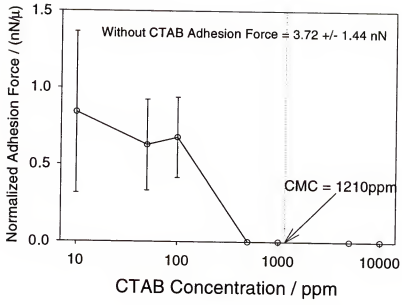

Figure 4-12. Plot of silicon-silicon nitride adhesion force as a function of CTAB concentration. The CTAB CMC is about 1210 ppm at room temperature. Without CTAB the adhesion force is 3.72 ± 1.44 nN/μ. After adding CTAB the adhesion force decreases significantly. At low concentration up to 100 ppm the adhesion force is about the same with a value around 0.7 nN/μ. The adhesion force decrease rapidly to zero when CTAB concentration changes from 100 ppm to 500 ppm. It remain zero when CTAB concentration exceeds 500 ppm.

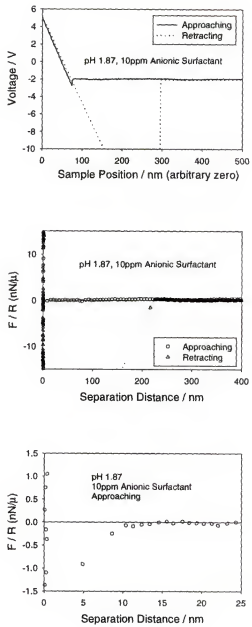

Figure 4-13. Silicon nitride tip-silicon surface interaction in 10 ppm anionic surfactant pH 1.87 aqueous solution. The approaching curve indicates an attractive force near the surface. The retracting curve shows a very large adhesion force. A)(top) Plots of PSD voltage versus sample position; B)(middle) Plots of the normalized force versus separation distance; C)(bottom) Plots of the normalized force versus separation distance when the sample approaches the tip. The attractive force starts at about 10 nm separation.

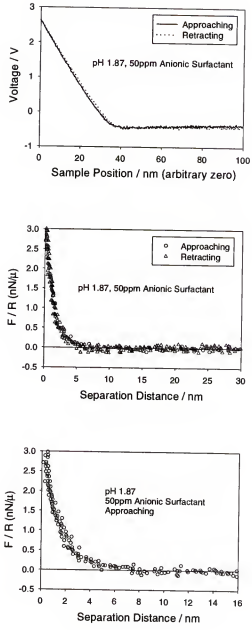

Figure 4-14. Silicon nitride tip-silicon surface interaction in 50 ppm anionic surfactant pH 1.87 aqueous solution. Both approaching curve and retracting curve overlap, indicating a reversible process. The intersurface force becomes repulsive. A)(top) Plots of PSD voltage versus sample position; B)(middle) Plots of the normalized force versus separation distance; C)(bottom) Plots of the normalized force versus separation distance when the sample approaches the tip.

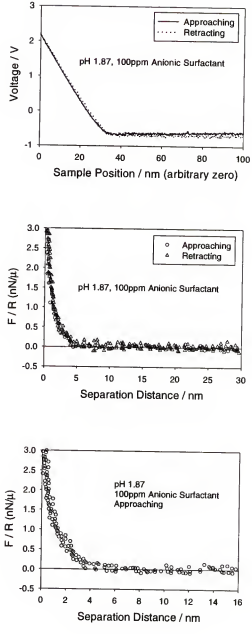

Figure 4-15. Silicon nitride tip-silicon surface interaction in 100 ppm anionic surfactant pH 1.87 aqueous solution. Both approaching curve and retracting curve overlap, indicating a reversible process. The intersurface force is repulsive. A)(top) Plots of PSD voltage versus sample position; B)(middle) Plots of the normalized force versus separation distance; C)(bottom) Plots of the normalized force versus separation distance when the sample approaches the tip.

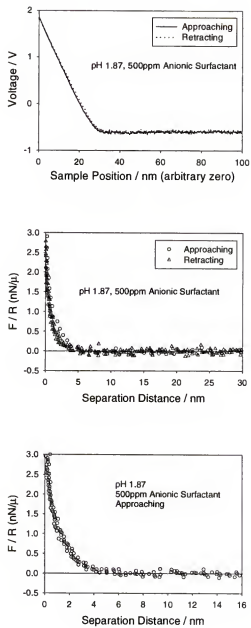

Figure 4-16. Silicon nitride tip-silicon surface interaction in 500 ppm anionic surfactant pH 1.87 aqueous solution. Both approaching curve and retracting curve overlap, indicating a reversible process. The intersurface force is repulsive. A)(top) Plots of PSD voltage versus sample position; B)(middle) Plots of the normalized force versus separation distance; C)(bottom) Plots of the normalized force versus separation distance when the sample approaches the tip.

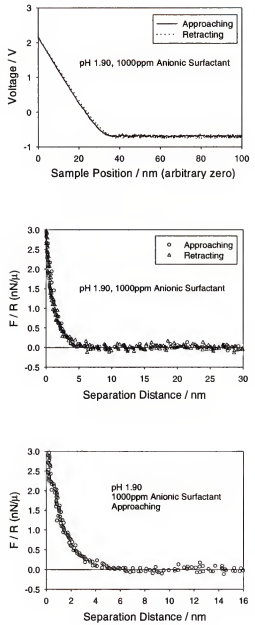

Figure 4-17. Silicon nitride tip-silicon surface interaction in 1000 ppm anionic surfactant pH 1.90 aqueous solution. Both approaching curve and retracting curve overlap, indicating a reversible process. The intersurface force is repulsive. A)(top) Plots of PSD voltage versus sample position; B)(middle) Plots of the normalized force versus separation distance; C)(bottom) Plots of the normalized force versus separation distance when the sample approaches the tip.

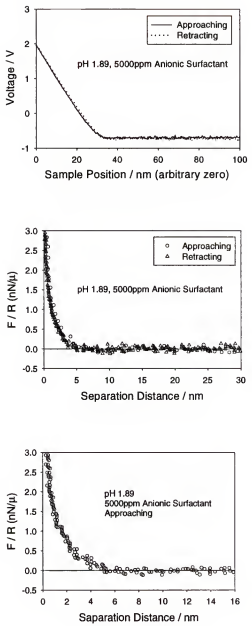

Figure 4-18. Silicon nitride tip-silicon surface interaction in 5000 ppm anionic surfactant pH 1.89 aqueous solution. Both approaching curve and retracting curve overlap, indicating a reversible process. The intersurface force is repulsive. A)(top) Plots of PSD voltage versus sample position; B)(middle) Plots of the normalized force versus separation distance; C)(bottom) Plots of the normalized force versus separation distance when the sample approaches the tip.

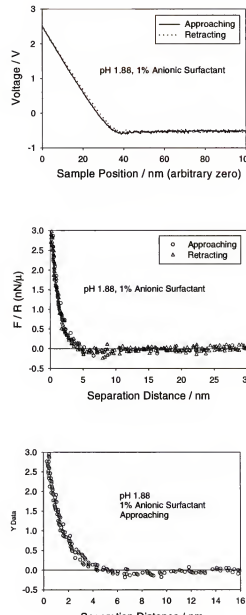

Figure 4-19. Silicon nitride tip-silicon surface interaction in 1 % anionic surfactant pH 1.88 aqueous solution. Both approaching curve and retracting curve overlap, indicating a reversible process. The intersurface force is repulsive. A)(top) Plots of PSD voltage versus sample position; B)(middle) Plots of the normalized force versus separation distance; C)(bottom) Plots of the normalized force versus separation distance when the sample approaches the tip.

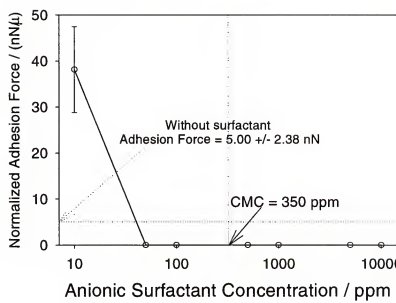

Figure 4-20. The plot of silicon-silicon nitride surface normalized adhesion force as a function of the anionic concentration. At 10 ppm surfactant concentration the adhesion force increases significantly. When the concentration exceeds 50ppm, the adhesion force is not observed.

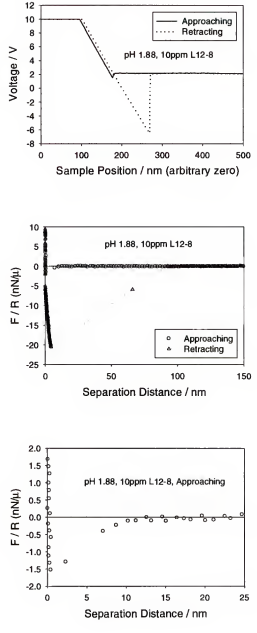

Figure 4-21. Silicon nitride tip-silicon surface interaction in 10 ppm L12-8 pH 1.88 aqueous solution. The approaching curve shows a attractive force near the surface. The retracting curve shows a very strong adhesion force. A)(top) Plots of PSD voltage versus sample position; B)(middle) Plots of the normalized force versus separation distance; C)(bottom) Plots of the normalized force versus separation distance when the sample approaches the tip. The attractive force starts at about 12 nm from the surface.

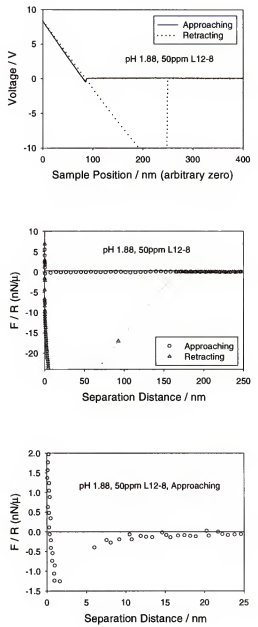

Figure 4-22. Silicon nitride tip-silicon surface interaction in 50 ppm L12-8 pH 1.88 aqueous solution. The approaching curve shows a attractive force near the surface. The retracting curve shows a very strong adhesion force. A)(top) Plots of PSD voltage versus sample position; B)(middle) Plots of the normalized force versus separation distance; C)(bottom) Plots of the normalized force versus separation distance when the sample approaches the tip. The attractive force starts at about 12 nm from the surface.

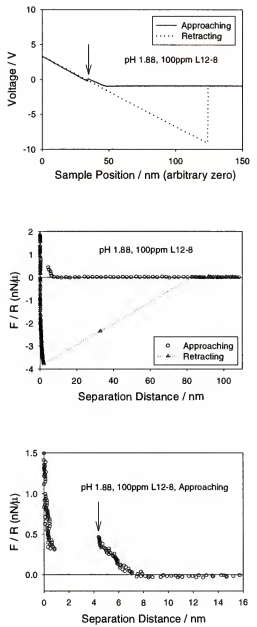

Figure 4-23. Silicon nitride tip-silicon surface interaction in 100 ppm L12-8 pH 1.88 aqueous solution. The approaching curve shows a repulsive barrier near the surface as indicated by the arrow. The retracting curve still shows an adhesion force. A)(top) Plots of PSD voltage versus sample position; B)(middle) Plots of the normalized force versus separation distance; C)(bottom) Plots of the normalized force versus separation distance when the sample approaches the tip. The maximum of the barrier locates at about 4.3 nm from the surface.

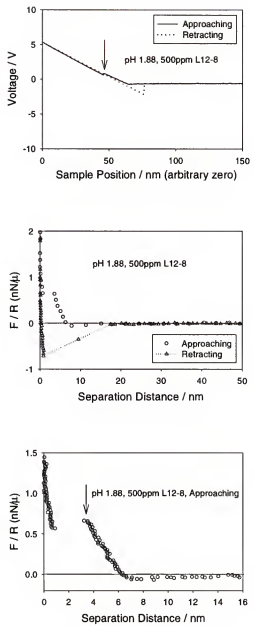

Figure 4-24. Silicon nitride tip-silicon surface interaction in 500 ppm L12-8 pH 1.88 aqueous solution. The approaching curve shows a repulsive barrier near the surface as indicated by the arrow. The retracting curve still shows an adhesion force. A)(top) Plots of PSD voltage versus sample position; B)(middle) Plots of the normalized force versus separation distance; C)(bottom) Plots of the normalized force versus separation distance when the sample approaches the tip. The maximum of the barrier locates at about 3.8 nm from the surface.

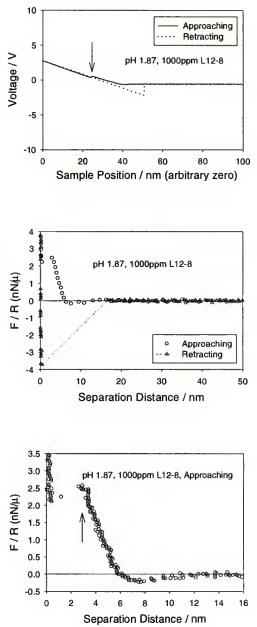

Figure 4-25. Silicon nitride tip-silicon surface interaction in 1000 ppm L12-8 pH 1.87 aqueous solution. The approaching curve shows a repulsive barrier near the surface as indicated by the arrow. The retracting curve still shows an adhesion force. A)(top) Plots of PSD voltage versus sample position; B)(middle) Plots of the normalized force versus separation distance; C)(bottom) Plots of the normalized force versus separation distance when the sample approaches the tip. The maximum of the barrier locates at about 3.0 nm from the surface.

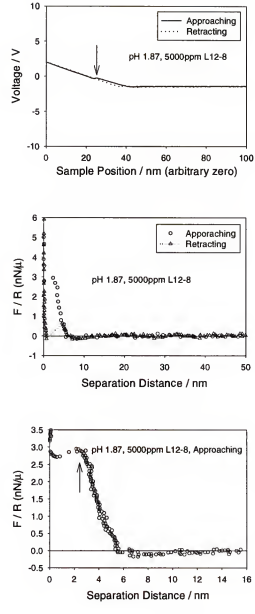

Figure 4-26. Silicon nitride tip-silicon surface interaction in 5000 ppm L12-8 pH 1.87 aqueous solution. The approaching curve shows a repulsive barrier near the surface as indicated by the arrow. The adhesion force on the retracting curve is not obvious in this graph, but the magnitude varies from run to run. A)(top) Plots of PSD voltage versus sample position; B)(middle) Plots of the normalized force versus separation distance; C)(bottom) Plots of the normalized force versus separation distance when the sample approaches the tip. The maximum of the barrier locates at about 2.8 nm from the surface.

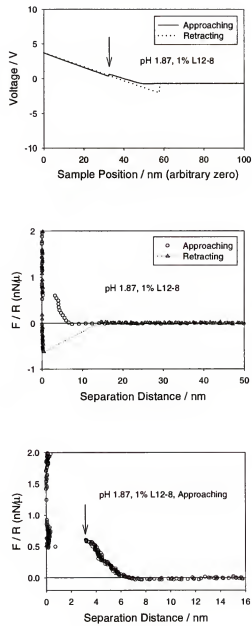

Figure 4-27. Silicon nitride tip-silicon surface interaction in 1 % L12-8 pH 1.87 aqueous solution. The approaching curve shows a repulsive barrier near the surface as indicated by the arrow. The retracting curve still shows an adhesion force. A)(top) Plots of PSD voltage versus sample position; B)(middle) Plots of the normalized force versus separation distance; C)(bottom) Plots of the normalized force versus separation distance when the sample approaches the tip. The maximum of the barrier locates at about 3.5 nm from the surface.

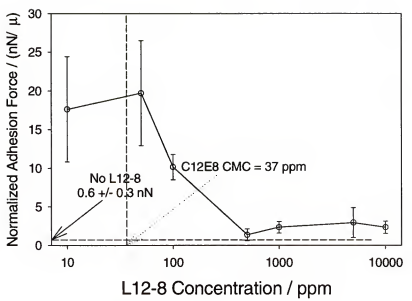

Figure 4-28. Plot of silicon-silicon nitride surface normalized adhesion force as a function of L12-8 concentration. Three regions are obvious: 1) 10 - 50 ppm region: constant high adhesion; 2) 50 - 500 ppm: transient region; 3) 500 ppm - 1 %: constant low adhesion.

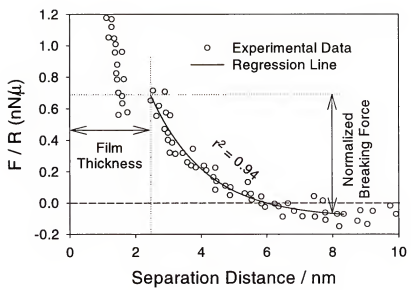

Figure 4-29. Plot of normalized force as a function of separation distance in approaching direction in CTAB solution. It shows a surface film structure. The film thickness and the breaking force of this surface film structure is illustrated in the graph. Three parameter regression, y=y0+a*exp(b*x), shows good agreement with the experimental data. Detailed discussion is in text.

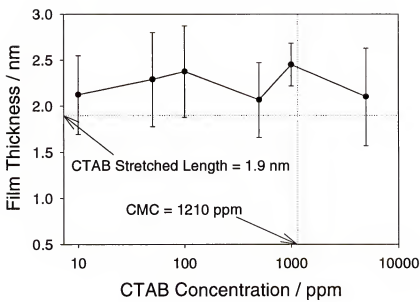

Figure 4-30. Plot of CTAB film thickness as a function of bulk concentration. The film thickness does not change with bulk concentration. The film thickness is comparable with the length of a stretched CTAB molecule, suggesting a monolayer film. The film forms at a concentration far below CMC.

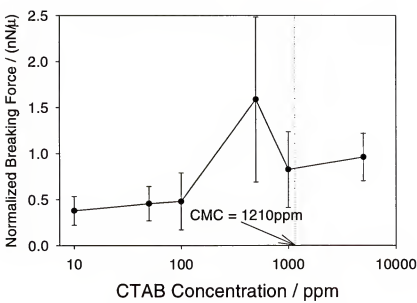

Figure 4-31. Plot of normalized breaking force of the CTAB surface film as a function of CTAB bulk concentration. The required breaking force increases slightly with the increasing of CTAB concentration, suggesting that the film become a little bit denser with bulk concentration increases.

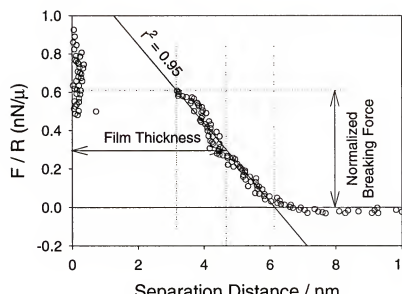

Figure 4-32. Plot of normalized force as a function of separation distance in approaching direction in L12-8 solution. It shows a surface film structure. The film thickness and the breaking force of this surface film structure is illustrated in the graph. Linear regression shows good agreement with the experimental data. Detailed discussion is in text.

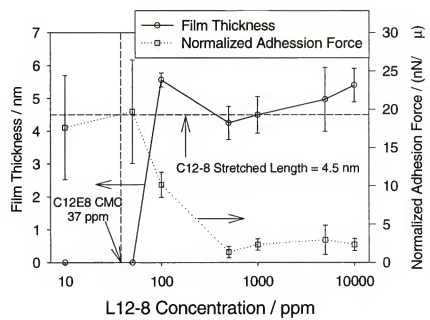

Figure 4-33. Plot of L12-8 film thickness and adhesion force as a function of bulk concentration. Once it is formed the film thickness does not change with bulk concentration. The film thickness is comparable with the length of a stretched C12E8 molecule, which is the mean component of the surfactant, suggesting a monolayer film. The film forms at a concentration near CMC. The film formation inversely correlates with adhesion force between silicon and silicon nitride surfaces.

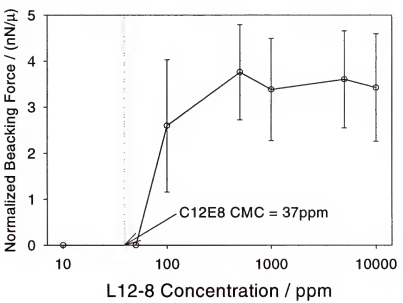

Figure 4-34. Plot of normalized breaking force of the L12-8 surface film as a function of L12-8 bulk concentration. The required breaking force does not increase with the increasing of L12-8 concentration once the film is formed.

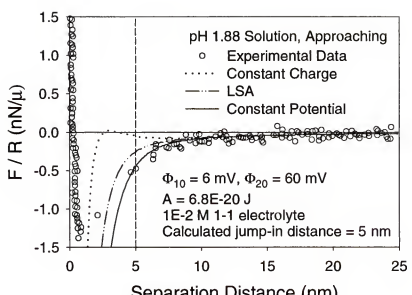

Figure 4-35. Plot of normalized force as a function of separation distance in approaching direction in pH 2 solution. Constant potential simulation gives the best fitting. The surface potentials are 6 mV and 60 mV, respectively, and the Hamaker constant is 6.8E-20 J. The background electrolyte is 1-1 type and 1E-2 M (pH=2). The calculated jump-in distance is 5.0 nm, shown as the dashed vertical line.

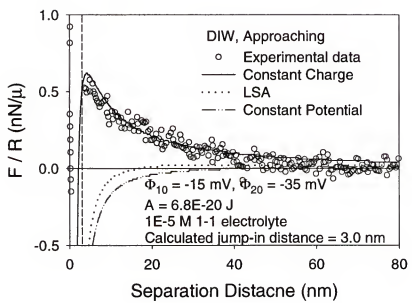

Figure 4-36. Plot of normalized force as a function of separation distance in approaching direction in DIW. Constant charge simulation gives the best fitting. The surface potentials are -15 mV and -35 mV, respectively, and the Hamaker constant is 6.8E-20 J. The background electrolyte is 1-1 type and 1E-6 M. The calculated jump-in distance is 3.0 nm, shown as the dashed vertical line.

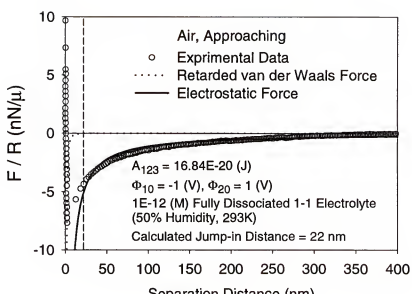

Figure 4-37. Plot of normalized force as a function of separation distance in approaching direction in air. The large attractive force is due to electrostatic interaction. The simulation is done under constant potential condition. The surface potentials are -1 V and 1 V, respectively. They are solely for illustration purpose. The Hamaker constant is 16.84E-20 J. The background electrolyte is 1-1 type and 1E-12 M, based on the argument of 50% humidity in 20 °C (detailed discussion can be found in the text). The calculated jump-in distance is 22.0 nm, shown as the dashed vertical line.

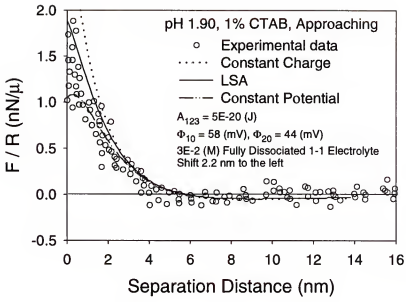

Figure 4-38. Plot of normalized force as a function of separation distance in approaching direction in pH 1.90 1 % CTAB solution. The noise of the experimental data is quite large. All the simulation give similar results, but the interaction appears that both charges and potentials are modulating. The surface potentials are 44 mV and 58 mV, respectively. The Hamaker constant is 5E-20 J. The background electrolyte is 1-1 type and 3E-2 M. The simulated curves are shifted 2.2 nm to the left. There is no jump-in observed.

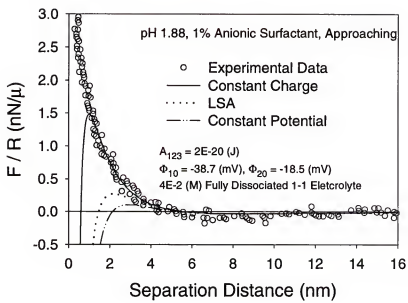

Figure 4-39. Plot of normalized force as a function of separation distance in approaching direction in pH 1.88 1 % anionic surfactant solution. The constant charge simulation gives the best fitting. The surface potentials are -18.5 mV and -38.5 mV, respectively. The Hamaker constant is 2E-20 J. The background electrolyte is 1-1 type and 4E-2 M. There is no jump-in observed.

CHAPTER 5
PREFERENTIAL DEPOSITION OF COPPER ONTO SILICON WAFER SURFACE FROM HF SOLUTION

Introduction

In Chapters 3 and 4 we discussed the mechanism and prevention of particulate contamination of silicon wafers in dilute HF solution. As discussed in Chapter 2, noble metal contamination of silicon wafers in dilute HF is also a critical issue. Therefore, after we discussed particle contamination, we will focus on noble metal contamination in the following studies. In this Chapter, we will concentrate on the study of the mechanism of copper ions preferential deposition from dilute HF solutions on silicon wafer surfaces.

The mechanism of copper deposition has been intensively studied and understood quite well [Ker90, Hsu92, Mor94, Obe94, Tor95, Chy96, Tee96a, Nor97, Li98, Che98]. It is widely accepted that copper deposition from HF solution is through a redox reaction with silicon

$$2Cu^{2+} + Si + 6HF = H_2SiF_6 + 2Cu\downarrow + 4H^+ \qquad (5\text{-}1)$$

in which the copper ions having higher reducing potential than silicon withdraw electrons from the silicon surface. Copper deposits on the silicon surface as metal particles while localized oxidation of silicon forms pits on silicon surface. The reduction of cupric ions by silicon is thermodynamically favorable.

The surface copper contamination is linearly proportional to bulk copper concentration and to square root of dipping time. Therefore, the reaction kinetics are believed to be diffusion-controlled. The deposited copper is in the shape of isolated particles. Figure 5-1 is an AFM micrograph of copper deposited silicon surface (10 min deposition time). The solution was 0.5% HF with 100 ppb copper ions. It shows that the deposited copper is in particle form, and pits are seen below the copper particles. After dipping, the surface roughness of the wafer increases significantly. A typical SEM image of a silicon surface after copper contamination at high contamination level (10 ppm) is given in Figure 5-2. The silicon surface was not intentionally damaged before copper contamination. It shows that the particles are uniformly distributed on the surface.

However, the existing models did not explain the phenomenon that copper sometimes preferentially deposits on certain region of silicon wafer. Figure 5-3 shows one SEM image after a 10 min copper deposition in 0.5% HF solution with 10 ppm bulk copper concentration. In the center of the pattern, a large pit is formed. Next to the large pit, one observes a large particle followed by a fine particle region with the mean particle diameter less than 50 nm. Outside this fine particle region there is a coarse particle region with the mean particle diameter about 100 nm. Beyond these particles a sharp boundary between the deposited particles and pristine undeposited area is clearly seen.

Figure 5-4 shows a big pit caused by copper deposition in 0.5% HF solution with 10 ppm bulk copper contamination. It can be clearly seen that a 0.8 μ crystalline particle sits at the bottom of a 3 μ wide pit. At the edge of the pit there are many smaller particles, and in the vicinity of the pit even smaller particles can be observed. Some distance away

from the pit the particles disappear. The SEM micrograph in Figure 5-5 reveals a more interesting phenomenon. The deposited particles are arranged in lines. The straight lines with perpendicular propagating directions cannot be formed by water retrieval. Higher magnification micrographs of the aligned particles are in Figure 5-6, which is a portion of the thinner line in Figure 5-5. Cu Kα and Si Kα x-ray mapping in Figure 5-6 indicate that these alined particles are indeed copper particles. The deposition condition was also 0.5% HF solution with 10 ppm bulk copper concentration.

The preferential deposition of copper on the n-type regions of p-n junctions was reported [Who58]. Nevertheless, observations seemingly contradictory to these were also reported that the pits occured preferentially on the p-type regions [Chu97]. Torcheux et al. reported that pitting corrosion of polysilicon dissolution occurred while the surrounding structure remained intact [Tor95]. Other reports have indicated that copper contamination was a function of wafer quality, and ring-shaped pattens were observed after metal spiking [Hey93, Hou89]. The mechanism discussed above is not enough to explain these observations. It has only been speculated that defect-enhanced nucleation could be the cause of preferential deposition [Hey93]. Copper deposition has two stages: nucleation and particle growth. The reported diffusion limited mechanism deals with the particle growth stage. However, in actual processes the copper contamination level is lower than 1ppm and the wafer-solution contact time is short so that copper deposition is limited only to nucleation stage [Mor94]. Therefore, copper particle nucleation is more relevant to copper contamination in real fabrication processes.

It is thus the aim of this study to find unequivocal experimental evidence to test the defect-induced nucleation postulation. The biggest ambiguity of the defect-induced nucleation assumption lies in that the natural defect sites on silicon wafer surface are not easily known before copper deposition. Therefore, the key issue to check the assumption is to introduce defects intentionally on silicon surface at easily identifiable locations. This is done by two methods. On is to scratch the silicon surface to produce mechanical defects. The other is to use ion bombardment to create irradiation defects. Both of these methods can introduce localized defects. It was found that copper preferentially deposited on these structurally modified regions.

Experimental

The wafers were test grade 2 inch n-type Si(100) wafers with resistivity 1 - 10 Ohm·cm from Silicon Quest International. They were cut into 1 × 1 cm^2 pieces. Before they were dipped into HF solutions, the wafer pieces were cleaned by a standard SC-1 cleaning to remove particles, then followed by a DIW rinse and nitrogen blow dry. Some wafer pieces were scratched on the surface using a diamond scriber from Ted Pella. The scratching was done before SC-1 cleaning. The HF solutions contained 0.5 wt. % HF and 10ppm Cu^{2+} intentionally contaminated from 1000ppm atomic absorption spectroscopy copper standard solution. The dipping time was 10 min and a 25W Leica incandescent lamp was used to illuminate samples. scanning electron microscopy (SEM) and electron dispersion spectroscopy (EDS) studies were done with a JEOL 6400 SEM. All samples were normal to the electron beam during SEM and EDS measurements. X-ray mapping

was performed by choosing the wavelength window containing the characteristic Kα lines of the element under study.

For those samples on which the defects were generated by ion bombardment and characterized with the transmission electron microscopy (TEM), the silicon wafer pieces were further cut to round shape with 3 mm in diameter. These pieces then were subjected to mechanical grinding and dimpling. In order to obtain high defect density regions the ion milling with a 6 KeV argon ion beam and an incidence angle of 13° for up to 10 hours was conducted. Before ion milling, a 10 min SC-1 clean was employed to remove any particles and organic contaminants on the sample surfaces. When ion milling was finished, one sample was dipped into a 0.5% HF solution without copper contamination and two samples were dipped into 0.5% HF solution which was intentionally contaminated by atomic absorption spectroscopy (AAS) standard Cu^{2+} solution for 20 min. The copper bulk concentration was 100ppb. In order to increase copper deposition, a 25 W Leica incandescent lamp was also used. After the HF bath, the samples were cleaned with DI water. Transmission electron microscopy measurements were conducted using a JEOL 200X instrument operating at 200kV.

Results and Discussion

SEM micrographs of the unscratched silicon surface after copper contamination have been shown in Figures 5-2, 5-3, 5-4, 5-5, and 5-6. For many samples the copper particles are uniformly distributed on the surfaces (Figure 5-2), but for others the nonuniformities are seen as localized deposition (Figures 5-3 and 5-4) or particle

alignment (Figures 5-5 and 5-6). The SEM micrograph of an scratched silicon surface after copper contamination is in Figure 5-7. The scratched pattern was the letters "UF". We can see that particles preferentially deposits along the scratched lines. X-ray mappings indicate that these particles are indeed copper particles. The deposited copper particles beyond the scratched lines are far fewer than those along the lines. This shows that copper will be preferentially deposited on the areas with high defect density. It should be noted that the background white dots in (b) are due to noise in the x-ray signal, because the copper signal was very weak. The micrographs of the same surface with higher magnification are shown in Figure 5-8. They clearly show that the detailed scratching pattern has been destroyed after copper deposition.

TEM study also confirms this statement. Figure 5-9a shows the TEM bright field micrograph from a bare silicon sample that has not been contaminated by copper. It shows the presence of two regions; near the hole a contrast-free image is obtained while at distance further from the hole bend contours are clearly visible. The bend contours disappear near the edge of the hole, thereby indicating a microstructure transformation from a crystalline to an amorphous matrix. The presence of an amorphous region near the hole can be further confirmed by the diffuse rings obtained from selected area diffraction (SAD) patterns (Figure 5-9b).

Figure 5-10 shows bright field images and SAD pattern obtained after copper outplating. The figure shows deposition of nanoparticles in the amorphous region of the sample. No particles are deposited on the crystalline region where the bend contours are evident. A sharp boundary for particle deposition corresponds to amorphous-crystalline

interface of the matrix. The SAD pattern (Figure 5-10b) shows that these particles were crystalline, as confirmed by the presence of diffraction spots and diffracting rings which are superimposed on a diffuse ring pattern from the substrate. The polycrystalline-like diffraction is indexed and the values listed in Table 5-1. The table clearly shows that the diffraction pattern corresponds to the fcc copper. No specific orientation relationship was observed among the deposited particles. The size distribution of the copper particles can be clearly shown by higher magnification micrograph (Figure 5-10c). The micrograph shows that particles are typically spherical in shape with sizes varying from 5 nm to 60 nm. The contrast from the particles also suggests that the particles are typically polycrystalline in nature. Two contaminated samples gave similar results, only particle densities had some variation.

Table 5-1. Index of SAD pattern in Figure 5-9.

Ring #	Index	Radius/mm (calc.)	Radius/mm (mea.)	Err %
#1	{111}	9.86	9.6	-2.6
#2	{200}	11.39	11.1	-2.5
#3	{220}	16.11	15.9	-1.3
#4	{311}	18.89	18.8	-0.5
--	{222}	19.73	--	--
--	{400}	22.78	--	--
#5	{331}	24.82	24.9	0.3
--	{420}	25.46	--	--
#6	{422}	27.90	27.8	-0.4
#7	{333}	29.59	29.5	-0.3

L=820mm, λ = 0.0251Å, a(Cu) = 3.6146Å.

Both SEM and TEM studies clearly suggest that copper will be preferentially deposited on the areas with high defect density. Hence, it could be the reason of two contradictory observations: both n-type and p-type preferences of copper deposition / pitting at p-n junctions have been reported previously [Who58, Chu97]. The cause of preferential deposition is not due to doping type, but rather by the defects induced by ion implantation. Our observations are also in agreement with the results of Torcheux et al [Tor95]. They reported preferential pitting on a polysilicon emitter. Here the boundaries enhance corrosion. It would be interesting to go back and see Figures 5-3, 5-4, 5-5, and 5-6, in which the big pits could have been initiated by localized surface defects and the particle alignments could have been due to very sallow surface cracking caused when the piece was cut from the wafer.

Summary

We showed in this microscopic study that the copper preferential deposition on silicon surface from HF solution is caused by defect-enhanced nucleation. Copper was found to deposit only on defect sites which were artificially induced by surface scratching or ion bombardment. They serve as direct experimental proof of the hypothesis that defects will enhance copper contamination. Previously inconsistent results thus may be understood. This work also suggests that in order to decrease copper contamination on silicon surface, the defect sites such as ion-implanted areas or polysilicon area should be more carefully protected.

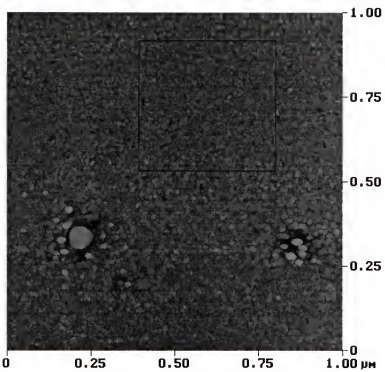

Figure 5-1. AFM image of a 100ppb Cu + 0.5% HF 10 min dipped silicon surface. The particles and the pits under the particles are clearly shown. Z range: 10 nm; boxed region: Rms = 0.655 nm, Ra = 0.514 nm; before dipping Rms = 0.25nm, Ra = 0.5 nm.

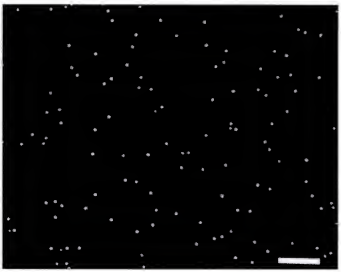

Figure 5-2. A typical SEM micrograph of a unscratched silicon surface after copper contamination. The sizes and distribution of copper particles are uniform. Deposition condition: 0.5% HF + 10 ppm Cu 10 min under illumination. The scale bar is 10 micron.

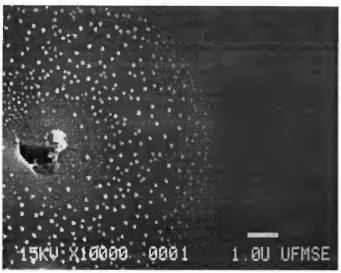

Figure 5-3. SEM image of a unscratched silicon surface after copper outplating. Note the formation of the copper pattern and a sharp boundary. Deposition condition: 0.5% HF + 10ppm Cu 10 min under illumination.

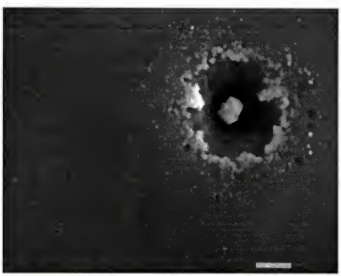

Figure 5-4. SEM micrograph of a unscratched silicon surface after copper contamination. A big pit and copper particles in and around it are shown. Deposition condition: 0.5% HF + 10 ppm Cu 10 min under illumination. The scale bar is 10 micron.

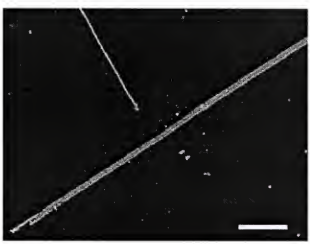

Figure 5-5. A SEM micrograph of a unscratched silicon surface after copper contamination. Most copper particles are aligned into two perpendicular lines, others are rather uniformly distributed on the surface. Deposition condition: 0.5% HF + 10 ppm Cu 10 min under illumination. The scale bar is 20 micron.

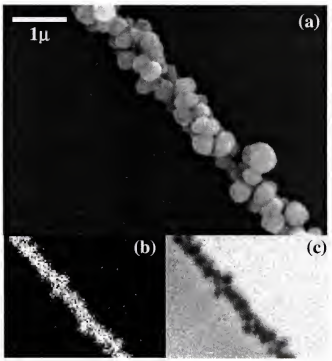

Figure 5-6. Micrographs of a unscratched silicon surface after copper contamination. They are one portion of the thinner line in Figure 5-5. (a) SEM image, (b) Cu Kα X-ray image, and (c) Si Kα X-ray image. The aligned particles are copper particles.

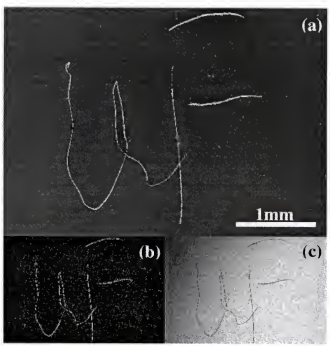

Figure 5-7. Micrographs of a scratched silicon surface after copper contamination. The scratched lines are the letters "UF", and copper is preferentially deposited along the scratched lines. (a) SEM image, (b) Cu Kα X-ray image, and (c) Si Kα X-ray image. The background wight dots in (b) are from noise because the copper signal was very weak.

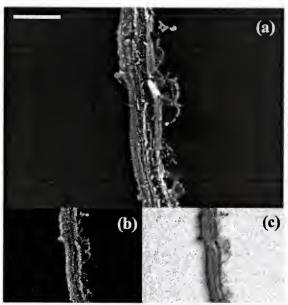

Figure 5-8. Magnified micrographs of a scratched silicon surface in Figure 5-7.Copper particles cover the scratched areas totally. (a) SEM image, (b) Cu Kα X-ray image, and (c) Si Kα X-ray image. The scale bar is 10 micron.

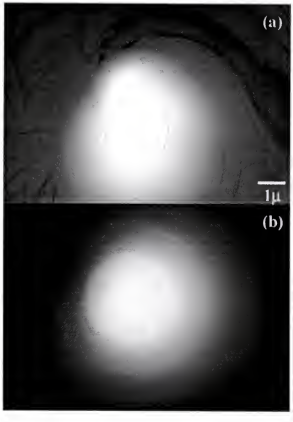

Figure 5-9. Ion bombardment modified silicon surface. (a)TEM bright field image and (b)SAD pattern of the region near the hole generated by ion milling. The edge of the hole becomes amorphous while other regions the crystalline is still maintained. The scale bar in (a) is 1 micron.

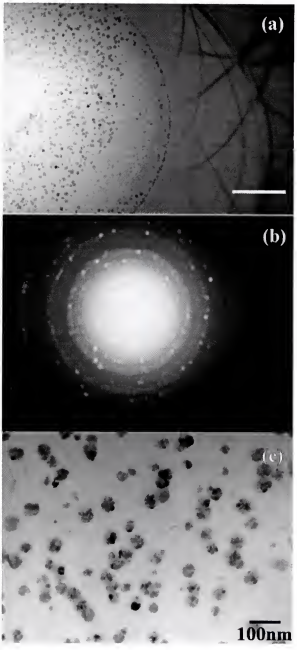

Figure 5-10. Ion-bombarded silicon surface micrographs after copper contamination. (a)TEM bright field image, (b)SAD pattern of deposited particles, and (c) Higher magnification images of the particles. The particles are preferentially deposited on amorphous region. The particles are fcc copper particles. The scale bar in (a) is 1 micron.

CHAPTER 6
NOVEL IN SITU TECHNIQUE TO CHARACTERIZE COPPER OUTPLATING FROM HF SOLUTIONS ONTO SILICON SURFACES

Introduction

In the last chapter we discussed the preferential nucleation of copper ions on silicon wafer surfaces in HF solution. Our ultimate goal is to find a method to reduce copper outplating on silicon wafer surfaces from HF solutions. In order to judge weather a method is effective to reduce copper outplating or not, we have to find a technique which can inform us, even qualitatively, how much copper is on the silicon surfaces after dilute HF cleaning. In this chapter, we present a novel technique to in situ characterize copper outplating from HF solutions onto silicon wafer surfaces.

The Characterization of surface copper contamination is usually conducted by employing total reflectance x-ray fluorescence (TXRF) or inductively coupled plasma mass spectrometry (ICP-MS) [Hoc89, Hen99]. Recently, Chyan et al. reported a new potentiometric sensor for the detection of trace metallic contaminants in HF solution [Chy96b]. They found that metal ions that can oxidize silicon shift the open circuit potential (OCP) of a silicon electrode positively. The detection limits using this technique was reported to be in part-per-trillion to part-per-billion range. We have further extended these measurements to determine the copper contamination nature of silicon in dilute HF

baths. It should be noted that during our study, we found that among other electrochemical techniques such as stripping voltammetry and impedance measurements, the OCP measurement was the best method to in situ characterize copper outplating onto silicon wafer surfaces.

There have been several reports of copper outplating in DHF bath. Several factors have been found to affect the rate of copper outplating. Some of the factors include doping type, doping level and illumination during DHF cleaning [Tee95, Tee96, Ohm93]. Illumination has been found to drastically increase the copper outplating rate. Highly doped n-type silicon wafers have been found to be more susceptible to copper contamination than highly doped p-type wafers. There have been also several studies which have shown that the addition of additive like H_2O_2 [Chu97, Ohm93], HCl [Chu97, Tee96], and HNO_3 [Rot95] significantly decrease the copper outplating.

We have also shown with our in situ technique that copper contamination on n-type wafers is more severe than on p-type wafers. Additives such as H_2O_2 , HCl, and HNO_3 are effective in decreasing copper outplating. This technique has a sensitivity of surface copper concentration caused by 5ppb bulk copper, and has at least three orders of magnitude dynamic range. The mechanism of OCP response to bulk copper ions is explained by using mixed potential theory.

Experimental

Two inch (100) n-type and p-type silicon wafers with 1-10 ohm·cm resistivity (Silicon Quest International) were subject to SC-1 cleaning, dilute HF cleaning and DI water rinse to remove particles and chemical oxide before being mounted on a custom-made TEFLON electrochemical cell. Only the polished side of a wafer was contacted with solution, and the back side was electrically contacted to a stainless steel base that had a stainless steel connection to the outside. For n-type wafers, ohmic contact was made by coating a thin film of eutectic Ga-In alloy (Alfa Aesar) between the back side of the wafer and the metal base. For p-type wafers no Ga-In alloy was used. A HF resistant Ag/AgCl reference electrode (Fisher Scientific) was positioned near the wafer. 50 ml 0.5 wt. % solutions with/without additives were used in the cell. In order to detect copper outplating, lamp illumination on the silicon electrode was carefully controlled. In our setup a 25 W Leica incandescent lamp was employed and the light was directly shed onto the wafer. Copper was added by using 1000 ppm atomic absorption spectroscopy (AAS) standard (Fisher Scientific) to different final bulk concentrations. Each time when Cu was added, the solution was gently shaken until it appeared well mixed. The OCP change with time was recorded using a CHI 660 Electrochemical work station. After 15 minutes, more Cu was added to the solution and the above processes were repeated. To regenerate silicon wafer electrode, a 5ml 5% HF + 5% HNO_3 + 5% H_2O_2 (wt.) was employed to remove surface Cu.

Results and Discussion

The OCP Change with Cu Addition

The OCP change with Cu addition is plotted in Figure 6-1. It shows that the OCP change correlates well with the bulk Cu concentration. Every time right after Cu is added, the OCP increases suddenly, and then gradually decreases to a relative stable value after 15 minutes when more Cu is added. After DI water rinse and fresh 0.5% HF without Cu contamination is used, the OCP does not decrease significantly. It suggests that the OCP response is caused by surface Cu not bulk Cu. This statement is further verified by the results plotted in Figure 6-2 in which the stripping solution is used to dissolve surface Cu, and the OCP in fresh 0.5% HF goes back to about original value.

Figure 6-3 plots the OCP change as a function of the logarithm of bulk Cu concentration. The least square regression result shows that the relationship between OCP change and log[Cu/ppb] is linear with $r^2 = 0.99$. Our experiments indicate that the linear relationship and the slope are repeatable but the absolute OCP value varies from run to run (Figure 6-5 and Figure 6-6). The linear relationship could be described phenomenologically by the equation

$$OCP - k \log[Cu] = const. \qquad (6\text{-}1)$$

Now consider two states, say initial state and final state, then apply Eq.6-1 one will get

$$OCP_f - k \log[Cu]_f = OCP_i - k \log[Cu]_i \qquad (6\text{-}2)$$

that is

$$\Delta OCP = OCP_f - OCP_i = -k \log[Cu]_i + k \log[Cu]_f \qquad (6\text{-}3)$$

Equation 6-3 simulates the regression results with -klog[Cu]$_i$ as the intercept. However, this treatment attributes the line shift (Figures 6-5 and 6-6) only to the initial Cu concentration caused by unintentional contamination. This may not be absolutely correct, as the line shift is also affected by the surface properties of silicon wafer, such as nucleation site density and contamination/adsorption of other substances. Those factors will also affect Cu outplating. Nevertheless, from these figures it is known that this technique is able to characterize Cu outplating from an HF solution even when the bulk Cu concentration is in ppb range, and the dynamic range is at least three orders of magnitude. It should be noted that equations (6-1), (6-2) and (6-3) are not derived from the mechanism of OCP response, which is described in below.

Mechanism of OCP Response to Bulk Copper Contaminants

For a reactive electrode its OCP is the potential at which the two exchange currents of oxidation and reduction are equal [Ple90]. In our system if there are no copper ions, then silicon is oxidized and protons are reduced, as described by following equations:

$$Si - 4e + 6HF = H_2SiF_6 + 4H^+ \text{ (Oxidation)} \qquad (6\text{-}4)$$

$$2H^+ + 2e = H_2 \text{ (Reduction)} \qquad (6\text{-}5)$$

Therefore the overall reaction on a silicon electrode at OCP is the summation of the above two half reactions:

$$Si + 6HF = H_2SiF_6 + 2H_2 \text{ (Total reaction)} \qquad (6\text{-}6)$$

The partial anodic current density, I, of reaction (6-4) can be described by

$$I_A = n_A F a_{Si} k_{0,A} \exp\left(\frac{\alpha_A n_A F}{RT} E\right) \qquad (6\text{-}7)$$

where n is the number of electrons transferred; F is the Faraday constant; a_{Si} the chemical activity of silicon which can be taken as 1; α_A the anodic transfer coefficient, R the ideal gas constant, T the temperature and E the electrical potential, and k_0 the rate constant for electron transfer at E=0. The subscript A denotes the anodic reaction (6-4). The electrical potential E can be treated as the summation of two components, the equilibrium potential E_e of the half reaction and the overpotential η,

$$E = E_e + \eta \qquad (6\text{-}8)$$

Similarly, for cathodic reaction we can write

$$-I_C = n_C F a_{H^+} k_{0,C} \exp\left(-\frac{\alpha_C n_C F}{RT} E\right) \qquad (6\text{-}9)$$

where a_{H+} is the chemical activity of protons and the subscript C denotes the cathodic reaction (6-5). Since there is no net current at OCP, then

$$I_A(OCP) + I_C(OCP) = 0 \qquad (6\text{-}10)$$

According to Eqs. (6-7), (6-9) and (6-10), we obtain

$$OCP = \frac{RT}{F(\alpha_A n_A + \alpha_C n_C)} \ln\left(\frac{n_c k_{0,C}}{n_a k_{0,A}}\right) + \frac{RT}{F(\alpha_A n_A + \alpha_C n_C)} \ln a_{H^+} \qquad (6\text{-}11)$$

The above relationship suggests that the OCP is a function of reactive specie concentration, exchange currents, and charge transfer characteristics. Furthermore, with the development of the reaction the reactive specie concentrations change, and thus the equilibrium potentials of the two half reactions also change. Ttherefore the original balance of cathodic and anodic currents are not balanced, and the system moves to a new equilibrium by a shift of OCP. Hence OCP usually shifts with time if the electrode is reactive. This shift without the addition of Cu^{2+} is evident in Figures 6-1 and 6-2 at the initial stages.

If copper contaminants are present, then we also need to consider the reduction of Cu^{2+} as well as the reduction of H^+. However, results in Figures 6-1 and 6-2 suggest that the OCP shifts are due to *surface* copper, not bulk copper. Therefore, the effect of copper on OCP shift does not result from copper reduction itself. Figure 6-2 shows that even if a clean HF solution is employed, the OCP shift still remains about the same as that with 100 ppb bulk copper . The mechanism can be understood by taking into consideration of a catalyzed hydrogen evolution (Eq. 6-4) with the presence of copper metal. When copper is outplated onto the silicon surface, the copper particles act as cathodes where protons are reduced to hydrogen. The total cathode current density is the sum of the cathode current densities from copper particles and bare silicon. Therefore the Eq.(6-9) should be modified to

$$-I_C = Fa_{H^+}(1-\theta)k_{0,C}\exp\left(-\frac{\alpha_C F}{RT}E\right) + Fa_{H^+}\theta k_{0,C}^{Cu}\exp\left(-\frac{\alpha_C^{Cu} F}{RT}E\right) \quad (6\text{-}12)$$

where θ is the coverage of copper particles and the superscript Cu denotes the cathode reaction on Cu particles. In above equation, the number of electrons transfered for hydrogen evolution is taken to be 1. Although the copper coverage is small, the reaction rate is much faster than without copper. Figure 6-4 is a SEM micrograph of a silicon surface after 0.5% HF + 100ppm Cu^{2+} 30min dipping under illumination and subsequent stripping of copper particles use stripping solution. The remarkable features on this micrograph are bubble marks as well as pits. In fact, bubbles visible to the eye were formed on the silicon surface when the sample was dipped into HF solution with high concentration of copper contaminants for a long time. While if clean HF solution was used, no bubble was observed. This suggests that the galvanic corrosion of silicon is much faster than HF etching. Hence, we can neglect the contribution of cathodic current from non-covered area in Eq.(6-12). Furthermore, we assume that the surface coverage is linearly proportional to copper surface concentration, i.e.,

$$\theta = k_1[Cu]_{surf} \qquad (6\text{-}13)$$

where k_1 is a constant, then Eq. (6-12) can be simplified to

$$-I_C = F a_{H^+} k_1 [Cu]_{surf} k_{0,C}^{Cu} \exp\left(-\frac{\alpha_C^{Cu} F}{RT} E\right) \qquad (6\text{-}14)$$

Combining Eqs. (6-7), (6-10) and (6-14), we obtain

$$OCP = \frac{RT}{F(n_A\alpha_A + \alpha_C^{Cu})} \ln\left(\frac{k_1 k_{0,C}^{Cu}}{n_A k_{0,A}}\right) + \frac{RT}{F(n_A\alpha_A + \alpha_C^{Cu})}\left(\ln a_{H^+} + \ln[Cu]_{surf}\right) \qquad (6\text{-}15)$$

The correlation between bulk copper concentration and silicon surface concentration after HF dipping has been extensively studied [Ohm93, Rot95, Tor95, Hsu92, Nor97, Tee96, Yon95, Bed93]. However these results suffered from a large within-run and between-run deviation during surface copper measurements. Nevertheless, on a linear scale the plot of surface concentration against bulk concentration at relatively narrow range seemed to be of parabolic type [Tor95, Hsu92, Nor97] and on log-log scale the plot is quite linear [Rot95, Hsu92, Tee96, Yon95, Bed93]. Therefore, the relation between bulk copper concentration and surface copper concentration can be described as

$$[Cu]_{surf} = k_2 [Cu]_{bulk}^{k_3} \qquad (6\text{-}16)$$

thus

$$\ln[Cu]_{surf} = \ln k_2 + k_3 \ln[Cu]_{bulk} \qquad (6\text{-}17)$$

where k_2 and k_3 are constants which characterize the outplating of copper. Combining Eqs. (6-15) and (6-17), we finally obtain Eq. (6-1). Therefore the slope k in Eq. (6-1) is a function of k_3. By measuring k we can characterize copper outplating from HF solution. If additives are present, we need to assume that the additives do not change electron transfer characteristics significantly. Thus the measured change in k can be contributed to the additive effects on copper outplating. The experiment results below indicate that this assumption is reasonable. It should be noted that our data were obtained 15 min after each copper addition. In this duration copper is assumed to be either entirely consumed or remaining in only a very small fraction. Therefore the contribution of cathode current by Cu^{2+} ions can be neglected when considering total cathodic current (Eq. 6-12).

Measurements of Copper Outplating Using This Technique

Figure 6-5 summarizes the OCP change versus time on different p-type wafers from the same batch and Figure 6-6 shows the same parameter obtained from different n-type wafers from the same batch. It shows that n-type wafers have a higher slope than p-type wafers, indicating n-type wafers are more susceptible to Cu outplating. This result agrees with those obtained by other authors [Tee95, Ohm93]. The effects of additives are shown in Figure 6-7, where the curves from 5% H_2O_2, 0.5M HCl, and 0.5M HNO_3 have much smaller slopes, suggesting that all of them are effective in decreasing Cu outplating. These results are also in accordance with previously published results [Chu97, Tee96, Ohm93, Rot95]. In the case of H_2O_2 the slope becomes negative. This may be due to decomposition of H_2O_2 catalyzed by Cu ions.

Summary

A novel technique to characterize copper outplating in situ from HF solutions even when copper bulk concentration is in ppb range is reported. The experiments showed that more severe copper outplating occurs on n-type wafers than on p-type wafers, and that H_2O_2, HCl, and HNO_3 are all effective in alleviating Cu outplating. These results are in agreement with the copper contamination results reported by other authors. The mechanism of OCP shift is explained in detail by using mixed potential theory and take copper catalyzed hydrogen evolution into consideration. This technique has been employed successfully on identifying novel additives to minimize Cu outplating during HF cleaning.

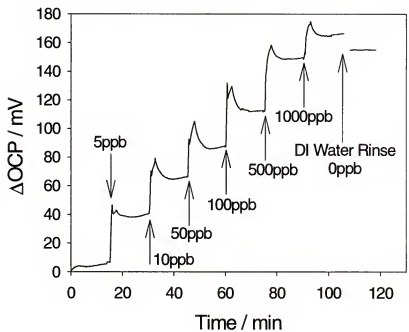

Figure 6-1. Plot of OCP change with Cu addition. It shows that OCP changes with the addition of copper ions. Fresh 0.5% HF is used at final stage and the OCP does not change much, suggesting the OCP change is irrelevant to the bulk copper contaminant.

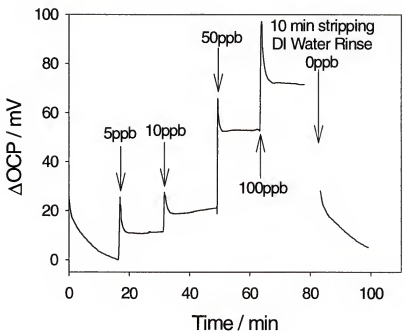

Figure 6-2. Plot of OCP change with Cu addition. At final stage surface Cu is stripped and fresh 0.5% HF is used, and the OCP goes back to original value, suggesting that OCP change is caused by surface copper contamination.

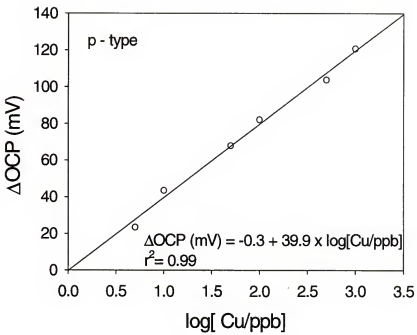

Figure 6-3. OCP change versus logarithm of Cu bulk concentration. It gives a straight line.

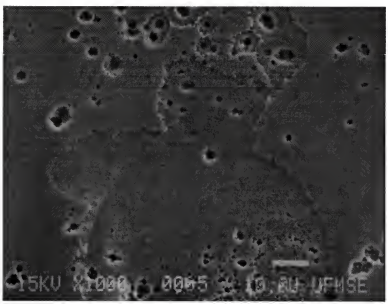

Figure 6-4. SEM micrograph of a copper contaminated silicon surface. It was dipped into 0.5%HF + 100ppm Cu^{2+} for 30 min under illumination, then copper particles were stripped by stripping solution. Note the clear bubble marks which is likely to be due to hydrogen evolution. No bubbles were observed if no copper contaminants or contamination level in HF solution is low.

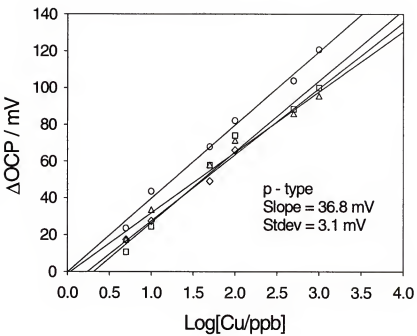

Figure 6-5. P-type wafer OCP change versus logarithm of Cu bulk concentration (different wafers from same batch). It shows that the slope is repeatable but the absolute OCP values are not repeatable.

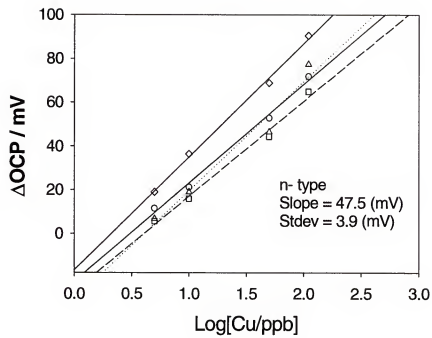

Figure 6-6. N-type wafer OCP change versus logarithm of Cu bulk concentration (different wafers from same batch). It shows that the slope is repeatable but the absolute OCP values are not repeatable.

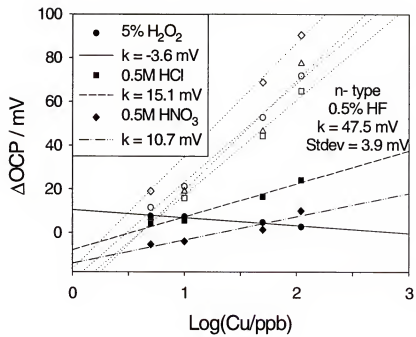

Figure 6-7. Effects of H_2O_2, HCl, and HNO_3 in decreasing Cu outplating (5% H_2O_2, 0.5M HCl and 0.5M HNO_3 in 0.5% HF, respectively. Plots of 0.5% HF only are also graphed). Additives clearly decrease the slopes.

CHAPTER 7
SURFACTANT EFFECTS ON COPPER OUTPLATING ONTO SILICON SURFACES FROM HF SOLUTION

Introduction

The studies in Chapters 3 and 4 suggest that in order to prevent particle redeposition in HF-last cleaning, surfactants will be used to modify electric charges on both silicon and particle surfaces so that a repulsive electrostatic force overcomes the attractive dispersion force between the two surfaces. Surfactants are also reported to be effective in decreasing copper outplating from HF solutions onto silicon surfaces. Ohmi et al. have shown that copper deposition on silicon wafers from BHF63 solution was decreased if a certain type of hydrocarbon or fluorocarbon surfactant was used [Ohm92] . Obeng demonstrated that the addition of anionic perfluorocarbon surfactants to a 5% HF solution reduced the silicon surface copper concentration by four fold [Obe94]. Jeon et al. reported a tenfold decrease in copper outplating by using the surfactant OHS, which is an alkylphenol polyglycidol nonionic surfactant [Jeo96]. However, Torcheux et al. reported that FC-98, a perfluoroalkylcyclohexylsulfonate clearly increased silicon surface copper contamination [Tor95].

It has been postulated that the reasons for surfactants to be effective in decreasing copper outplating are (1) surfactant films adsorb on and passivate substrate surfaces, and

(2) the micelles immobilize cupric ions, which reduces the efficiency of electron transfer kinetics and free cupric ion concentration thus driving force for copper outplating [Obe94]. Nevertheless, it is not yet clear just what the role is of surfactants in increasing copper contamination.

In Chapter 6 , a new method to characterize copper outplating in situ from HF solutions was studied. It measures the open circuit potential(OCP) change of a silicon electrode immersed in HF solutions contaminated with various amounts of copper. The plot of OCP change vs. the logarithm of bulk copper concentration is a straight line, and the slope of the line best describes the additive effects on copper outplating. An additive which reduces copper outplating will give a smaller slope than that when no additive is used, and visa versa. Figure 7-1 shows the results of 0.5% HF and 0.5% HF + 0.5M HCl solutions contaminated with copper. In Figure 7-1a the plots of OCP change vs. log[Cu] show that the slope is decreased when HCl is present. Figure 7-1b is the TXRF results of surface copper concentration after a 10min dip into above-mentioned solutions under illumination. It shows that 0.5M HCl can reduce surface copper contamination up to two orders of magnitude. This is in agreement with other authors [Tee96].

In this study, the effects and mechanism of surfactants on copper outplating are discussed. Special attention is payed to the additives which were shown effective in decreasing particulate contamination. It was found that certain cationic surfactants can significantly decrease copper outplating, and that there is a potential risk in terms of increased copper and organic contamination using anionic surfactants in HF-last cleaning.

Experimental

A cationic surfactant and an anionic surfactant were selected to study their effects on copper outplating. The cationic surfactant we used is an alkyltetramethylammonium bromide, and the anionic surfactant is a sodium alkylsulfonate. They have similar chain structures and molecular weights. Results in Chapter 3 showed that both of them are effective in prevention of particle redeposition onto silicon wafer surface from HF solution.

The OCP measurement set up was the same as in Chapter 6. A 2 inch (100) n-type silicon wafer with 1-10 ohm-cm resistivity (Silicon Quest International) was subjected to SC-1 cleaning, dilute HF cleaning and DI water rinse to remove particles and chemical oxide before being mounted on a custom-made TEFLON electrochemical cell. Only the polished side of a wafer was contacted with solution, and the back side was contacted to a stainless steel base that had a stainless steel connection to the outside. The ohmic contact was made by coating a thin film of eutectic Ga-In alloy (Alfa Aesar) between the back side of the wafer and the metal base. An HF resistant Ag/AgCl reference electrode (Fisher Scientific) was positioned near the wafer. 50 ml 0.5 wt. % solutions with and without additives were used in the cell. A 25 W Leica incandescent lamp was employed and the light was shone directly onto the wafer. Copper was added by using 1000 ppm atomic absorption spectroscopy (AAS) standard (Fisher Scientific). Each time when Cu was added, the solution was gently shaken until it appeared well mixed. Then OCP change with time was recorded using a CHI 660 Electrochemical work station. After 15 minutes

more Cu was added to the solution and the above processes were repeated. To regenerate silicon wafer electrode after a complete copper outplating experiment, a 5ml 5% HF + 5% HNO_3 + 5% H_2O_2 (wt.) was employed to remove surface Cu.

Wafers were also dipped into 0.5% HF bath with the intentional copper contamination and with/without surfactant for 10 min under illumination. The bulk copper concentrations are 100ppb and 10 ppm. For the wafers dipped into 100 ppb copper contaminated bath, the surface contaminations were examined by the total reflectance X-ray fluorescence (TXRF) and the time-of-flight secondary ion mass spectroscopy (TOF-SIMS). For the wafers dipped in 10 ppm copper contaminated bath, the surface morphology was studied with the scanning electron microscope. For all the experiments, the surfactant concentrations were 1% (wt.). Particle size analyses were carried out in a 1% anionic surfactant + 500ppm copper contaminant water solution by the dynamic light scattering method. Transmission electron spectroscopy(TEM) analyses on particles from a 1% anionic surfactant + 500ppm copper contaminant solution were also conducted. The TEM sample was prepared by dipping a copper grid covered with an amorphous carbon thin film (Ted Pella) into the solution to capture particles.

Results and Discussion

The plots of OCP change with bulk copper concentration with and without the cationic surfactant are shown in Figure 7-2a. At low copper contamination levels (<50ppb), the slope is remarkably smaller when the surfactant is present; at high copper contamination levels (>50ppb), the slopes with and without the surfactant are about the

same. It suggests that the cationic surfactant can reduce copper outplating effectively at low copper contamination levels. The TXRF surface copper concentration results in Figure 7-2b suggest that the surfactant indeed decreases copper outplating. It should be noted that at a 100ppb bulk contamination level, as in TXRF experiments, the surfactant starts losing its capability to reduce copper outplating as suggested by Figure 7-2a. Nevertheless, the overall surface copper contamination is still lowered. It could be understood by drawing a regression line passing only the first four points, i.e., the points corresponding to the bulk concentration up to 100ppb. The slope of this line is lower than that of the control sample which is 0.5% HF only, without surfactant. The change of slopes in Figure 7-2a further indicates the change of copper outplating mechanisms from one to another. Unfortunately they are not well understood. In Chapter 5 we have shown that copper will preferentially deposit on damaged surface due to defect-enhanced nucleation. The effect of the cationic surfactant on the preferential deposition is discussed here. Figure 7-3 is a SEM micrograph of a scratched silicon surface after copper deposition with the presence of the cationic surfactant. No copper particles are observed at all, as suggested by the characteristic X-ray mapping in Figure 5-7b and c. Comparing Figure 7-3 with Figure 5-7, one will conclude that the surfactant is effective in decreasing copper deposition. Furthermore, The higher magnification micrographs in Figure 7-4 show that even the detailed scratching feature can survive 10 ppm copper contamination. It would be more evident if one compares Figure 7-4 with Figure 5-8. Therefore, it can be concluded that the effect of the surfactant is due to its ability to protect surface defects from copper preferential nucleation.

The effect of the selected anionic surfactant on copper outplating is shown in Figure 7-5. The OCP change vs. log[Cu] plots in Figure 7-5a indicates that the surfactant is also effective in decreasing copper outplating, since it gives significantly smaller slopes. However TXRF results in Figure 7-5b only show about two fold decreases in copper outplating, invalidating our prediction. In order to investigate the copper outplating mechanism with the presence of this sulfonate surfactant, surface copper change with dipping time was measured. The bulk copper concentration was still 100ppb. The results are given in Figure 7-6. The most important observation in this experiment is that the surface copper concentrations do not change with dipping time when the surfactant is present. They then imply that the surface copper may not be due to redox reaction, but some kind of adsorption type of reaction. Therefore, we propose the following reaction:

$$2R-SO_3^- + Cu^{2+} \Leftrightarrow (R-SO_3)_2 Cu \ (aq.) \Leftrightarrow (R-SO_3)_2 Cu \downarrow \qquad (7\text{-}1)$$

Some free cupric ions associate with surfactant molecules on the sulfonate group, and the charges are neutralized. Thus surfactants lose their hydrophilicity, they then have a greater tendency to adsorb onto hydrophobic bare silicon surfaces. Furthermore, the final rinse by DI water cannot remove adsorbed surfactant-copper molecules totally from silicon surfaces. Therefore, copper surface contamination is high. It should be noted that the OCP method only responds to metallic copper. That is why the OCP method suggests low copper contamination, while TXRF results show high copper contamination.

In order to support our hypothesis on copper-sulfonate association, we increased the copper concentration to 500ppm to see if precipitation can be formed or not. As long

as concentrated AAS standard copper solution was added into 1 wt. % surfactant water solution, white precipitation was indeed observed. The cloudy solution was subject to dynamic light scattering particle size analysis. The results are graphed in Figure 7-7. They show that after the addition of cupric ions to bulk concentration to be 500ppm, the measured particle distribution clearly shifted to larger sizes compared with the case without copper contaminants. Those particles were subjected to TEM analysis. The bright field(BF) transmission electron micrograph in Figure 7-8a showed that the precipitation formed an oily film with localized globular droplets on the amorphous thin carbon film of the copper grid. Selected area diffraction patterns (SADP's) were taken from both the oily film and the droplets. The SAD pattern in Figure 7-8b indicates that they are amorphous.

If copper is indeed precipitated onto the silicon surfaces with surfactants, then the silicon surfaces should have high sulphur contamination. Unfortunately, TXRF did not detect a sulphur signal at this contamination level. In order to prove our hypothesis, another disulfonate surfactant was studied vis-a-vis its effect on copper outplating by OCP monitoring and TOF-SIMS surface analysis. Since this surfactant has two sulfonate groups on one molecule, it is expected to be more feasible to complex it with cupric ions. Moreover, it may give a higher sulphur signal if the adsorption amount is about the same as the previous monosulfonate surfactant. The OCP change with bulk copper concentration plots in Figure 7-9a suggest it is effective in reducing copper contamination. However, the TOF-SIMS results in Figure 7-9b reveal increased copper contamination. This time the sulphur signal was clearly observed to be higher than the control sample. These results are in agreement with our hypothesis.

Generally speaking, in HF-last cleaning only noble metals are a concern for metal contamination, because the mechanism for metal outplating from HF solution is via redox reaction. However, if an anionic surfactant is used, the precipitation mechanism should also be considered. In this mechanism, not only cupric ions but also other metal ions are able to form precipitates with the surfactant and adsorb onto the silicon wafer surfaces. Therefore, we also studied the sulfonate surfactant interactions with Fe^{3+} and Ni^{2+}. Figure 7-10a and 7-10b are the dynamic light scattering results on 1% surfactant + 500ppm Fe^{3+} and Ni^{2+}, respectively. It turned out that Fe^{3+} does not form a precipitate with the surfactant, while Ni^{2+} indeed forms a precipitate with this surfactant. Therefore, it is also possible to increase nickel contamination if this surfactant is used in HF-last cleaning.

According to the results presented above and those published previously, the roles that the surfactant plays in copper contamination during HF-last cleaning can be summarized as follows:

(1) Surfactants alter silicon surface charges, causing localized depletion or accumulation of copper ions.

A positively charged silicon surface will repel cupric ions, while negatively a charged silicon surface will attract cupric ions. To a first approximation, let us neglect copper-surfactant interaction, then the spatial distribution of cupric ion concentration near the charged silicon surface can be described by Boltzmann distribution:

$$c(x) = c_b \exp\left(-\frac{2e\Phi}{kT}\right) \qquad (7\text{-}2)$$

where c is the concentration of cupric ions at distance x from the silicon surface, c_b is the

concentration of cupric ions far from the surface, e is unit charge, Φ is the electric potential, k is the Boltzmann constant, and T is the absolute temperature. This relation states that the electrostatic force exerted on a cupric ion is balanced by its thermal motion. In Table 7-1 the zeta-potentials of a silicon surface in different solutions are listed.

Table 7-1. Zeta-potentials of silicon surfaces in different solutions

Solution	Zeta-potential
0.5% HF	6.0 ± 2.0
0.5% HF + 1% cationic surfactant	58.4 ± 2.8
0.5% HF + 1% anionic surfactant	-38.7 ± 2.3

The Potential distribution near a charged surface in a symmetrical electrolyte solution is [Gou10]

$$\Phi = \frac{2kT}{ze}\ln\left(\frac{1+\exp(-\kappa x)\tanh(ze\Phi_0/4kT)}{1-\exp(-\kappa x)\tanh(ze\Phi_0/4kT)}\right) \qquad (7\text{-}3a)$$

where κ is called inverse Debye length which has a m^{-1} unit, and

$$\kappa = \sqrt{\frac{2z^2e^2n_0}{\varepsilon kT}} \qquad (7\text{-}3b)$$

and Φ_0 is surface potential, n_0 is bulk concentration of the electrolyte, z is the absolute charge of electrolyte ions, and ϵ is permittivity of the solution. Based on Eqs. 7-2 and 7-3,

and data in Table 7-1 we can access the cupric ion concentration distributions. The bulk copper concentration is 100ppb. The electrolyte concentration is 5×10^{-2} M assuming surfactant molecules are totally dissociated, then the Debye length is about 1.4 nm. The cupric ion contribution on κ is neglected. The results are plotted in Figure 7-11. It shows the cationic surfactant modified surface depletes cupric ions significantly while anionic surfactant modified surface attracts cupric ions. The cupric ion concentration at slip planes very close to the silicon surface where the zeta-potential is measured is about two orders of magnitude lower than that in the bulk when the cationic surfactant is present, and about twenty fold higher when the anionic surfactant is presented. It should be noted that in the anionic surfactant case, we clearly showed that there is a strong interaction between the cupric ions and the anionic surfactant ions, therefore the Boltzmann distribution is not appropriate to describe cupric ion distribution, at least when anionic surfactant is present.

(2) Surfactants alter the mass transport kinetics.

It has been shown that copper outplating is a diffusion-controlled process, and the surface copper concentration linearly correlates to square root of dipping time [Tor95, Chy96]. The diffusivity values of cupric ions were also reported according to the surface copper concentration / dipping time relation. However, the previous work only considered cupric ion diffusion under a concentration gradient. The effect of an electric potential gradient was neglected. Conversely, the above discussion on cupric ion concentration distribution neglected surface reaction between cupric ions and silicon. If the surface reaction rate is very fast, then, according to thermodynamic data, the cupric ion

concentration at the silicon surface is essentially zero [Tor95]. Therefore, the correct description for cupric ion transport kinetics and concentration distribution should be based on the following equation [Sze81]

$$\frac{\partial c}{\partial t} = D\frac{\partial^2 c}{\partial x^2} + \frac{zeD}{kT}\frac{\partial c}{\partial x}\frac{\partial \Phi}{\partial x} + \frac{zeD}{kT}\frac{\partial^2 \Phi}{\partial x^2} \qquad (7\text{-}4)$$

where c is the concentration and D is the chemical diffusivity. Although the solution to the above equation is beyond the scope of this paper, we can conclude that as long as the diffusivity of cupric ions changes, the copper outplating kinetics change, assuming surface reaction is very fast. The presence of a surfactant in the solution changes the viscosity of the solution, and thus changes the diffusivity of the cupric ions. More importantly, the surfactant molecules form a thin layer on the silicon surface; cupric ions have to pass this film to react with silicon. The transport kinetics of cupric ions through this adsorbed surfactant thin film are expected to be different greatly from the transport in the bulk.

(3) Surfactants interact with cupric ions.

Surfactants, especially anionic surfactants, may have a strong interaction with cupric ions. This has two effects on copper outplating. One is that surfactants decrease the free cupric ion concentration, resulting in a decreased tendency for copper outplating. The other is that the surfactant/cupric ion complex may be adsorbed onto silicon surfaces. If this complex is not or cannot be totally rinsed off by the following DI water rinse, then copper contamination will increase.

(4) Surfactants alter silicon surface properties.

The initial nucleation stage plays a vital role in copper outplating. It has been shown in Chapter 5 that for a silicon surface with both an intact region and an artificially modified region, copper was preferentially deposited on the modified region. The reason was believed to be due to preferential nucleation because of higher dangling bond density. If surfactants were also preferentially adsorbed onto defect sites where nucleation could take place, then the copper outplating is expected to decrease. Moreover, adsorbed ionic surfactants change the silicon surface charge, causing a change of electron/hole distribution near the silicon surface on silicon side. The depletion/accumulation of electrons/holes in turn affects electron/hole transfer kinetics between silicon and cupric ions [Nor97], thus, the copper outplating is influenced.

The roles of surfactants in copper outplating are not isolated; they most probably are connected together. Hence, we observed different effect of surfactants on copper outplating. The contamination mechanism via adsorption suggests that if surfactants are used in HF-last cleaning, which is proposed so as to minimize particle redeposition, it is critical to study its effect on metal contamination. Not only should copper be studied, but also other metals which have low reducing potentials.

Summary

Surfactant effects on copper outplating onto silicon surfaces during DHF cleaning were studied. It was found that certain cationic surfactants are effective in reducing copper outplating onto silicon surfaces during DHF cleaning. Anionic surfactants may

increase the metal outplating not only of copper but also other metals (such as nickel) by forming complexes with metal ions and subsequent adsorption of these complexes onto silicon surfaces. Combining open circuit potential monitoring and surface metal analysis, one can differentiate different mechanisms of copper outplating. The roles of surfactant on copper outplating are discussed in detail in the Chapter.

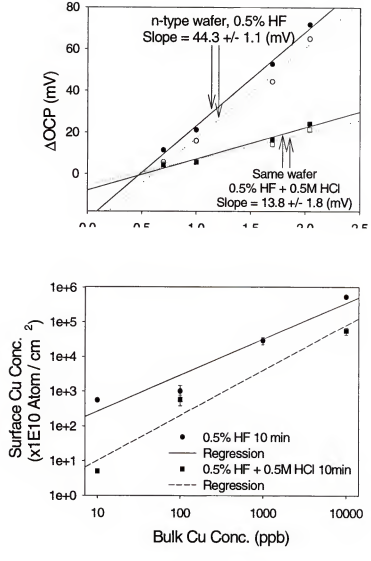

Figure 7-1. The effect of HCl on copper outplating from DHF solution onto silicon surfaces. (a, top) The plots of OCP change vs. Log[Cu]. Addition of HCl remarkably decreases the slope. (b, bottom) TXRF results of surface copper concentration after 10min dipping into 100ppb copper contaminated DHF solution.

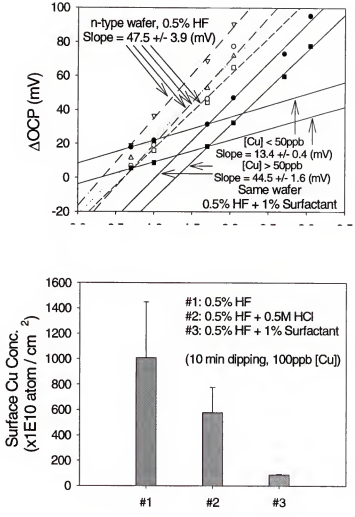

Figure 7-2. The effect of the selected cationic surfactant on copper outplating from DHF solution onto silicon surfaces. (a, top) The plots of OCP change vs. Log[Cu]. The cationic surfactant decreases the slope. (b, bottom) TXRF results of surface copper concentration after 10min dipping into 100ppb copper contaminated DHF solution.

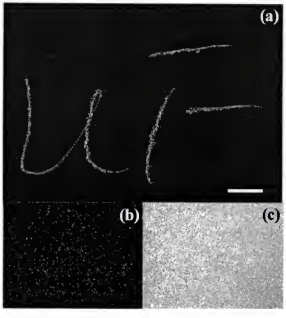

Figure 7-3. Micrographs of a scratched silicon surface after copper contamination with the presence of a cationic surfactant. The scratched lines are the letters "UF", and copper preferential deposition is not observed. (a) SEM image, (b) Cu Kα X-ray image, and (c) Si Kα X-ray image. The scale bar is 200 micron.

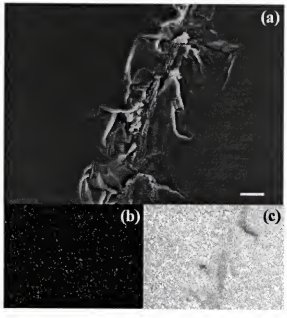

Figure 7-4. Magnified micrographs of a scratched silicon surface in Figure 7-3. After adding the surfactant the scratched areas are free of copper contamination and remain intact. (a) SEM image, (b) Cu Kα X-ray image, and (c) Si Kα X-ray image. The scale bar is 10 micron.

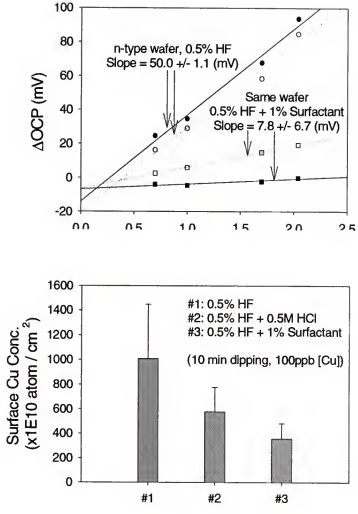

Figure 7-5. The effect of the selected anionic surfactant on copper outplating from DHF solution onto silicon surfaces. (a, top) The plots of OCP change vs. Log[Cu].The anionic surfactant also decreases the slope significantly. (b, bottom) TXRF results of surface copper concentration after 10min dipping into 100ppb copper contaminated DHF solution. Note that the surfactant only decreases copper outplating by about two fold.

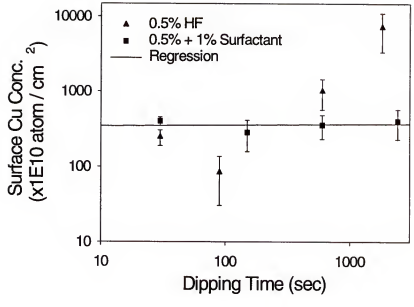

Figure7- 6. TXRF results of surface copper concentrations as a function of dipping time. The copper contamination with the presence of the anionic surfactant does not change with time. The solution is 0.5% HF + 100ppb copper with/without surfactant.

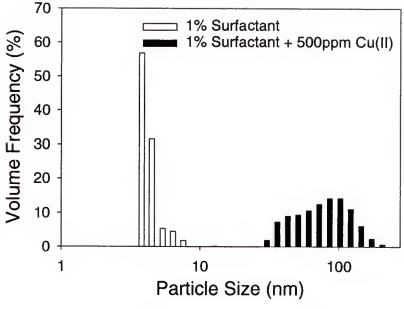

Figure 7-7. Particle size distributions in 0.5% HF + 500ppm copper with/without the anionic surfactant. Note that the surfactant clearly forms precipitates with cupric ions.

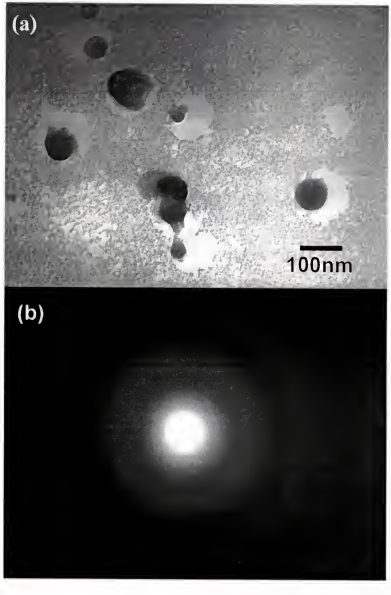

Figure 7-8. TEM results of surfactant-copper precipitations. (a) BF image of the particles. (b) SAD pattern of the particles. They are amorphous in nature.

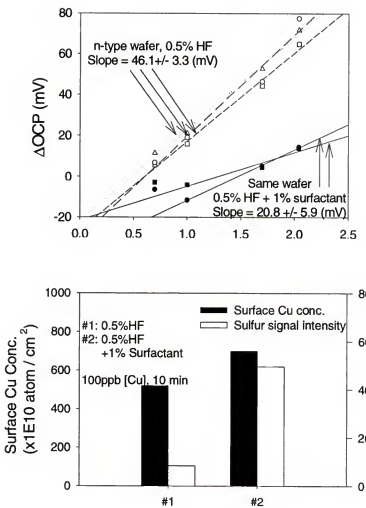

Figure 7-9. The Effect of an disulfonate surfactant on copper outplating. (a, top) Plots of OCP change vs. Log[Cu]. It also gives a smaller slope. (b, bottom) TOF-SIMS surface analysis results. Note that both copper contamination and sulfur contamination are higher.

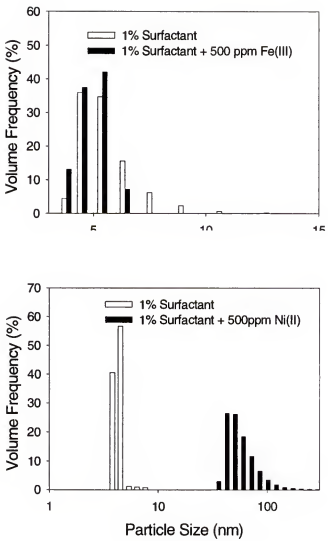

Figure 7-10. Particle size distributions in 0.5% HF + 500ppm metal ions with/without surfactant. (a, top) Fe(III) ions. (b, bottom) Ni(II) ions. It clearly shows that Ni(II) also forms precipitation with this surfactant.

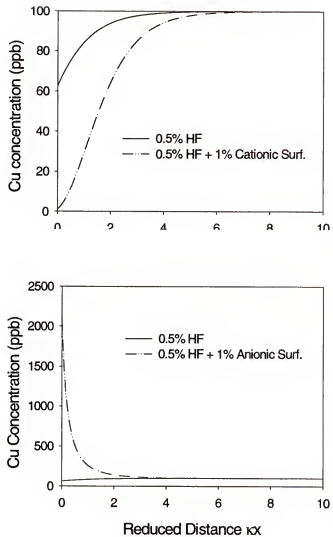

Figure 7-11. Cupric ion spatial distributions near silicon surfaces in different solutions. (a) The cationic surfactant effect. (b) The anionic surfactant effect. They show that cationic surfactant modified silicon surface repels cupric ions while anionic surfactant modified silicon surface attracts cupric ions. It should be noted that during the calculation the surface reaction and electrolyte interactions are neglected. Copper bulk concentration is 100ppb.

CHAPTER 8
GENERAL SOLUTION FOR POISSON-BOLTZMANN EQUATION IN SEMI-INFINITE PLANAR SYMMETRY

Introduction

During our discussions on particulate and metal contamination on silicon wafer surfaces in HF solutions, we have repeatedly applied the Derjaguin-Landau-Verway-Overbeek (DLVO) theory which is about colloidal surface interactions. Although this theory can be successfully applied to our silicon surface-contaminant-HF solution system, my attention has extended to some cases in which the DLVO theory is not readily applicable because of mathematical difficulty, or the DLVO theory fails. In this chapter, we will discuss the potential distribution in a planar electrical double layer with the presence of a highly asymmetrical electrolyte. The potential distributions in electrical double layers are the basis of the electrostatic interaction between two surfaces. There is no a simple mathematical equation to describe the planar electrical double layers with the presence of an electrolyte previously. We will discuss the failure of the DLVO theory in confined colloidal systems in the next chapter.

The theory of planar electrical double layers is an old topic originated from Gouy [Gou09, Gou10]. It is the foundation for the calculation of electrostatic interactions of colloid particles [Ver48, Der87]. The governing equation of a diffuse layer is the well-

known Poisson-Boltzmann(PB) equation, which states that electrolyte ions are attracted/repelled by a charged surface in addition to their thermal motion, and that the distributions of ions then implicitly define the potential distribution near the charged surface,

$$\nabla^2\Phi = -\sum \frac{z_i e n_{i0}}{\varepsilon} \exp\left(-\frac{z_i e \Phi}{kT}\right) \qquad (8\text{-}1)$$

where Φ is the potential, ϵ is the static permittivity of solution, i is the ions of kind i, z_i is its charge including sign, n_{i0} is its concentration at bulk where Φ is chosen to be zero, e is the unit charge, k is the Boltzmann constant and T is the absolute temperature. For a semi-infinite plane the problem is simplified to a one-dimensional case with the following boundary conditions:

$$x = 0, \quad \Phi = \Phi_0 \qquad (8\text{-}2)$$

$$x \to \infty, \quad \Phi = 0 \qquad (8\text{-}3)$$

where Φ_0 is surface potential and the surface is located at x = 0. Note here the Stern layer is neglected for the purpose of this paper.

Only three limiting cases have been found to have exact solutions in Eq.(8-1) in semi-infinite planar symmetry. One is the Debye-Huckel approximation for small surface potentials. When $|z_i e\Phi|/kT \ll 1$, the right-hand-side Eq. (8-1) can be Taylor expanded with only the linear terms retained, and the solution is then

$$\Phi(x) = \Phi_0 \exp(-\kappa x) \qquad (8\text{-}4)$$

where κ is known as inverse Debye length. It has units of m^{-1} and is given by

$$\kappa = \sqrt{\sum \frac{z_i^2 e^2 n_{i0}}{\varepsilon kT}} \qquad (8\text{-}5)$$

This simple solution contains all qualitative information about a diffuse layer. However, since at room temperature kT is about 25mV, this linearization renders large deviation at potentials higher than 25mV. When only the symmetrical z-z electrolyte is present, the exact solution for PB equation is available [Gou09, Gou10, Cha13]

$$\Phi(x) = \frac{2kT}{ze} \ln\left(\frac{1+\gamma \exp(-\kappa x)}{1-\gamma \exp(-\kappa x)}\right) \qquad (8\text{-}6)$$

where

$$\gamma = \tanh\left(\frac{ze\Phi_0}{4kT}\right) \qquad (8\text{-}7)$$

and z is the charge of a cation.

When the electrolyte is of z-2z or 2z-z type, the exact solutions are also available, but they are mathematically cumbersome, and two functions are required for z-2z and 2z-z electrolytes, respectively [Gou10, Der87, Gra53, Lev90]. For example, for 2-1 electrolyte such as $CaCl_2$, the solution is

$$\Phi(x) = \frac{kT}{e} \ln\left(1 + \frac{6p}{(p-1)^2}\right) \qquad (8\text{-}8)$$

where

$$p = \frac{\sqrt{1+2\exp\left(\frac{e\Phi_0}{kT}\right)} + \sqrt{3}}{\sqrt{1+2\exp\left(\frac{e\Phi_0}{kT}\right)} - \sqrt{3}} \exp(\kappa x) \qquad (8\text{-}9)$$

Apparently, the complexity associated with these expressions hinder their application. Therefore people tend to use a symmetrical approximation when asymmetrical electrolytes are encountered [Ros88]. In doing so, the absolute value of counter ion charge should be always chosen as z in Eq.(8-6), because the counter ion term in the right-hand side of the PB equation is dominant in the high potential region. However, the symmetrical approximation will lead to large errors in some cases, especially when the potential is high and the electrolyte is highly asymmetrical. This will be discussed later in this Chapter.

Despite the argument on its validity at high potentials [Ons33, Kir34], the PB equation provides a useful first approximation for the electrical potential distribution [Lev51]. For multivalent ions, the non-linear PB equation is expected to be more accurate than the linear equation [Sha90]. Furthermore, the calculation of electrical interaction in classical DLVO theory starts with a calculation of the potential distribution near charged plates [Ver48]. Therefore it is still meaningful to obtain a simple and accurate solution for non-linear PB equation in semi-infinite planar symmetry. In this paper we reported a simple and general solution for all unmixed electrolyte cases in this symmetry. It is exact for symmetrical and z-2z/2z-z electrolytes, and is a very good approximation for z-3z/3z-z or 2z-3z/3z-2z electrolytes. The accuracy of the approximation is evaluated by comparing with numerical solutions obtained by the Galerkin weighted residual finite element method. The error is within 1%. The numerical method itself can be easily adapted to any case in semi-infinite planar symmetry or two interacting planar double layers, no matter if the electrolyte is mixed or not.

Methods

The method we used to solve the PB equation analytically is the same as many authors used before [Rus89, Isr92, Hun93]. Multiply both sides of Eq.(8-1) by 2dΦ/dx then integrate the equation with the boundary condition

$$\Phi = 0, \quad \frac{d\Phi}{dx} = 0 \qquad (8\text{-}10)$$

we obtain

$$\frac{d\Phi}{dx} = \mp\sqrt{\sum_i \frac{2kTn_{i0}}{\varepsilon}\left[\exp\left(-\frac{z_i e\Phi}{kT}\right)-1\right]} \qquad (8\text{-}11)$$

In the above equation, the negative sign is used when the surface potential is positive, and visa versa. Integrate Eq.(8-11) again, to obtain

$$\int \frac{d\Phi}{\sqrt{\sum_i \frac{2kTn_{i0}}{\varepsilon}\left[\exp\left(-\frac{z_i e\Phi}{kT}\right)-1\right]}} = x + C \qquad (8\text{-}12)$$

where C is the integral constant which can be evaluated by using Eq.(8-2). The left-hand-side of Eq.(8-12) cannot be generally integrated. Nevertheless, when the electrolyte is unmixed we can obtain analytical solutions for two special cases; namely the z-z electrolyte case and the z-2z/2z-z case.

(1)The symmetrical z-z electrolyte case

It turns out that the two results pertaining to positive or negative surface charges are identical. The result is

$$\Phi(x) = -\frac{2kT}{ze}\ln\left(\tanh\left(\frac{\kappa}{2}x + \beta\right)\right) \qquad (8\text{-}13)$$

where

$$\beta = \tanh^{-1}\left(\exp\left(-\frac{ze\Phi_0}{2kT}\right)\right) \qquad (8\text{-}14)$$

and κ is defined by Eq.8-5. The value of z is equal to the charge of electrolyte ions (cation or anion) including a sign.

(2)The asymmetrical z-2z or 2z-z electrolyte case.

The two results of positive and negative potentials can be included into one form

$$\Phi(x) = -\frac{kT}{ze}\ln\left(\frac{3}{2}\tanh\left(\frac{\kappa}{2}x + \beta\right)^2 - \frac{1}{2}\right) \qquad (8\text{-}15)$$

where

$$\beta = \tanh^{-1}\left(\sqrt{\frac{1 + 2\exp\left(-\frac{ze\Phi_0}{kT}\right)}{3}}\right) \qquad (8\text{-}16)$$

and z is the charge (sign included) of the ion which contains less charge. For example, if the electrolyte is $CaCl_2$, then the z should be -1; if the electrolyte is Na_2SO_4, z should be +1, no matter what sign the surface potential is. Eqs.(8-15) and (8-16) contain all the possible cases with z-2z/2z-z electrolytes.

One can unify Eqs. (8-13) and (8-15) into one equation

$$Y(x) = -\frac{1}{z}\ln\left[\alpha\tanh\left(\frac{\kappa}{2}x + \beta\right)^2 - \alpha + 1\right] \qquad (8\text{-}17)$$

where the unitless quantity Y is known as the reduced potential

$$Y \equiv \frac{e\Phi}{kT} \qquad (8\text{-}18)$$

and

$$\beta = \tanh^{-1}\left(\sqrt{\frac{y+\alpha-1}{\alpha}}\right) \qquad (8\text{-}19)$$

with

$$y \equiv \exp\left(-\frac{ze\Phi_0}{kT}\right) \qquad (8\text{-}20)$$

The constant α is evaluated by combining Eqs.(8-1), (8-17), (8-19) and (8-20) at x = 0

$$\alpha = \frac{1}{2}\frac{y^3 - 3y + 2}{1 - y + \frac{z}{z_c - z_a}y^2\left(y^{\frac{z_c}{z}} - y^{\frac{z_a}{z}}\right)} \qquad (8\text{-}21)$$

where z_c is the valence of cation and z_a is the valence of anion including the sign. It turns out that the general solution (8-17) is a very good approximation for z-3z/3z-z and 2z-3z/3z-2z cases, if the value z in the general solution is chosen to be the valence of the counter ions (including the sign).

In order to evaluate the accuracy of the general solution in the z-3z/3z-z and 2z-3z/3z-2z cases, the nonlinear PB was solved numerically by the Galerkin weighted residual finite element method [Red93]. Since the geometry goes to infinity, it is easier to transform x to a finite region. Let

$$X = \exp(-\kappa x) \quad 0 \le X \le 1 \qquad (8\text{-}22)$$

then the nonlinear PB equation (Eq. (8-1)) is transformed to

$$X^2 \frac{dY}{dX} + X \frac{dY}{dX} = A \exp(-z_c Y) + B \exp(-z_a Y) \qquad (8\text{-}23)$$

when the x-direction only with unmixed electrolyte case is considered. The constants A and B are

$$A = \frac{1}{z_a - z_c} \qquad (8\text{-}24)$$

$$B = \frac{1}{z_c - z_a} \qquad (8\text{-}25)$$

Note that Eq. (8-23) is a unitless equation in which X and Y are defined by Eq. (8-22) and Eq. (8-18), respectively.

The formulation of Galerkin weighted residual finite element method is as follows. The weighted residual, R_i, of Eq. (8-23) is written as

$$R_i = \int_0^1 \left(X^2 \frac{d^2 Y}{dX^2} + X \frac{dY}{dX} - f(Y) \right) \phi_i dX = 0 \qquad (8\text{-}26)$$

where f(Y) is the right-hand-side of Eq. (8-23) and ϕ_i is the i-th weighting function. The weak form of the equation is obtained by performing an integration by parts

$$-\int_0^1 \frac{dY}{dX} \left(X^2 \frac{d\phi_i}{dX} + X\phi_i \right) dX - \int_0^1 f(Y)\phi_i dX = 0 \qquad (8\text{-}27)$$

The boundary terms are omitted since only Dirichlet-type (essential) boundary conditions are considered. The solution of Y is approximated as

$$Y \approx \sum_j \phi_j Y_j \qquad (8\text{-}28)$$

where Y_j is the value of Y at the j-th node, and ϕ_j is the j-th shape function. The Galerkin method uses shape functions as weighting functions. Thus the functions ϕ in Eq. (8-26) and Eq. (8-28) are the same. Two-node linear elements were used in our formulation. Insert Eq. (8-28) into Eq. (8-27), we obtain

$$K_{ij}Y_j = F_i \qquad (8\text{-}29)$$

or in matrix form

$$[K]\{Y\} = \{F\} \qquad (8\text{-}30)$$

where

$$K_{ij} = -\int_0^1 \left(X^2 \frac{d\phi_i}{dX} + X\phi_i \right) \frac{d\phi_j}{dX} dX \qquad (8\text{-}31)$$

and

$$F_i = \int_0^1 f(Y)\phi_i dX \qquad (8\text{-}32)$$

Since the {F} vector contains the unknown Y at each node, we have to use an iterative method to solve Eq.(8-30). It turns out that convergency cannot be reached with the direct iteration method (Picard method), therefore the Newton-Raphson method was employed. First we calculated the variation of the solution $\{\Delta Y\}$ by

$$\{\Delta Y^{r+1}\} = -[K_T]^{-1}\left([K]\{Y^r\} - \{F(Y^r)\}\right) \qquad (8\text{-}33)$$

where r is the iteration level and $[K_T]$ is called the tangent matrix. It is given by

$$K_{T_{ij}} = K_{ij} - \frac{\partial F_i}{\partial Y_j} \qquad (8\text{-}34)$$

Then we updated the solution

$$\{Y^{r+1}\} = \{Y^{r}\} + \{\Delta Y^{r+1}\} \qquad (8\text{-}35)$$

until convergency is reached.

Results and Discussion

First we used the exact solution (z-z, z-2z/2z-z) to check the accuracy of the results obtained by the numerical method. The error is defined as

$$Err = \sqrt{\frac{\sum_{k} \left(Y_k - Y(x_k)\right)^2}{\sum_{k} Y(x_k)^2}} \qquad (8\text{-}36)$$

where Y_k is the numerical result at $x = x_k$ and $Y(x_k)$ is the result from exact solution at $x = x_k$. The above definition of error can be considered as weighted average error where the weighting factors are just the value of reduced potential at each point evaluated. Hence it gives more weight to those points where reduced potentials have larger values. The advantage of this way of evaluating error is that it avoids the overestimation of error caused by the diffuse tail which has essentially zero potential. For example, if a point far from the surface has a reduced potential of 0.001 and the calculation gives 0.0009, the relative error will be 10% although the absolute error is only 0.0001. This potion of the diffuse layer is not technologically important, thus error is overestimated if no weighted average is used.

It turned out that if we use 500 elements with equal length, the absolute errors of numerical results were less than 3×10^{-4} and the relative error defined by eq.(8-36) was less than 5×10^{-5} for absolute values of reduced surface potentials less than or equal to 5. For greater surface (reduced) potentials, one needs to increase the number of elements or change the length of the elements. However, in practice the reduced surface potential is less likely beyond 5, therefore we restrict our error evaluation in this range. Figure 8-1 is the plots of exact solutions and numerical solutions when the surface potential is 5 and the electrolyte is 1-1, 1-2 or 2-1, respectively. Numerical results and exact solutions are indistinguishable, as the maximum difference between them is less than 3×10^{-4}. Therefore our numerical method is accurate enough to evaluate the accuracy of approximate solution for z-3z/3z-z and 2z-3z/3z-2z cases.

Table 8-1. Errors (%) from general solution and from symmetrical approximation.

Y0	1-2		2-1		1-3		3-1		2-3		3-2	
	gen	sym	gen	sym	gen	sym	gen	sym	gen	sym	gen	sym
1	0	3.8	0	4.0	1.4	6.7	.64	7.4	.47	3.1	.18	3.3
2	0	5.5	0	6.1	1.0	8.6	.92	10.8	.31	3.9	.14	4.3
3	0	6.1	0	7.3	.83	9.0	.78	12.5	.25	4.0	.10	4.7
4	0	6.3	0	7.9	.77	9.1	.61	13.3	.23	4.1	.08	4.8
5	0	6.4	0	8.2	.78	9.2	.49	13.8	.30	4.1	.08	4.8

Table 8-1 listed the percentile errors of the general solution Eq. (8-17) and the symmetrical approximation when the electrolyte is asymmetrical. It shows that our general solution gives much better results than the symmetrical approximation. Its error is

at most 1.3% in all the cases we considered here. Besides, the general solution does not involve a complicated formulation, although the expressions of α and β are cumbersome, they are constants and one only needs to evaluate them once for a given set of conditions such as surface potential and electrolyte type. The general solution also has "mirror symmetry" characteristics: the positive surface potential with z_c-$|z_a|$ electrolyte case is just the opposite of the negative surface potential with $|z_a|$-z_c electrolyte case. Plots in Figure 8-2 clearly show these characteristics. These characteristics result from the electrical diffuse layer, because if the sign of the surface potential changes, the original co-ions become counter ions. In figure 8-2 the numerical results are also plotted. Since the error is very small, numerical results and general solution can hardly be distinguished. It worthwhile to summarize that the selection of z value in the general solution is

(i)z-z: z = z_c or z = z_a, they give same results,

(ii)z-2z/2z-z: z = valence of the ion having fewer charges,

(iii)z-3z/3z-z: z = valence of counter ion,

(iv)2z-3z/3z-2z: z = valence of counter ion.

When determining the value of z, the sign of the charge should always be included.

There are other characteristics worth noticing. Given that the surface potential and the Debye length are the same, counter ions with higher charge shrink the diffuse layer more than those with less charge, and the charge of co-ions also affects the potential distribution. Figure 8-3 gives an example of this phenomenon. The surface potential is fixed and the potential distributions are plotted against reduced distance with the presence of different electrolytes. Figure 8-3a shows the potential distribution plots for which the

charges of co-ions are the same and only the charges of counter ions vary. It suggests that the charge of counter ions has great influence on the structure of the electrical diffuse layer. Figure 8-3b shows the potential plots when counter ion charges are fixed and co-ion charges vary. It also suggests that the higher the co-ion charge is, the more the diffuse layer extends, as higher charged co-ions are repulsed more by the surface.

Another feature needs to be mentioned is that a diffuse layer with a higher surface potential shrinks more quickly than the one with a lower surface potential, keeping other parameters the same. Figure 8-4 gives some examples. They are plots of the normalized potential distribution with the presence of different electrolytes. The normalization is done by dividing the potential with surface potential so that all the potential values lie in the range from 0 to 1. They show that the high potential shrinkage is more pronounced when the electrolyte is more asymmetrical.

The solution for the semi-infinite planar PB equation can be served as the first step to calculate the electrostatic interaction between two charged plates by using the linear superposition approximation(LSA) [Lev69]. The approximation states that the potential distribution in two overlapping double layers is the direct summation of potentials in two isolated double layers. Therefore, our general solutions provide a functional approximation for the potential distribution in overlapping planar double layers for any unmixed electrolyte cases. Then the calculation of the electrostatic interaction energy is reduced to an integration, for example, of disjoining pressure which is readily available as long as the potential profile is obtained [Der87].

The numerical method we used here can be easily adapted to any other one dimensional case. Only slight modification of the [K] matrix is necessary. It can also be used when any mixed electrolytes are present. It only needs a little modification of the {F} vector and subsequently of the $[K_T]$ matrix. However, like any other finite element method, the expansion from one the dimensional problem to the three-dimensional problem requires a significant effort to do spacial discretization and matrix assembly.

Summary

In this Chapter a general solution for the semi-infinite planar PB equation was discussed. It is exact for symmetrical electrolytes and z-2z/2z-z electrolytes. It is also a very good approximation for z-3z/3z-z and 2z-3z/3z-2z electrolytes with an error of no more than 1% or less. The evaluation is done by comparing with numerical results using the Galerkin weighted residual finite element method. This numerical method can be easily expanded to any one-dimensional case with any electrolytes. The general solution can be served as a functional approximation for potential distribution in two interacting double layers when calculating the electrostatic interaction energy.

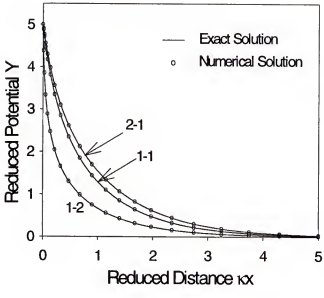

Figure 8-1. Plots of potential distributions near a charged plane surface with different electrolyte. In these cases exact solutions of PB equation are available. The numerical results agrees with exact results. The maximum difference between them is less than 3×10^{-4}. The surface potential is hold at 5.

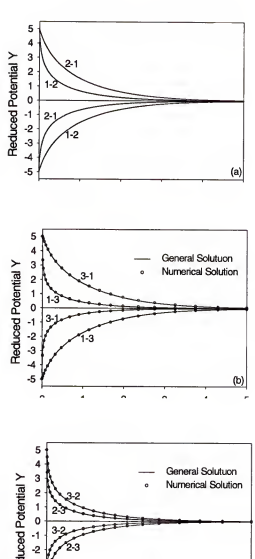

Figure 8-2. Plots of potential distributions near a charged plane surface. They show that the diffused layer with Y_0 surface potential and zc-lzal electrolytes is the same as the diffused layer with $-Y_0$ surface potential and lzal-zc electrolyte, except the sign is reversed. (a) 1-2/2-1 electrolytes, (b) 1-3/3-1 electrolytes, and (c) 2-3/3-2 electrolytes. In (b) and (c) the numerical results are also plotted. The general solutions essentially overlap with the numerical results.

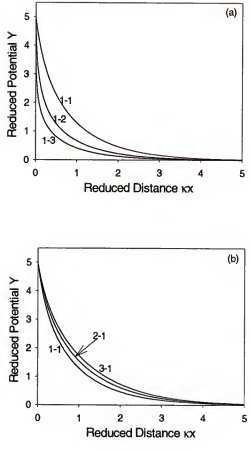

Figure 8-3. Plots of potential distributions near a charged plane surface. (a) the charge of co-ions hold constant, (b) the charge of counter ions hold constant. They suggest that the charges of electrolyte ions influence diffuse layer significantly.

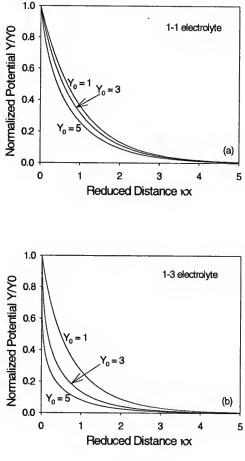

Figure 8-4. Plots of normalized potential distribution near a charged plane surface. The higher the surface potential is, the more fast the diffuse layer shrinks. This phenomenon is more pronounced when electrolyte is more asymmetrical. (a) 1-1 electrolyte, (b) 1-3 electrolyte.

CHAPTER 9
LIKE-CHARGE ELECTROSTATIC ATTRACTION IN CONFINED COLLOIDAL SYSTEMS

Introduction

The classic DLVO theory on the stability of colloidal systems has been well established and widely accepted for more than half a century [Ver48, Der87]. Strictly speaking, DLVO theory is only applied for an infinitely dilute colloidal system where the external source and drain of the electrolyte can be neglected. When the system is confined or concentrated, the application of this theory is not yet well studied. Figure 9-1a and 9-1b illustrate this argument. In Figure 9-1a the semi-infinite plan is not charged and the 1-1 electrolyte concentration n_0 is uniformly distributed in the surrounding solution. In Figure 9-1b the surface is positively charged. Thus in the vicinity of this surface anions are accumulated and cations are depleted. The exact distributions of electrolyte ions are described by Boltzmann distribution

$$n(x) = n_0 \exp\left(\frac{-zq\Phi}{kT}\right) \qquad (1)$$

where z is the charge of ions including the sign, q the unit charge, Φ the electric potential, k the Boltzmann constant and T the absolute temperature. At a location far away from the surface the local electroneutrality is maintained and the electric potential is essentially

zero, therefore the concentrations of ions go back to n_0. Now the question is, comparing Figure 9-1b to Figure 9-1a, that where the accumulated anions come from and where the depleted cations go. The only source and drain of ions are the surrounding solution. Therefore, if the solution is not infinitely large in volume, then the accumulation and depletion of ions cannot be neglected. Mass conservation should be always maintained during charging process. One could argue that if the solution volume is finite, then there is no location within the solution where the electric potential is exactly zero. However, it should be noticed that in this case one type of ion is always in accumulation and the other type of ion is always in depletion. The source and drain of ions still need to be specified. One should notice the origin of the surface charges could be due to an adsorption or desorption/dissociation of charged species. When considering mass conservation, the surface species should also be considered. As will be shown later in this Chapter, the inconsistence of electrolyte ion concentrations before and after surface charging are not due to the surface adsorption or desorption/dissociation. For example, assume the negative surface charges are caused by desorption of cations, then the average cation concentration in the surrounding solution is larger than that before charging of surface, meanwhile the average anion concentration in surrounding solution should be the same as that before charging since the is no source or drain of anions. Now let us consider the Boltzmann distribution of anions. In the vicinity of the negatively charged surface, the anion is depleted, and at a distance far away from the surface, the anion concentration keeps at the original concentration. Therefore after charging of the surface, the average anion concentration is less than that before charging. The mass is not conserved

according to the classical treatment unless the surrounding solution has infinite volume. It also should be noted that not only anions, but also cations are not conserved according to classical treatment. The surface charges are not equal to the accumulation of cations only, but rather the difference between the concentrations of accumulated cations and depleted anions.

Since the mass is not conserved, then how does the classical treatment retain charge neutrality? Actually, the whole system is forced to be neutralized in the classical theory because the integration of charge density, ρ, over the volume of surrounding solution in the whole system is set to be equal to the surface charge density, σ, as described by Eq. (9-2) for the semi-infinite planar symmetry case where the surface is located at x=0

$$\sigma = -\int_0^\infty \rho dx \qquad (9\text{-}2)$$

According to Poisson equation

$$\frac{d^2\Phi}{dx^2} = -\frac{\rho}{\varepsilon} \qquad (9\text{-}3)$$

the surface charge can be written as

$$\sigma = \varepsilon\int_0^\infty \frac{d^2\Phi}{dx^2}dx = \varepsilon\int_0^\infty d\left(\frac{d\Phi}{dx}\right) = -\varepsilon\left(\frac{d\Phi}{dx}\right)_{x=0} \qquad (9\text{-}4)$$

Therefore, the classical treatment still maintains total charge neutrality, although, mass is not conserved. The classic DLVO theory did not discuss mass conservation and, to our knowledge, there is no theory developed to specifically study this problem since the

establishment of DLVO theory. Therefore, the application of DLVO theory on confined or concentrated colloidal system is under serious question prior to a a thorough investigation on this issue.

Coincidently, many experiments suggest that in a confined or concentrated colloid system there could be a long range attractive electrostatic force which was not predicted by DLVO theory [Luk63, Kos73, Ise83, Tat92, Pal94, Tat94, Ito94, Kep94, Tat95, Cro94, Cro96, Lar97]. A numerical calculation showed that in a confined system a long-range attractive electrostatic force did exist [Bow98]. However, two independent groups disproved this result [Neu99, Sad99, Sad00]. It was suggested that the only possible source of long range attractive electrostatic forces was from the distribution of electrolytes, thus the osmotic pressure [Sad00]. Does the mass conservation in confined/concentrated system have anything to do with the possible long range attractive force? To answer that is the aim of this paper. To do so the classical formulations of double layer electrostatic energies have to be rejected since they are based on infinitely diluted system, and a set of new relationship has to be established. In the following discussions, we define our model system first. It is a one dimensional planar symmetry confined system. Second the linearized Poisson-Boltzmann equation is solved in our model system. Third the double layer electrostatic energies are formulated by the variational principle based on the solution of the linearized P-B equation. Fourth the pre-exponential constants of Boltzmann distribution are discussed. Last numerical results are given and compared with the classical results.

We found that the paired interaction of like-charged plates could indeed be attractive at long separation distances and repulsive at short separation distances. The attractive force is a function of confinement, electrolyte concentration, and surface charge density. The paired interaction energies become identical to the classical formulation when the confinement is removed or the colloid concentration is infinitely dilute.

Theory

The Model System

A good model system should simplify mathematics as much as possible while maintain its physical significance. It is well-known that P-B equation has no analytical solutions except some extreme cases such as low potential and one dimension. Therefore our model should be one dimensional where only linearized P-B is considered. Also our model should be a confined system, thus we can add the mass conservation condition for electrolytes. We designed our model as graphed in Figure 9-2. Two infinite plates, I and III, are fixed at $x = 0$ and $x = D$. One infinite plate, II, with finite pores is placed between the two fixed plates and can move in the x direction. For plate II, the pore sizes are negligible when compared to the total plate area, and the existence of the pores does not alter the surface charge and electric field distribution significantly. That is, we assume the edge perturbation on electric field distribution can be neglected. Electrolyte solution is held in the space between the two fixed plates, I and III. To keep our discussion simple, We assume the surface charging is caused by desorption of cations on the plate surfaces, which is similar to the polystyrene latex particle case. This simplification does not hinder

the generality of the method we provide. Before surface charging, the electrolyte in the solution is an unmixed 1-1 type with concentration n_0. The electrolyte is uniformly distributed in the entire space between plates I and III. We set the electric potential Φ at this condition to be zero. When charging begins, the cations on the surfaces start to enter the solution and the surfaces begin charging negatively. Meanwhile, plate II starts to move in accordance with the interactions of charged plate pairs I-II and II-III. After a sufficiently long time the system reaches equilibrium and plate II comes to rest at a specific position, d, corresponding to the minimum in Gibbs free energy of the whole system.

Solutions to Linearized P-B Equation

As discussed before, the Boltzmann distribution in the form of Eq. 9-1 invalidates mass conservation if the pre-exponential constant and the zero point of the electric potential are not appropriately chosen. Therefore, we have to introduce three unknown constants, N_{C1}, N_{C2} and N_A, for the pre-exponential terms representing dissociated cations from surface, the background cations, and anion Boltzmann distributions, respectively:

$$n_{C1} = N_{C1}\exp\left(-\frac{z_{C1}q\Phi}{kT}\right) = N_{C1}\exp\left(-\frac{zq\Phi}{kT}\right) \approx N_{C1} - N_{C1}\frac{zq\Phi}{kT} \quad (9\text{-}5)$$

$$n_{C2} = N_{C2}\exp\left(-\frac{z_{C2}q\Phi}{kT}\right) = N_{C2}\exp\left(-\frac{zq\Phi}{kT}\right) \approx N_{C2} - N_{C2}\frac{zq\Phi}{kT} \quad (9\text{-}6)$$

$$n_A = N_A\exp\left(-\frac{z_Aq\Phi}{kT}\right) = N_A\exp\left(\frac{zq\Phi}{kT}\right) = N_A + N_A\frac{zq\Phi}{kT} \quad (9\text{-}7)$$

where the subscripts C1, C2 and A denote dissociated cations from surface, background cations and anions, respectively, and $z = z_{C1}=z_{C2} = -z_A$. Upon inserting Eqs. 9-5, 9-6 and 9-7 into Eq.9-3, we obtain the linearized P-B equation for the system

$$\frac{d^2\Phi}{dx^2} = K^2\Phi + b \qquad (9\text{-}8)$$

where

$$K = \sqrt{\frac{z^2q^2}{\varepsilon kT}(N_{C1} + N_{C2} + N_A)} \qquad (9\text{-}9)$$

and

$$b = \frac{zq}{\varepsilon}(N_A - N_{C1} - N_{C2}) \qquad (10)$$

The boundary conditions we considered here are two cases as usual, namely (i)surface charge constant and (ii)surface potential constant. The system can be divided into two compartments, 1 and 2, as shown in Figure 9-2. In each compartment Eq. 9-8 applies and we denote the potential in compartment 1 as Φ_1 and the potential in compartment 2 as Φ_2. In order to generalize the formulations we set the left plate of each compartment to x_1, and the right plate to x_2. In compartment 1, $x_1 = 0$ and $x_2 = d$, and in compartment 2, $x_1 = d$ and $x_2 = D$.

(i) Surface charge constant case:

The boundary conditions are

$$\sigma_{x_1} = -\varepsilon\left(\frac{d\Phi}{dx}\right)_{x=x_1} \qquad (9\text{-}11)$$

$$\sigma_{x_2} = \varepsilon\left(\frac{d\Phi}{dx}\right)_{x=x_2} \qquad (9\text{-}12)$$

and the solution is

$$\Phi = \frac{\sigma_{x_1}\cosh(K(x_2-x)) + \sigma_{x_2}\cosh(K(x_1-x))}{\varepsilon K \sinh(K(x_2-x_1))} - \frac{b}{K^2} \qquad (9\text{-}13)$$

(ii) Surface potential constant case:

The boundary conditions are

$$\Phi(x_1) = \Phi_{x_1} \qquad (9\text{-}14)$$

$$\Phi(x_2) = \Phi_{x_2} \qquad (9\text{-}15)$$

and the solution is

$$\Phi = \frac{(\Phi_{x_1}K^2 + b)\sinh(K(x_2-x)) - (\Phi_{x_2}K^2 + b)\sinh(K(x_1-x))}{K^2\sinh(K(x_2-x_1))} - \frac{b}{K^2} \qquad (9\text{-}16)$$

Gibbs free energy for interacting planar electric double layers in confined system

Since classic treatments of overlapping Gibbs free energies are all related to the infinite separation state, we cannot directly use those results on our confined system. In this paper, we will derive a set of expression by the variational principle [Red93]. Let us start from Eq.9-8. It can be changed to

$$\frac{d^2\Phi}{dx^2} - K^2\Phi - b = 0 \qquad (9\text{-}17)$$

Let $\delta\Phi$ be a small linear variation of Φ, then

$$\int_{x_1}^{x_2}\left[\left(\frac{d^2\Phi}{dx^2}\right) - K^2\Phi - b\right]\delta\Phi\, dx = 0 \qquad (9\text{-}18)$$

The weak form of Eq. 9-18 is obtained by performing a integration by parts:

$$\delta\Phi\left(\frac{d\Phi}{dx}\right)_{x=x_2} - \delta\Phi\left(\frac{d\Phi}{dx}\right)_{x=x_1} - \int_{x_1}^{x_2}\left(\frac{d\Phi}{dx}\right)\left(\frac{d\delta\Phi}{dx}\right)dx - \int_{x_1}^{x_2} K^2\Phi\,\delta\Phi dx - \int_{x_1}^{x_2} b\,\delta\Phi dx = 0 \quad (9\text{-}19)$$

Since $\delta\Phi$ is a linear variation of Φ, then the Eq. 9-19 is equivalent to

$$\delta\Phi\left(\frac{d\Phi}{dx}\right)_{x=x_2} - \delta\Phi\left(\frac{d\Phi}{dx}\right)_{x=x_1} - \delta\left\{\int_{x_1}^{x_2}\left[\frac{1}{2}\left(\frac{d\Phi}{dx}\right)^2 + \frac{1}{2}K^2\Phi^2 + b\Phi\right]dx\right\} = 0 \quad (9\text{-}20)$$

Multiplying ϵ on both sides and considering Eqs. 9-11 and 9-12, one obtains

$$\delta\Phi\cdot\sigma_{x_2} + \delta\Phi\cdot\sigma_{x_1} - \delta\left\{\int_{x_1}^{x_2}\left[\frac{\varepsilon}{2}\left(\frac{d\Phi}{dx}\right)^2 + \frac{\varepsilon}{2}K^2\Phi^2 + \varepsilon b\Phi\right]dx\right\} = 0 \quad (9\text{-}21)$$

For the surface charge constant case, the potential Φs at the surfaces are not fixed and Eq. 9-21 can be changed to

$$\delta\left\{\Phi_{x_2}\sigma_{x_2} + \Phi_{x_1}\sigma_{x_1} - \int_{x_1}^{x_2}\left[\frac{\varepsilon}{2}\left(\frac{d\Phi}{dx}\right)^2 + \frac{\varepsilon}{2}K^2\Phi^2 + \varepsilon b\Phi\right]dx\right\} = 0 \quad (9\text{-}22)$$

For the surface potential constant case, the potential Φs at the surfaces are fixed, and their variations are zero. Therefore Eq. 9-21 can be simplified to

$$\delta\left\{-\int_{x_1}^{x_2}\left[\frac{\varepsilon}{2}\left(\frac{d\Phi}{dx}\right)^2 + \frac{\varepsilon}{2}K^2\Phi^2 + \varepsilon b\Phi\right]dx\right\} = 0 \quad (9\text{-}23)$$

Variational principle states that the solution to Eq. 9-17 will minimize the variation of the functions in Eqs. 9- 22 and 9-23. In such a system only the Gibbs free energy is minimized. Therefore the Gibbs free energy for the paired interaction is

$$G = (\Phi\sigma)_{x_2} + (\Phi\sigma)_{x_1} - \int_{x_1}^{x_2}\left[\frac{\varepsilon}{2}\left(\frac{d\Phi}{dx}\right)^2 + \frac{\varepsilon}{2}K^2\Phi^2 + \varepsilon b\Phi\right]dx \quad (9\text{-}24)$$

for surface charge constant and

$$G = -\int_{x_1}^{x_2}\left[\frac{\varepsilon}{2}\left(\frac{d\Phi}{dx}\right)^2 + \frac{\varepsilon}{2}K^2\Phi^2 + \varepsilon b\Phi\right]dx \quad (9\text{-}25)$$

for surface potential constant. It is easy to verify that the units in Eq. 9-21 are indeed units of energy. Inserting the expression of Φ under different boundary conditions one can obtain the explicit expressions of Gibbs free energy

$$\begin{aligned} G = {} & \frac{1}{2K\varepsilon}\left[2\sigma_{x_1}\sigma_{x_2}\frac{1}{\sinh(K(x_2-x_1))} + \left(\sigma_{x_1}^2+\sigma_{x_2}^2\right)\coth(K(x_2-x_1))\right] \\ & -(\sigma_{x_1}+\sigma_{x_2})\frac{b}{K^2} + \frac{\varepsilon b^2}{2K^2}(x_2-x_1) \end{aligned} \quad (9\text{-}26)$$

for surface charge constant, and

$$\begin{aligned} G = {} & \frac{\varepsilon K}{2}\left\{\begin{array}{l} 2\left(\Phi_{x_1}+\frac{b}{K^2}\right)\left(\Phi_{x_2}+\frac{b}{K^2}\right)\frac{1}{\sinh(K(x_2-x_1))} \\ -\left[\left(\Phi_{x_1}+\frac{b}{K^2}\right)^2+\left(\Phi_{x_1}+\frac{b}{K^2}\right)^2\right]\coth(K(x_2-x_1)) \end{array}\right\} \\ & +\frac{\varepsilon b^2}{2K^2}(x_2-x_1) \end{aligned} \quad (9\text{-}27)$$

for surface potential constant. It is very interesting to compare above Gibbs free energy expressions with the classical ones [Der87]:

$$\Delta G = \frac{1}{2\kappa\varepsilon}\left[2\sigma_{x_1}\sigma_{x_2}\frac{1}{\sinh(\kappa(x_2-x_1))}+\left(\sigma_{x_1}^2+\sigma_{x_2}^2\right)\left[\coth(\kappa(x_2-x_1))-1\right]\right] \quad (9\text{-}28)$$

$$\Delta G = \frac{\varepsilon\kappa}{2}\left[2\Phi_{x_1}\Phi_{x_2}\frac{1}{\sinh(\kappa(x_2-x_1))}-\left(\Phi_{x_1}^2+\Phi_{x_2}^2\right)\left[\coth(\kappa(x_2-x_1))-1\right]\right] \quad (9\text{-}29)$$

for surface charge constant and surface potential constant, respectively. Recall that the classic results (Eqs.9-28 and 9-29) are in the form of Gibbs free energy change and are obtained by

$$\Delta G = G(x_2 - x_1) - G(\infty) \qquad (9\text{-}30)$$

In our confined system if we apply Eq.9-30 then our results take the form of well-known Eqs.9-28 and 9-29. It should be noted that when the distance between two plates become infinite, then b vanishes and K becomes the classic inverse Debye length κ. Thus the classic results are specific solutions assuming infinite conditions, while our new results are for a general scenario.

It is worthwhile to show that the above new formulations can be also obtained by using Derjaguin's disjoining pressure method [Der87]. Derjaguin's disjoining pressure, Π, is given by

$$\Pi = -\int_0^{\Phi}\rho(\Phi)d\Phi - \frac{\varepsilon}{2}\left(\frac{d\Phi}{dx}\right)^2 \qquad (9\text{-}31)$$

The charge density in the solution, ρ, is

$$\rho = -\varepsilon K^2\Phi - \varepsilon b \qquad (9\text{-}32)$$

Then the disjoining pressure is

$$\Pi = \frac{1}{2}\varepsilon K^2\Phi^2 + \varepsilon b\Phi - \frac{1}{2}\varepsilon\left(\frac{d\Phi}{dx}\right)^2 \qquad (9\text{-}33)$$

Inserting the potential and potential gradient profiles under different conditions into Eq. 9-33 we obtain

$$\Pi = \frac{\sigma_{x_1}^2 + \sigma_{x_2}^2}{2\varepsilon\sinh(Kd)^2} + \frac{\sigma_{x_1}\sigma_{x_2}\cosh(Kd)}{\varepsilon\sinh(Kd)^2} - \frac{1}{2}\frac{\varepsilon b^2}{K^2} \qquad (9\text{-}34)$$

for constant charge, and

$$\Pi = \frac{\varepsilon\left[\left(\Phi_{x_1}K^2 + b\right)^2 + \left(\Phi_{x_2}K^2 + b\right)^2\right]}{2K\sinh(Kd)^2} - \frac{\varepsilon\left(\Phi_{x_1}K^2 + b\right)\left(\Phi_{x_2}K^2 + b\right)\cosh(Kd)}{K\sinh(Kd)^2} - \frac{1}{2}\frac{\varepsilon b^2}{K^2} \qquad (9\text{-}35)$$

for constant potential. In the above equations $b = x_2 - x_1$. It is interesting to compare these results with the classic ones,

$$\Pi = \frac{\sigma_{10}^2 + \sigma_{20}^2}{2\varepsilon\sinh(\kappa d)^2} + \frac{\sigma_{10}\sigma_{20}\cosh(\kappa d)}{\varepsilon\sinh(\kappa d)^2} \qquad (9\text{-}36)$$

for constant charge, and

$$\Pi = \frac{\varepsilon\kappa\left(\Phi_{10}^2 + \Phi_{20}^2\right)}{2\sinh(\kappa d)^2} - \frac{\varepsilon\kappa\Phi_{10}\Phi_{20}\cosh(\kappa d)}{\sinh(\kappa d)^2} \qquad (9\text{-}37)$$

for constant potential. It can be clearly seen that once the confinement is removed, then the parameter b vanishes, K becomes κ, and then the Eqs.9-34 and 9-35 become Eqs. 9-

36 and 9-37, respectively. That means DLVO results are just special cases of our more generous results.

The interaction energy can be obtained by

$$\Delta G = \int_d^\infty \Pi(d)dd \qquad (9\text{-}38)$$

which states how much energy is released when two plates with separation distance d were moved infinitely apart. In the classical treatment, the Eqs. 9-28 and 9-29 can be obtained by combining Eq. 9-38 with Eq. 9-36 and 9-37. However, in our confined system, only under the constant charge condition can we follow this procedure to obtain the interaction energy. This is because the parameter K and b are invariant with separation distance, and they are unknown functions of separation distance under the constant potential condition. Thus the integration in Eq. 9-38 only applies to constant charge case in our discussion here, and we obtain

$$\Delta G = \frac{1}{2K\varepsilon}\left[\frac{2\sigma_{x_1}\sigma_{x_2}}{\sinh(Kd)} + \left(\sigma_{x_1}^2 + \sigma_{x_2}^2\right)\coth(Kd)\right] - \frac{\sigma_{x_1}^2 + \sigma_{x_2}^2}{2K\varepsilon} + \frac{\varepsilon b^2}{2K^2}d \qquad (9\text{-}39)$$

Now, let us compare Eq. 9-26 and Eq. 9-39. They are identical except the second term from the right-hand-side of each equation. These two terms do not change with the separation distance because they are constants. Therefore, the different between Eq.9-26 and Eq.9-39 are trivial since we are interested in the change of the free energy, not the absolute value of the free energy.

We have obtained the formulation of Gibbs free energy for the double layer interaction in a confined system. However, we cannot calculate the Gibbs free energy-

separation distance function yet, because we still do not know the constants N_A, N_{C1} and N_{C2} in K and b. The following section will evaluate these constants and discuss their physical meaning.

Pre-exponential constants N_A, N_{C1} and N_{C2}

Application of the mass conservation condition is the first attempt to obtain the pre-exponential constants N_A, N_{C1} and N_{C2}.

$$\int_0^d n_A(x)dx + \int_d^D n_A(x)dx = n_0 D \qquad (9\text{-}40)$$

$$\int_0^d n_{C1}(x)dx + \int_d^D n_{C1}(x)dx = \frac{\Sigma}{-ze} \qquad (9\text{-}41)$$

$$\int_0^d n_{C2}(x)dx + \int_d^D n_{C2}(x)dx = n_0 D \qquad (9\text{-}42)$$

where Σ is the sum of surface charge density and

$$\Sigma = \sigma_{10} + \sigma_{20} + \sigma_{30} + \sigma_{40} \qquad (9\text{-}43)$$

and σ_{10}, σ_{20}, σ_{30}, and σ_{40} are the charge densitise on surfaces 1 to 4, respectively, as shown in Figure 9-2. It should be noted that the Eq.9-41 comes from assuming the charging is caused by desorption of cations from the surfaces. When the valence of dissociated ions from surface is positive, z, then the valence of surface charge is negative, -z. The surface charge density is also negative ($\Sigma < 0$), thereby causing the right-hand-side of Eq. 9-41 to be positive. Applying Eqs. 9-5, 9-6, 9-7, and the expression of Φ under specific boundary conditions one will get three equations with three undetermined quantities N_A, N_{C1}, and N_{C2}. It turns out, however, that two of the three equations are equivalent, so we cannot

determine N_A, N_{C1}, and N_{C2} unequivocally. Only relationships among themselves are available. They are

$$N_{C1} = \frac{N_A \Sigma}{-zeD\left(2N_A - n_0\right)} \qquad (9\text{-}44)$$

$$N_{C2} = \frac{n_0 N_A}{2N_A - n_0} \qquad (9\text{-}45)$$

That means there are numerous selections of pre-exponential constants that will satisfy mass conservation. The reference state, at which the surface is not charged, states that the pre-exponential constants for background electrolyte should be n_0, since at this state the potential is defined to be zero. That means at $\Phi = 0$, the concentrations of the background electrolyte cations and anions should be the same. Selection of proper pre-exponential constants should not be at odds with the reference state. Therefore,

$$N_A = N_{C2} \qquad (9\text{-}46)$$

Inserting Eq. 9-46 into Eqs. 9-44 and 9-45, we obtain

$$N_{C1} = \frac{\Sigma}{-zeD} \qquad (9\text{-}47)$$

and

$$N_A = N_{C2} = n_0 \qquad (9\text{-}48)$$

That indicates the pre-exponential constants are the average concentration of the ions, which is in agreement with Sogami and Ise [Sog84].

Numerical examples

In this section, the paired interaction energy and the total energy of the system will be discussed with the aid of numerical examples. The examples are chosen to follow the conditions of the experiments conducted by Larsen and Grier [Lar97]. Polystyrene latex particles of diameter $2R = 0.652 \pm 0.005\ \mu$ and about 1E5 charge groups per particle were dispersed into deionized water. The actual ionized groups are assumed to be far less then this number. Ion exchange resin was used to keep the background electrolyte concentration as low as possible. The solid loading was $\phi = 0.02$ by volume. They found that a denser ordered structure with ~ 1.8 μ interparticle separation coexisted with a looser disordered structure. They concluded that the ordered structure was metastable with appreciable energy trap associated with each particle.

In our examples, we assume 0.5 % charge groups are dissociated, giving -6E-5 C/m^2 charge density. The background electrolyte concentration is assumed to be 1E-6 M, slightly larger than that in pure water, because of possible contamination by ion leaching from container walls or dissolved carbon dioxide. The surface potential at infinite separation is about -26.1 mV, which is calculated from $\Phi_0 = \sigma/\epsilon\kappa$. The interparticle distance can be accessed as follows. Assume the volume of the solution is V, then the total particle volume is ϕV, and the number of particles is $3\phi V/4\pi a^3$. Assume all the particles form simple cubic structures, then the closest surface to surface distance between two particles, d_{ave}, is then

$$d_{ave} = \left[\left(\frac{4\pi}{3\phi} \right)^{1/3} - 2 \right] R \qquad (9\text{-}49)$$

We set the confinement, D, to be the distance between the fixed plates, to be $2d_{ave}$, thus the change in D relates the change of solid loading, and vice versa. In Larson and Grier's work the solid loading was reported to be $\phi = 0.02$. According to Eq. 9-49 the calculated average separation is ~1.284 μ, which is against the experimental observation. Ito et al. [Ito94] used $\phi = 0.02$ polystyrene latex particles with 0.96 μ diameter and resulted in much denser appearance in micrograph image. Therefore we believe in Larson and Grier's work either some particles settled or the reported particle loading was wrong. In our examples the particle loading is chosen to be $\phi = 0.002$, and it gives $d_{ave} = 3.519$ μ and D = 7.038 μ. Furthermore, in the polystyrene latex particle system the particle interaction is homogeneous, that is, the surface charge and surface potential on each particle are identical. Therefore Eqs. 9-26 and 9-27 can be simplified to

$$G = \frac{\sigma^2}{\varepsilon K}\coth\left(\frac{K}{2}\left(x_2 - x_1\right)\right) - \frac{2b\sigma}{K^2} + \frac{\varepsilon b^2}{2K^2}\left(x_2 - x_1\right) \qquad (9\text{-}50)$$

and

$$G = -\varepsilon K\left(\Phi_0 + \frac{b}{K^2}\right)^2 \tanh\left(\frac{K}{2}\left(x_2 - x_1\right)\right) + \frac{\varepsilon b^2}{2K^2}\left(x_2 - x_1\right) \qquad (9\text{-}51)$$

for surface charge constant and surface potential constant, respectively.

After determining all the required parameters, numerical examples can now be given. We will consider the surface charge constant case first. The paired interaction energy between plate I and II, as a function of separation distance, is plotted in Figure 9-3 according to Eq. 9-50. Here the value of $(x_2 - x_1)$ is just equal to d. The contribution of each term in Eq. 9-50 is also plotted separately in Figure 9-3. It shows that the first term

is exactly the same as the classic results, except a constant which results from different reference states. It provides a repulsive component in total interaction, as predicted by the classic theory. The second term is a constant as long as the confinement/particle loading is given. Actually, it is a redundant term since it only changes the absolute value of the Gibbs free energy, and what we interested in is the change of the Gibbs free energy. We can neglect it safely. The third term is the key contribution of our model. It increases as the separation distance increases, resulting in an attractive component of the total interaction energy. Therefore, the total interaction is attractive at long separation distance and repulsive at short separation distance, and the energy - distance curve possesses a minimum. The location of the minimum can be calculated as 1.412 μ from Eq.9-52:

$$d_{\min} = \frac{2}{\kappa}\sinh^{-1}\left(\frac{\sigma\kappa}{b\varepsilon}\right) \qquad (9\text{-}52)$$

The attractive component is linearly dependent on the separation distance. From it we can find the attractive force since force is the negative gradient of energy. Therefore, by considering the expression of b, the attractive force is

$$F = -\frac{\Sigma^2 kT}{2z^2e^2D^2\left(2n_0 + \frac{\Sigma}{-zeD}\right)} \qquad (9\text{-}53)$$

The dependence of the attractive force on the confinement factor, D, in terms of the solid loading, ϕ, via Eq.9-49 is plotted in Figure 9-4. It conspicuously shows that the attractive force increases remarkably as the confinement/solid loading increases. This in agreement with the experimental findings that long range attractive forces among like-charged

particles are always observed in confined or concentrated system. The attractive force as a function of background electrolyte concentration is plotted in Figure 9-5, in which the increase of background electrolyte concentration cause the attractive forces to decrease drastically. This again agrees well with experimental observations. Ion exchange resins are usually employed to promote the attractive force. Surface charge density also has an influence on the attractive force. Figure 9-6 is the plot of the attractive force as a function of the surface charge density. It shows that with increasing of the surface charge density the attractive force also increases. The effect of particle diameter on the attractive force can also be discussed if we take the relation given by Eq. 9-49 into consideration. The attractive force is much more prominent when particles are submicron in size, as shown in Figure 9-7.

It should be noted that in our model system the attractive force only appears in paired interaction. If multibody interactions are considered the attractive forces disappear in our model system, as shown in Figure 9-8, because the two attractive forces exerted on the movable plates are equal in magnitude and opposite in direction. The total interaction energy in the system, given by the summation of paired interaction energy in compartment 1 and 2, shows no energy minimum. The energetically favorable state for this system is when the plates are equally spaced. This result comes from that fact that the paired attractive force is independent of separation distance, which results most likely from the linearization of the Poisson - Boltzmann equation. Therefore, our model did not exclude the possibility of forming order/disorder structures or structures with the coexistence of high and low densities. Unfortunately, the analytical solution for nonlinear

Poisson - Boltzmann equation is not available in our system. It implies that solving the nonlinear PB by means of numerical methods under the frame of our system could be very rewarding in terms of gaining understanding of the ordered colloidal structures.

It is meaningful to plot the potential distribution in the system. Figures 9-9, 9-10, and 9-11 are the plots of the potential distributions of the movable plates at different locations. It turns out that the potential in the solution could become positive, which is not possible in classic treatment. It also implies that the potential is not additive; the potential of interacting double layers is not even close to the addition of two isolated double layer potentials in the confined/concentrated system. One more important fact lies in that the integral of the potential over the entire space is zero. This is a direct result of mass conservation under the linearized Boltzmann distribution condition. It is interesting to point out that at d equals d_{min} given by Eq.9-52, the potential at the middle of the compartment 1 is zero, as shown in Figure 9-10. Therefore, it is clear that the attractive force is related to the sign reversal of the potential. As long as the sign of the potential in the solution becomes opposite to the sign of the surface potential the attractive force appears. This also indicates why the classic treatment does not predict the attractive force since the sign reversal in the solution never happens.

Interactions under the constant potential condition in the confined/concentrated system are much more complicated than that under the constant charge condition. This is because the ion concentrations in the solution are a function of the separation distance. There is no close-formed expression available for the ion concentration-separation distance relationship. Numerical calculation with iteration should be used to determine

the ion concentrations at each separation distance. The procedure is described as follows: (i) The separation distance and surface potential should be specified. (ii) A starting value of surface charge density should be given. The value at infinite separation is a good choice. Then the value K and b can be calculated according to Eqs. 9-9 and 9-10. (iii) A new value of total surface charge density, Σ, is calculated according to

$$\Sigma = 2\varepsilon K\left(\Phi_0 + \frac{b}{K^2}\right)\left[\tanh\left(\frac{K}{2}d\right) + \tanh\left(\frac{K}{2}(D-d)\right)\right] \qquad (44)$$

(iv) According to the calculated Σ, a new set of K and b are obtained. (v) Steps (iii) and (iv) are repeated until Σ converges to a fixed value. Then the paired energy, total energy, and potential distributions can be evaluated.

The paired interaction energy, as a function of separation distance, is plotted in Figure 9-12. The contribution of each term is also plotted in the figure. The first term gives a repulsive interaction at short separation distance and the repulsive interaction is screened when distance increases, analogue to the classic results. But it also gives an attractive interaction at long separation. This is not accounted for by the classic treatment, and it is originated from the b parameter. The second term gives an almost constant attractive interaction at short and intermediate separation, which is similar to the constant charge chase. However, at long separation it becomes repulsive. The b parameter is also the cause of this repulsion. The total interaction energy thus shows repulsion at short separation, attractive at intermediate separation, and repulsive again at long separation. In order to understand this unique profile, it is helpful to plot the surface charge density as a function of separation distance. This is provided in Figure 9-12. First let us look at the

surface charge density change in compartment 1. It is denoted as $\sigma 1$ in the figure. When the two plates are very close the surface charge density drops, indicating some of the cationic ions go back to the surface. When the separation increases, the surface charge groups dissociate and the surface charge density increases and becomes stable at intermediate separation over a quite large region of separations. These results are similar to the classic results. However, when the separation becomes large, the surface charge density decreases again. This is induced by the surface charge density change in compartment 2. The total electrolyte concentration decreases because of the association of surface ions in compartment 2 due to the approaching of the two surface in compartment 2, thus the K parameter decreases. This is analogue to the infinite separation case, in which the surface charge density is equal to $\epsilon\kappa\Phi_0$; decreasing κ will cause surface charge density to decrease. The mutual influence of charging/discharging process is a unique characteristic of confined system.

Since over a fairly large intermediate separation range the total surface charges in the system do not change significantly, it is similar to the surface charge constant case. Therefore, all the discussions about the influence on the attractive force by confinement, electrolyte concentration, surface charge density, and particle size are applicable to the surface potential constant case in this range of separation. Only at short separation distances are these two cases expect to be different. However, the total energy curve in Figure 9-13 suggests that the attractive forces exerted on the movable plate II are canceled with each other at intermediate separation. Only at short separations are these two attractive forces different in magnitude. But here the repulsive force from the first term of

energy formulation dominates the attractive force. Therefore, the preferred position of the movable plate is still in the middle.

The potential profiles at three different separation distances are plotted in Figures 9-14, 9-15, and 9-16. They clearly show a potential reversal in the solution. The integral of the potential profile over whole domain is also zero, as in the constant charge case. It is the indication of mass conservation under the condition of the linearized Boltzmann distribution. It is interesting to point out that the paired interaction energy minimum in compartment 1 is at the separation where the potential in the middle plane of compartment 1 is zero, again, as in the constant charge case. It reveals that the attractive force is a result of the sign reversal of potential in the solution.

Summary

In this Chapter we provided a model for a simple confined one-dimensional planar symmetry scenario and the method to obtain paired and total energies for electrostatic interactions in colloid system. From this we found that the classic DLVO electrostatic interaction energy formulations are just special cases of our more general ones. We found that the long range attractive force between two like-charged bodies does indeed exist. It results from the sign reversal of electric potential in the solution, which originates from the mass conservation condition. The predicted attractive force is influenced by the confinement, the background electrolyte concentration, the surface charge density/surface potential, and the particle size. However, the total interaction energy of the system shows a minimum only at the average separation of each of the plates due to the cancellation of

the attractive components. Future studies on nonlinearized Poisson - Boltzmann equation and/or higher dimensional interactions by numerical methods are highly needed to simulate the order/disorder structure in colloidal systems. Nevertheless, our model reveals the unique characteristics of confined/concentrated system for the first time since the establishment of Gouy-Chapman diffuse layer theory one century ago and the establishment of DLVO theory half century ago.

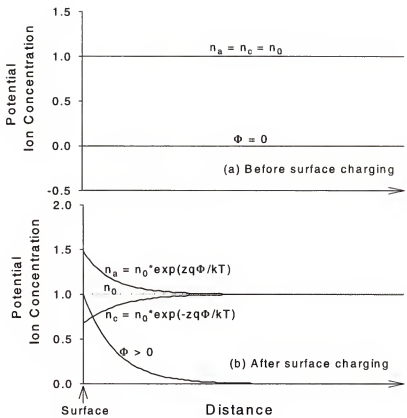

Figure 9-1. Schematic graph of electric potential and electrolyte ion concentration distributions near a semi-infinite planar surface (a) before and (b) after surface charging. Before charging the potentials are zero everywhere in the solution, and both anions and cations are uniformly distributed in the solution with concentration being n_0. After surface charging the surface is assumed to be positively charged and the anion concentration near the surface is greater than n_0 and the cation concentration less than zero. At the position far away from the surface, the potential and ion distributions are remains the same. This scenario breaks the mass conservation law.

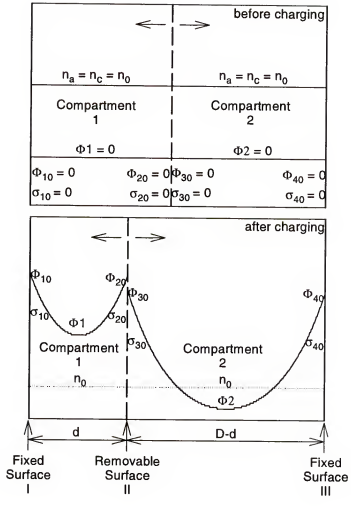

Figure 9-2. Schematic graph of the confined one-dimensional model system. It is composed of three infinitely large planar surfaces. Two fixed non-permeable surfaces hold an electrolyte solution between them, defining the confinement. One movable and permeable surface locates between the fixed surface, dividing the system into two compartments. Before charging, the potentials are zero all over the entire confined space, and the anions and cations are uniformly distributed. There is no preference for the removable surface to locate. After charging, the potentials become non-zero, and their distributions are given be Poisson-Boltzmann equation. The distributions of cations and anions are adjusted accordingly. The removable surface will rest at a specific location corresponding to the lowest system energy after equilibrium is reached.

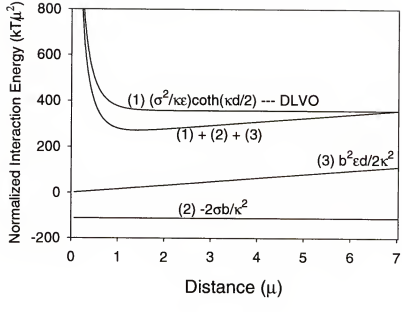

Figure 9-3. The plot of paired interaction energy as a function of separation distance. The paired interaction energy is composed of three terms: one is a classic repulsive term, one is a constant which is not important, and another one is an attractive term caused by confinement. The slop of the third term gives the attractive force. The interaction is under constant charge condition.

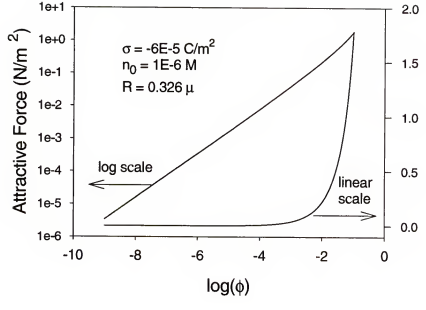

Figure 9-4. The Plot of attractive force as a function of confinement / solid loading. The attractive force increases drastically as the confinement/solid loading increases. The interaction is under constant charge condition.

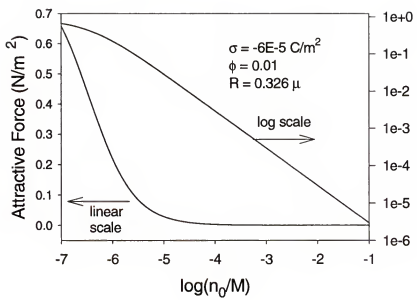

Figure 9-5. The plot of attractive force as a function of background electrolyte concentration. With the increase of background electrolyte concentration the attractive force decreases drastically. The interaction is under constant charge condition.

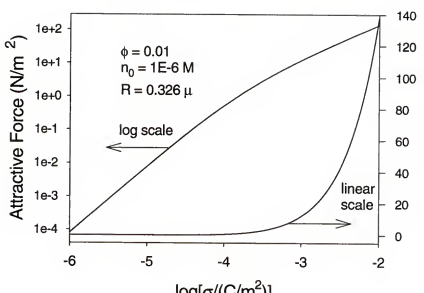

Figure 9-6. The plot of attractive force as a function of surface charge density. The increase of surface charge density will increase the attractive force. The interaction is under constant charge condition.

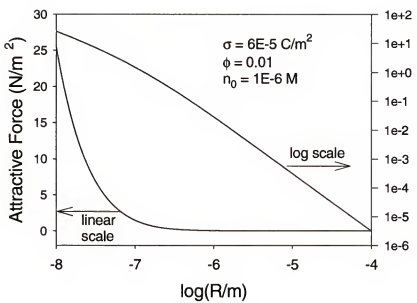

Figure 9-7. The plot of attractive force as a function of particle radius. Smaller particle will show more prominent attraction. This interaction is under constant charge condition.

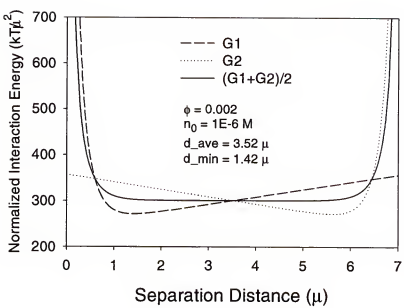

Figure 9-8. The plots of interaction energies as a function of removable surface position. The attractive forces are canceled and only repulsive interaction is left. The preferred location for the removable surface is thus in the middle. The interaction is under constant charge condition.

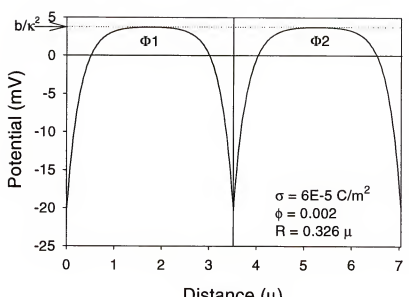

Figure 9-9. Potential distributions when the movable surface is at the middle of the system. Sign reversal of potential is seen in the solution. The integral of potential curve gives a zero value. The interaction is under constant charge condition.

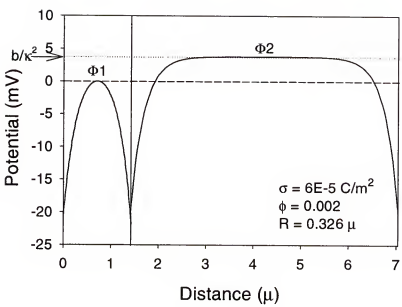

Figure 9-10. The plot of potential distributions in the system when the compartment 1 has its lowest energy. Correspondingly, the sign reversal of potential in the compartment 1 just vanishes. The integral of potential curve gives a zero value. The interaction is under constant charge condition.

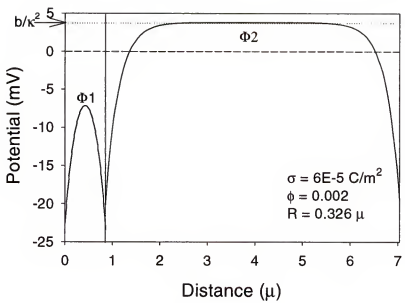

Figure 9-11. The plot of potential distributions in the system when the paired interaction in compartment 1 show pure repulsion. Correspondingly, the sign reversal of potential in compartment 1 is not seen. The integral of potential curve gives a zero value. The interaction is under constant charge condition.

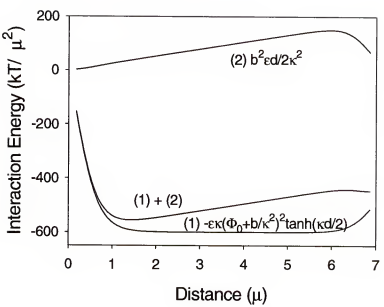

Figure 9-12. The plot of paired interaction energy as a function of separation distance under constant potential condition. The detailed discussion can be found in the text.

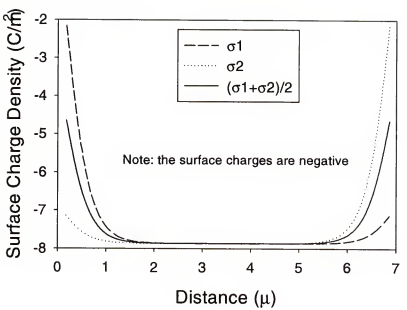

Figure 9-13. The plots of surface charge density changes as functions of the location of the removable plate.

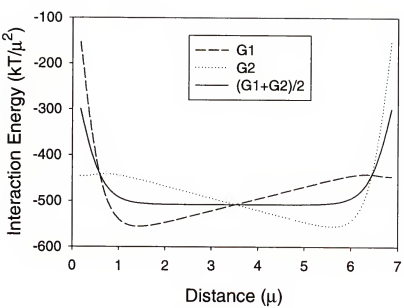

Figure 9-14. The plots of interaction energies as functions of the location of the removable surface under constant potential condition. The paired interactions show long-range attractive force, but they cancel with each other when considering the total energy of the system. Thus the preferred location for the removable surface is still in the middle.

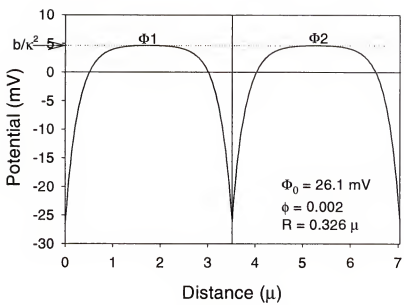

Figure 9-15. Potential distributions when the movable surface is at the middle of the system. Sign reversal of potential is seen in the solution. The integral of potential curve gives a zero value. The interaction is under constant potential condition.

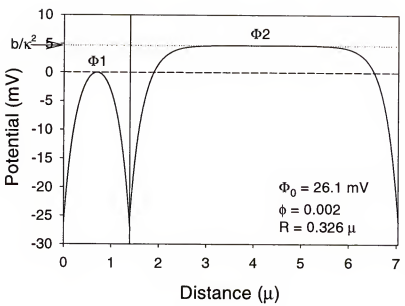

Figure 9-16. The plot of potential distributions in the system when the compartment 1 has its lowest energy. Correspondingly, the sign reversal of potential in the compartment 1 just vanishes. The integral of potential curve gives a zero value. The interaction is under constant potential condition.

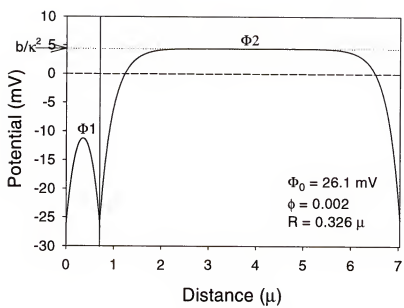

Figure 9-17. The plot of potential distributions in the system when the paired interaction in compartment 1 show pure repulsion. Correspondingly, the sign reversal of potential in compartment 1 is not seen. The integral of potential curve gives a zero value. The interaction is under constant potential condition.

CHAPTER 10
CONCLUSIONS AND FUTURE WORK

In Chapter 3 the mechanism and prevention of particle deposition onto silicon wafer surfaces from HF solutions were discussed. The pH value in 0.5 wt. % HF is 1.9 and in this solution the bare silicon surface is slightly positively charged. The particle deposition in the DHF cleaning is due to the large dispersion interaction between the silicon and the particles. Surfactants can be used to minimize particle deposition in DHF cleaning. The efficiency of a surfactant is correlated with its capability to increase the value of the product of silicon and particle zeta-potentials. This correlation can be understood with the linear superposition approximation during the calculation of electrical interaction between the silicon and the particles. This work can be served as the foundation of additive selection to minimize particle deposition in general. This experiment also proves that the linear superposition approximation is applicable in daily practice.

In Chapter 4, a detailed direct force measurement study on silicon-silicon nitride surface interactions with the atomic force microscope was presented. The two surfaces show strong attraction in air, and this attraction is electrostatic in nature. A very large adhesion force is also shown in air. It implies that bare silicon wafers are easily contaminated by silicon nitride-like particles in air. The force measurements in solution

generally showed reduced attraction and adhesion, suggesting that the particulate contaminants are easier to be removed in the solution than in the air. In other words, the wet cleaning is inherently better than the dry cleaning. In a pH 2 solution silicon nitride particles can be easily attracted by the silicon surface due to the van der Waals interaction and lack of the electrostatic repulsion. After the particles are attached on the silicon surface, they are not easily detached because of the existence of an adhesion force. The attaching/detaching process is not reversible.

When CTAB is present in the solution, the attractive force gradually changes to repulsive force and the adhesion force vanishes with the increase of CTAB concentration. CTAB concentration should be not less than 500 ppm in order to prevent silicon nitride particle contamination on silicon wafer surfaces. CTAB forms a monolayer film on a silicon surface even the bulk concentration is as low as 12.5 ppm. The film structure does not change significantly with the increase of CTAB bulk concentration. The repulsive forces have two origins: the steric repulsion from the surface film structure and the electrostatic force. The steric force alone does not effectively prevent a particle from depositing on the silicon surface. The simulation results of the DLVO forces show that the CTAB molecules not only increase the electrostatic repulsion, but also decrease the van der Waals interaction.

The anionic surfactant is very effective in modulating the silicon-silicon nitride surface interaction in a pH 2 solution. Although at very low concentration the anionic surfactant increases attractive and adhesion forces, it eliminates the adhesion force and changes the attraction force to repulsion force when the bulk concentration exceeds

50ppm. No surface film structure was observed. This may be due to the structure of this anionic surfactant: the head group is in the middle of the hydrophobic chain. The simulation suggests that the anionic molecules are adsorbed strongly on the surfaces and the van der Waals interaction is further reduced.

In the whole concentration range of interest the nonionic surfactant L12-8 does not help prevent particle deposition. The surfactant does not introduce any electrostatic repulsive force. After the concentration reaches CMC a monolayered surface structure forms on a silicon nitride surface. The film introduces steric repulsive force and decreases adhesion force, but the adhesion force is still present. Once the surface film is formed, it does not change significantly with the increase of surfactant bulk concentration. The film is stronger than that formed by CTAB.

In general, the silicon-silicon nitride system in a pH 2 solution with/without surfactant can be described by classic DLVO theory with the addition of steric forces. All the three conditions: constant charge, constant potential, and intermediate (LSA), can be encountered. An interesting finding is that as long as the attraction is decreased or the repulsion is increased at approaching direction, the adhesion at retracting direction is decreased. It suggests that the additive which decreases particle deposition also help particle removal.

Although silicon nitride particles represents most of the inorganic particulate contaminants in real fabrication environment, the study of organic particle-silicon surface interactions in HF solution is required in the future. Many researches have been done on polystyrene latex particle-silicon wafer interactions, however, a study with direct force

measurement methods to gain detailed interaction characteristics is still lack. Furthermore, the study of surfactant-polystyrene latex particle interactions could offer valuable information to reduce organic particle contamination on silicon surfaces in HF solutions.

The topic of Chapter 5 is to study the preferential deposition of copper onto silicon wafer surfaces from HF solutions. We showed in this microscopic study that the copper preferential deposition on silicon surfaces from HF solutions is caused by defect-enhanced nucleation. Copper was found to deposit only on defect sites which were artificially induced by surface scratching or ion bombardment. They serve the direct experimental proof of the hypothesis that defects will enhance copper contamination. Previous inconsistent results could be understood with the aid of this work. This work also suggests that in order to decrease copper contamination on silicon surfaces, the defect sites such as ion-implanted areas or polysilicon area should be more carefully protected.

A novel in situ technique to characterize copper outplating from HF solutions on to silicon surfaces was presented in Chapter 6. It measures the open circuit potential change of a silicon electrode in a HF solution as a function of copper concentration in the solution. The sensitivity is in ppb range and it has at lease three orders of magnitude dynamic range. This technique can also be used to characterize additive effects on copper outplating onto silicon surfaces. The experiments showed that more severe copper outplating occurs on n--type wafers than on p-type wafers, and that H_2O_2, HCl, and HNO_3 are all effective in alleviating Cu outplating. These results are in agreement with the

copper contamination results reported by other authors. The mechanism of OCP change is explained in detail by using mixed potential theory with taking copper catalyzed hydrogen evolution into consideration.

Surfactant effects on copper outplating onto silicon surfaces from HF solutions were studied in Chapter 7. It was found that certain cationic surfactant is effective in reducing copper outplating onto silicon surfaces during DHF cleaning. Anionic surfactants may increase metal outplating, not only copper but also other metals such as nickel, by forming complexes with metal ions. The complexes are then adsorbed onto silicon surfaces. Combining open circuit potential monitor and surface metal analysis, one can differentiate different mechanisms of copper outplating. The roles of surfactant on copper outplating are discussed in detail in the Chapter.

From the discussions in Chapters 5,6 and 7, it is clear that defect induced copper outplating is critical. The roles of additives play in reducing copper outplating are also better understood. The outplating of silver, gold or platinum should have similar characteristics as copper. However, the studies of the characteristics and the prevention of their outplating are still to be verified with experimental facts, although they are not major contaminant species in the real fabrication environment. More importantly, in the future the metal ions-surfactant interaction are urgently required to study, because the interaction could introduce a new type of contamination source in dilute HF cleaning.

In Chapter 8 a general solution for the semi-infinite planar Poisson-Boltzmann equation was discussed. It is an exact solution for symmetrical electrolyte and z-2z/2z-z electrolyte. It is also a very good approximation for z-3z/3z-z and 2z-3z/3z-2z electrolytes

with error no more than 1% or less. The evaluation is done by comparing with numerical results using Galerkin weighted residual finite element method. This numerical method can be easily expanded to any one-dimensional case with any electrolytes. The general solution can be served as a functional approximation for potential distribution in two interacting double layers when calculating electrostatic interaction energy.

Like-charge electrostatic attractions in confined colloidal systems were discussed in Chapter 9. In this Chapter we provided a simple confined one-dimensional planar symmetry model and the method to obtain paired and total energies for electrostatic interactions in a colloid system, from which we found that the classic DLVO electrostatic interaction energy formulations are just special cases of our more general ones. We found that the long range attractive force between two like-charged bodies does indeed exist. It results from the sign reversal of electric potential in the solution, which originates from the mass conservation. The predicted attractive force is influenced by the confinement, the background electrolyte concentration, the surface charge density/surface potential, and the particle size. However, the total interaction energy of the system shows a minimum only at average separation of each plates due to the cancellation of the attractive components. Future studies on nonlinearized Poisson-Boltzmann equation and/or higher dimensional interactions by numerical methods are highly needed to simulate the order/disorder structure in colloid system. Nevertheless, our model reveals the unique characteristics of confined/concentrated system for the first time since the establishment of Gouy-Chapman diffuse layer theory one century ago and the establishment of DLVO theory half century ago.

APPENDIX
NOVEL METHOD TO FORM A POROUS SILICON LAYER AND ITS APPLICATION ON COPPER SENSING

Porous silicon is a promising material with versatile potential applications in electronic isolation [Una78, Kon82, Yon87], heteroepitaxy [Kao87], metallization [Her85], micromachining [Tsa87], optoelectronic devices [Can90, Ric91, Hal91, Koy91, Kos92], and sensors [Smi86, And90]. Porous silicon is formed by the electrochemical anodization of a silicon wafer [Uhl56, Tur58]. Depending on the doping type, doping level, and anodization conditions, the porous silicon can have different morphology with the pore size ranging from several nanometers to tens of microns [Sea92a]. The common electrolyte bath for anodizing silicon is in a concentrated HF and ethanol mixture. The current density is about 20 $\mu A/cm^2$. During porous layer formation hydrogen gas is formed on the silicon electrode [Sea92a]. It has been reported that significant gas generation occured at the anodized surface of the silicon electrode, which needed to be prevented to form a porous silicon layer [Una97]. Gas formation and high concentration of HF involved are two potential issues if porous silicon is commercialized.

We found that by using dilute HF with small amount of surfactant the above-mentioned problems can be successfully solved. The experimental setup was the same as what has been reported in Chapter 6. The electrolyte solutions were 50 ml 0.5% HF aqueous solutions with or without a surfactant. During anodization the potential was kept

constant. The current densities were around 100 nA. The reaction time was 10 hours. Two-inch n-type and p-type Si(100) wafers with 1-10 Ohm·cm resistivity were studied. For n-type wafers, the effect of illumination on pore formation was also studied.

In Figure A-1 shows SEM micrographs of the anodized n-type silicon surfaces without the addition of the surfactant. The surface morphology is not uniform. The SEM micrograph in Figure A-1a shows that the surface is roughened but no pores are formed. During the reaction significant gas formation occurred on the silicon electrode. The gas bubble marks can be seen on the SEM micrograph in Figure A-1b. The reaction was done under the normal room light. However, if a surfactant was used, the gas bubbles were not observed on the silicon electrode surface. After 10 hour anodizing under similar conditions, the whole surface of the 2-in wafer became black. The SEM micrographs of an anodized n-type silicon surface with the addition of a surfactant are shown in Figure A-2. The effect of the surfactant is clear; it promotes pore formation. The porosity analyzed by an image soft ware on Figure A-2a is about 80%. The high magnification micrograph in Figure A-2b shows that the pore sizes are in the range of 3 - 5 microns. The cross section view in Figure A-2c shows that the porous layer is about 20 micron thick.

The surfactant also promoted pore formation on p-type wafers. The SEM micrographs of a p-type wafer surface after 10 hour anodizing in the same electrolyte solution are shown in Figure A-3. The low magnification micrograph in Figure A-3a suggests that pores are uniformly formed on the surface. The pore sizes are ~ 10 microns, as shown in Figure A-3b.

For n-type silicon the applied potential is dropped predominantly across the space-charge region on the silicon side [Gas89] and the characteristic pore morphology has been explained in terms of a tunneling mechanism involving electron injection at the pore base due to field concentration [Sea92b]. Therefore, it is deduced that the illumination will influence pore morphology on n-type silicon. The experimental results in dark and under 25 W incandescent lamp illumination are presented in Figures A-4 and A-5, respectively. They show that, together with the micrographs in Figure A-2 under normal light, the illumination decreases the average thickness of the pore walls. Therefore, it increases porosity of the porous layer.

From the above discussion we can see that the surfactant can promote pore formation. There are two possible explainations. One is that it eliminates gas bubble nucleation and growth on the silicon surface, allowing the reaction to take place uniformly on the entire electrode surface. The other is that it is adsorbed on the silicon surface, causing charging on the silicon surface. Thus, the space-charge region is changed. It also reveals that by adopting a different ionic surfactant, one can modify the space-charge region, thus modify the pore morphology. The electrochemical conditions such as voltage, current and reaction time are not optimized in this preliminary study. Nevertheless, this study provides the initial investigation on using very dilute HF solution to produce a satisfactory porous silicon layer over large areas. In this study, the macropore formation on an entire 2-in wafer surface under very mild chemical conditions was achieved.

The porous silicon can also be used to detect copper contamination in HF baths. The setup was described in Chapter 6. By forming a porous layer on the silicon electrode, the sensitivity of the electrode to copper contamination increases significantly, as shown in Figure A-6. The slope of the OCP change versus bulk copper concentration increases from 46.1 mV to 87.4 mV. This phenomenon can be understood by the mechanism of defect-enhanced copper outplating, which has been discussed in detail in Chapter 5. It is very promising to use porous silicon to detect copper contamination in HF solutions.

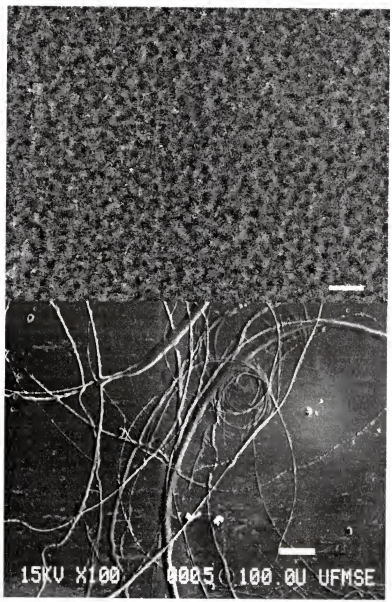

Figure A-1. SEM micrograph of an anodized silicon surface. The electrolyte was 0.5% HF without any surfactant. Current density was about 100 nA/cm^2. 10 hour reaction under normal light. The electrode was 2-in n-type Si(100) with 1-10 Ohm·cm resistivity. The surface morphology is not uniform. (a, top) Surface roughening of the silicon wafer. The surface was roughened but pores are not formed. The scale bar is 10 micron. (b, bottom) Lower magnification view of a silicon surface after the same anodization. Bubble marks are clearly shown.

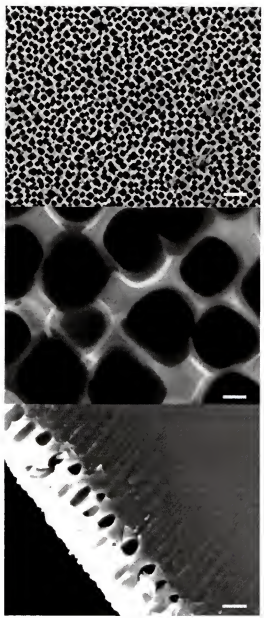

Figure A-2. SEM micrographs of an anodized silicon surface. The electrolyte was 0.5% HF + 1% surfactant. Current density was about 100 nA/cm^2. 10 hour reaction under normal light. The electrode was 2-in n-type Si(100) with 1-10 Ohm·cm resistivity. A 20 micron thick porous layer was formed with the pore size 3 - 5 micron. (a, top) Low magnification plane view. The scale bar is 10 micron. (b, middle) High magnification plane view. The scale bar is 1 micron. (c, bottom) Cross-section view. The scale bar is 5 micron.

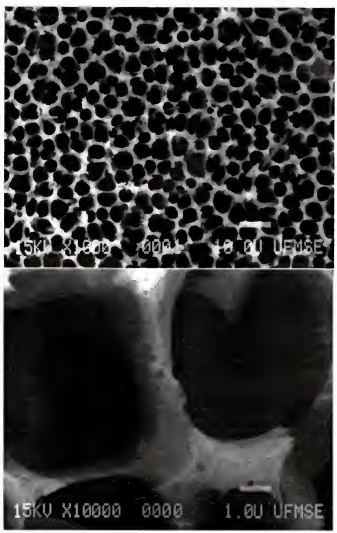

Figure A-3. SEM micrographs of an anodized silicon surface. The electrolyte was 0.5% HF + 1% surfactant. Current density was about 100 nA/cm^2. 10 hour reaction under normal light. The electrode was 2-in p-type Si(100) with 1-10 Ohm·cm resistivity. A porous layer was formed with the pore size ~ 10 micron. (a, top) Low magnification plane view. The scale bar is 10 micron. (b, bottom) High magnification plane view. The scale bar is 1 micron.

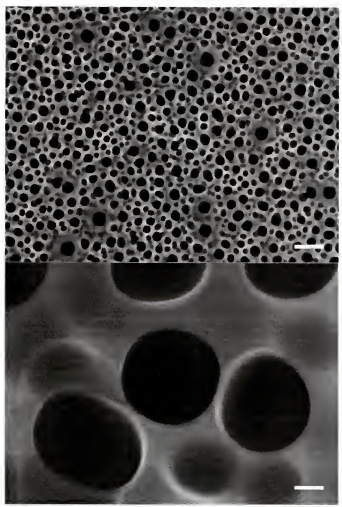

Figure A-4. SEM micrographs of an anodized silicon surface. The electrolyte was 0.5% HF + 1% surfactant. Current density was about 100 nA/cm^2. 10 hour reaction in dark The electrode was 2-in n-type Si(100) with 1-10 Ohm·cm resistivity. The average thickness of the pore walls is larger than that in Figure A-4, which was produced under normal laboratory light. (a, top) Low magnification plane view. The scale bar is 10 micron. (b, bottom) High magnification plane view. The scale bar is 1 micron. The pore sizes are ~ 3 microns.

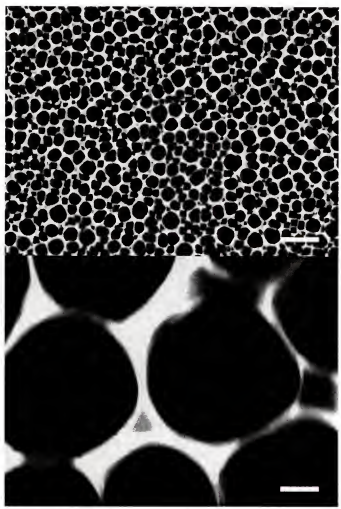

Figure A-5. SEM micrographs of an anodized silicon surface. The electrolyte was 0.5% HF + 1% surfactant. Current density was about 100 nA/cm^2. 10 hour reaction under 25W incandescent lamp illumination. The electrode was 2-in n-type Si(100) with 1-10 Ohm·cm resistivity. The average thickness of the pore walls is smaller than that in Figure A-4, which was produced under normal laboratory light. (a, top) Low magnification plane view. The scale bar is 10 micron. (b, bottom) High magnification plane view. The scale bar is 1 micron. The pore sizes are 3 - 5 microns.

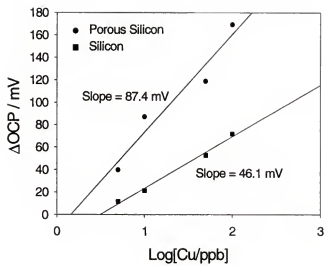

Figure A-6. Plots of silicon electrode OCP change in HF solution as a function of bulk copper concentration. The electrode with a porous silicon layer has a significantly higher slope than that of the electrode without porous silicon layer, indicating that porous silicon is more sensitive to detect copper contamination in HF solutions.

REFERENCES

And90 R. Anderson, R. Muller, and C. Tobias, *Sensors and Actuators A*, **23**, 835 (1990).

Aom93 H. Aomi, F. Derouin, and T. Ohmi, *Extended Abstract of Electrochemical Society*, **93-1**, 1144 (1993).

Bar72 D. Bargeman, F. Van Voorst Vader, *J. Electroanal. Chem. Interfacial Electrochem.*, **37**, 45 (1972).

Bec90 R. S. Becker, G. S. Higashi, Y. J. Chabal and A. J. Becker, *Phys. Rev. Lett.*, **65**, 1917 (1990).

Bed93 S. Bedge, B. S. Barron, and H. H. Lamb, *Mat. Res. Soc. Symp. Proc.*, **315**, 467 (1993).

Bin86 G. Binnig, C. Quate, and C. Gerber, *Phys. Rev. Lett.*, **56**, 930 (1986).

Bjo95 C. H. Bjorkman, H. Nishimura, T. Yamazaky, J. L. Alay, M. Fukuda, and M. Hirose, *Mat. Res. Soc. Proc.*, **386**, 177 (1995).

Blo82 H. N. Blount, *J. Phys. Chem.*, 86, 2632 (1982).

Bow98 W. Bowen and A. Sharif, *Nature*, **393**, 663 (1998).

Bur88 V. A. Burrows, Y. J. Chabal, G. S. Higashi, K. Raghavachari, and S. B. Christman, *Appl. Phys. Lett.*, **53**, 998 (1988).

But91 H. Butt, *Biophys. J.*, **60**, 1438 (1991).

But95a H. Butt and M. Jaschke, *Nanotechnology*, **6** (1995).

But95b H. Butt, M. Jaschke, and W. Ducker, *Bioelectrochemistry and bioenergetics*, **38**, 191 (1995).

Cac92 H. Cachet, M. Froment, E. Souteyrand and C. Dening, *J. Electrochem. Soc.*, **139**, 2920 (1992).

Can90 L. Canham, *Appl. Phys. Lett.*, **57**, 1046 (1990).

Cha13 Chapman, *Phil. Mag.*, **25**, 475 (1913).

Cha86 Y. J. Chabal, *Surf. Sci.*, **168**, 594 (1986).

Cha88 Y. J. Chabal, G. S. Higashi, K. Raghavachari, and V. A. Burrows, *J. Vac. Sci. Technol.*, **A7**, 2104 (1988).

Che98 X. Cheng, G. Li, E. Kneer, B. Vermeire, H. Parks, S. Raghavan, and J. Jeon, *J. Electrochem. Soc.*, **145**, 352 (1998).

Chu97 B. C. Chung, G. A. Marshall, C. W. Pearce, and K. P. Yanders, *J. Electrochem. Soc.* **144**, 652 (1997).

Chy96a O. M. R. Chyan, J. J. Chen, H. Y. Chien, L. Hall, and J. Sees, *J. Electrochem. Soc.* 143, 92 (1996).

Chy96b O. M. R. Chyan, J. Chen, H. Chien, J. Wu, M. Liu, J. A. Sees and L. Hall, *J. Electrochem. Soc.*,**143**, L235 (1996).

Crc97 *CRC Handbook of Chemistry and Physics*, D. Lide Editor-in-Chief, CRC press, New York (1997).

Cro94 J. Crocker and D. Grier, *Phys. Rev. Lett.*, **73**, 352 (1994).

Cro96 J. Crocker and D. Grier, *Phys. Rev. Lett.*, **77**, 1897 (1996).

Der75 B.V. Derjaguin, V. M. Muller, and Y. P. Toporov, *J. Colloid Interface Sci.*, **53**, 314 (1975).

Der87 B. V. Derjaguin, N. V. Churaev, and V. M. Muller, *Surface Forces*, Ch2, Ch4, Ch6, Ch8, Consultants Bureau, New York (1987).

Der93 F. Derouin, H. Aomi, and T. Ohmi, *Proc. 39th Meeting of Institute of Environmental Sciences*, **1**, 460 (1993).

Don93 R. P. Donovan, T. Yamamoto, and R. Periasamy, *Mat. Res. Symp. Proc.*, **315**, 3 (1993).

Dru94 C. Drummond, and T. Senden, *Colloids and Surfaces A*, **87**, 217 (1994).

Duc91 W. Ducker, T. Senden, and R. Pashley, *Nature*, **353**, 239 (1991).

Duc97 W. Ducker, E. Luther, D. Clarke, and F. Lange, *J. Am. Ceram. Soc.*, **80**, 575 (1997).

Dum91 P. Dumas and Y. J. Chabal, *Chem. Phys. Lett.*, **181**, 537 (1991).

Dum92 P. Dumas, Y. J. Chabal and P. Jakob, *Surf. Sci.*, **269**, 867 (1992).

Dur93 J. Drucker, A. Bandari and A. Burrows, *Mat. Res. Soc. Symp. Proc.*, **315**, 479 (1993).

Eva85 D. F. Evans and M. W. Upton, *J. Chem. Soc. Dalton Trans.,* 2525 (1985).

Gar92 B. Garrido, J. Samitier, J. R. Morante, L. Fonseca, and F. Campabadal, *Appl. Surf. Sci.*, **56-58**, 861 (1992).

Gas89 F.Gaspard, A. Bsiesy, M. Ligeon, F. Muller, and R. Herino, *J. Electrochem. Soc.*, **136**, 3043 (1989).

Gou09 G. Gouy, *Compt. Rend.*, **149**, 654 (1909).

Gou10 Gouy, *J. Phys. Theor. Appl.*, **9**, 457 (1910).

Gra53 D. C. Grahame, *J. Chem. Phys.*, **21**, 1054 (1953).

Gra90 D. Graf, M. Grundner, R. Schulz, and L. Muhlhoff, *J. Appl. Phys.*, **68**, 5155 (1990).

Gra91 D. Graf, M. Grundner, L. Muhlhoff, and M. Dellith, *J. Appl. Phys.*, **69**, 7620 (1991).

Gra95 L. Graff, *Metal Impurities in Silicon-Device Fabrication*, Springer, New York, 65 (1995).

Gre81 John Gregory, *J. Colloid Interface Sci.*, **83**, 138 (1981).

Gru86 M. Grundner and H. Jacob, *Appl. Phys.*, **A39**, 73 (1986).

Hal91 A. Halimaoui, C. Oules, G. Bomchil, A. Bsiesy, F. Gaspard, R. Herino, M. Ligeon, and F. Muller, *Appl. Phys. Lett.*, **59**, 304 (1991).

Ham37 H. C. Hamaker, *Physica (Utrecht)* **4**, 1058 (1937).

Has95a Hashimoto Chemical Corporation, *Technical materials: New Wet Cleaning Process* (1995).

Has95b Hashimoto Chemical Corporation, *Technical Materials: LLHF - HF with surfactant* (1995).

Hat94 T. Hattori, *Contamination Control and Defect Reduction in Semiconductor Manufacturing III*, the Electrochemical Society, Pennington, 3 (1994).

Hat98 T. Hattori in *Ultraclean Surface Processing of Silicon Wafers*, ed. T. Hattori, Springer, 3 (1998).

Hay95 Y. Hayami, M. T. Suzuki, H. Ogawa, and S. Fujimura, *Mat. Res. Soc. Symp. Proc.*, 386, 69 (1995).

Hen99 R. Henry, *R&D Magazine*, 6LS, January (1999).

Her81 H. Hertz, *J. Reine Angew. Math.*, **92**, 156 (1881).

Her85 R.Herino, P. Jan, and G. Bomchil, *J. Electrochem. Soc.*, **132**, 2513 (1985).

Hes91 H. E. Hessel, A. Feltz, M. Reiter, U. Memmert, and R. J. Behm, *Chem. Phys. Lett.*, **186**, 275 (1991).

Hey93 M. M. Heyns, S. Verhaverbeke, M. Meuris, P. W. Mertens, H. Schmidt, M. Kubota, A. Philipossian, K. Dillenbeck, D. Graf, A. Schnegg and R. de Blank, *Mat. Res. Soc. Symp. Proc.,* **315**, 35 (1993).

Hoc89 R. S. Hockett, *Surface and Interface Analysis of Microelectronic Materials Processing and Growth*, **1186**, 10, SPIE (1989).

Hog66 R. Hogg, T. W. Healy and D. W. Fuerstenau, *Trans. Faraday Soc.*, **62**, 1638 (1966).

Hou80 D. B. Hough and L. R. White, *Adv. Colloid Interface Sci.*, **14**, 3 (1980).

Hou89 M. Hourai, K. Murakami, T. Shigematsu, N. Fujino and Shiraiwa, *J. Appl. Phys.*, **28**, 2413 (1989).

Hsu92 E. Hsu, H. Parks, R. Craigin, S. Tomooka, J. Ramberg, and R. Lowry, *J. Electrochem. Soc.*, 139, 3659 (1992).

Hun93 R.J. Hunter, *Introduction to Modern Colloid Science*, Oxford University Press, Oxford, p.208 (1993).

ISe83 N. Ise, T. Okubo, M.Sugimura, K. Ito, and H. J. Nolte, *J. Chem. Phys.*, **78**, 536 (1983).

Isr92 J. Israelachvili, *Intermolecular & Surface Forces*, 2nd ed., Academic Press, London, (1992).

Ita90 M. Itano, F. W. Kern, Jr., I. Kawanabe, M. Miyashita, R. W. Rosenberg, and T. Ohmi, *Proceeding of 8th Workshop on Ultraclean Technology*, Tokyo, 35 (1990).

Ita92 M. Itano, F. W. Kern, Jr., I. Kawanabe, M. Miyashita, R. W. Rosenberg, and T. Ohmi, *IEEE Transactions on Semiconductor Manufacturing* **5**, 114 (1992).

Ita93 M. Itano, F. W. Kern, Jr., M. Miyashita, and T. Ohmi, *IEEE Transactions on Semiconductor Manufacturing*, **6**, 258 (1993).

Ita95 M. Itano, T. Kezuka, M. Ishii, T. Unemoto, M. Kubo, and T. Ohmi, *J. Electrochem. Soc.* **142**, 971 (1995).

Ita96 M. Itano, T. Kezuka, M. Kubo and T. Ohmi, *Proc. Semiconductor Pure Water and Chemicals Conference, Santa Clara, CA*, 257 (1996).

Ita98 M. Itano and T. Kezuka in Ultraclean *Surface Processing of Silicon Wafers*, ed. T. Hattori, Springer, New York, 115 (1998).

Itay92 K. Itaya, R. Sugawara, Y. Morita and Tokumoto, *Appl. Phys. Lett.*, **60**, 2534 (1992).

Itay95 K. Itaya, S. Yau, and K. Kaji, *Mat. Res. Soc. Symp. Proc.*, **386**, 365 (1995).

Ito94 K. Ito, H. Yoshida, and N. Ise, *Sicence*, **263**, 66 (1994).

Iup82 IUPAC, *Stability Constants of Metal Ion Complexes, Part A*, Pergamon Press, Oxford, 188 (1982).

Jac91 P. Jacob and Y. J. Chabal, *J. Chem. Phys.*, **95**, 2897 (1991).

Jeo96 Jeon, S. Raghavan, H. Parks, J. Lowell, and I. Ali, *J. Electrochem. Soc.*, **143**, 1996 (2870)

Joh71 K. Johnson, K. Kendall, and A. Roberts, *Proc. R. Soc. London A*, **324**, 301 (1971).

Kao87 Y. Kao, K. Wang, B. Wu, and G. Bai, *Appl. Phys. Lett.*, **51**,1809 (1987).

Kaw89 Y. Kawazawa and T. Tatsuno, *Extended Abstract, the 50th Autumn Meeting of the Japan Society of Applied Physics,* 27P-B-15 (1989).

Kek93 P. Kekicheff, S. Marcelija, T. Senden, and V. Shubin, *J. Chem. Phys.*, **99**, 15 (1993).

Kep94 G. Kepler and S. Fraden, *Phys. Rev. Lett.*, **73**, 356 (1994).

Ker70 W. Kern and D. A. Puotinen, *RCA Rev.* **31**, 187 (1970).

Ker90 F. W. Kern, Jr., M. Itano, I. Kawanabe, M. Miyashita, R. W. Rosenberg, and T. Ohmi, *Proceedings of Advanced Wet Chemical Processing II*, 113, Ultra Clean Society, Tokyo (1990).

Ker91 F. W. Kern Jr., M. Itano, I. Kawanabe, M. Miyashita, and T. Ohmi, *Proc. 11th Workshop on ULSI Ultra Clean Technology*, Tokyo, 23 (1991).

Kir34 J. G. Kirkwood, *J. Chem. Phys.*, **2**, 767 (1934).

Kik90 H. Kikuyama, N. Miki, K. Saga, J. Takano, I. Kawanabe, M. Miyashita and T. Ohmi, *IEEE Trans. Semiconductor Manufacturing*, **3**, 99 (1990).

Kim91 Y. Kim and C. M. Lieber, *J. Am. Chem. Soc.*, **113**, 2335 (1991).

Kon82 S. Konaka, M. Tabe, and T. Sakai, *Appl. Phys. Lett.*, **41**, 86 (1982).

Kos73 A. Kose, M. Ozaki, K. Takano, Y. Kobayashi, and S. Hachisu, *J. Colloid Interface Sci.*, **44**, 330 (1973).

Kos92 N. Koshida and H. Koyama, *Appl. Phys. Lett.*, **60**, 347 (1992).

Koy91 H. Koyama and N. Koshida, *J. Electrochem. Soc.*, **138**, 254 (1991).

Lev51 S. Levine and A. Suddaby, *Proc. Phys. Soc.* (London), **A 64**, 287, 431 (1951).

Lev69 S. Levine and J. E. Jones, *Kolloid. Z.*, **230**, 306 (1969).

Lev90 R de Levie, *J. Electroanal. Chem.*, **278**, 17 (1990).

Lar97 A. Larsen and D. Grier, *Nature*, **385**, 230 (1997).

Li98 G. Li, E. Kneer, B. Vermeire, H. Parks, S. Raghavan, and J. Jeon, *J. Electrochem. Soc.*, **145**, 241 (1998).

Lin93 X. Lin, F. Creuzet, and H. Arribart, *J. Phys. Chem.*, **97**, 7272 (1993).

Lju93 K. Ljungberg, Y. Backlund and A. Soderbarg, *Proceedings of the 3rd International Symposium on Cleaning Technology in Semiconductor Device Manufacturing*, New Orleans, LA, 222 (1993).

Luk63 W. Luck, M. Klier, and H. Wesslau, Ber Bunseges. *Phys. Chem.*, **67**, 75 (1963).

Man94 S. Manne, J. Cleveland, H. Gaub., G. Stucky, and P. Hansma, *Langmuir*, **10**, 4409 (1994).

Mar87 Y. Martin, C. Williams, and H. Wickramasinghe, *J. Appl. Phys.*, **61**, 4723 (1987).

Mat89 C. Mate, M. Lorenz, and V. Novotny, *J. Chem. Phys.*, **90**, 7550 (1989).

Meu95 M. Meuris, P. W. Mertens, A. Opdebeeck, H. F. Schmidt, M. Depas, G. Vereecke,M. M. Heyns and A. Philipossian, *Solid State Technology*, 109, July (1995).

Miy92 M. Miyashita, T. Tsuga, K. Makihara, and T. Ohmi, *J. Electrochem. Soc.*, **139**, 2133 (1992).

Miy94 M. Miyamoto, N. Kita, S. Ishida, and T. Tatsuno, *J. Electrochem. Soc.*, **141**, 2899 (1994).

Mor89 M. Morita, T. Ohmi, E. Hasegawa, M. Kawakami, and Suma, *Appl. Phys. Lett.*, **55**, 562 (1989).

Mor94 H. Morinaga, M. Suyama, and T. Ohmi, *J. Electrochem. Soc.*, **141**, 2834 (1994).

Muk71 P. Mukerjee and K. Mysels, *Critical Micelle Concentration of Aqueous Surfactant Systems -- National Standard Reference data Systems NSRDS-NBS 36*, Secretary of Commerce on Behalf of the United States Government, p. 106 (1971).

Nag95 Z. Nagy, J. P. Blaudeau, N. C. Hung, L. A. Curtiss and D. J. Zurawski, *J. Electrochem. Soc.*, **142**, L87 (1995).

Neu99 J. Neu, *Phys. Rev. Lett.*, **82**, 1072 (1999).

Nor97 G. Norga, M. Platero, K. Black, A. Reddy, J. Michel, and C. Kimerling, *J. Electrochem. Soc.*, **144**, 2801 (1997).

Obe94 Y. S. Obeng, *Proceedings of the Semiconductor Pure Water and Chemicals Conference*, San Jose, CA, 110 (1994).

Ohm91 T. Ohmi, M. Miyashita, and T. Imaoka, *Microcontamination Conference Proceedings*, 491 (1991).

Ohm91b T. Ohmi, K. Kotani, A. teramoto, and M. Miyashita, *IEEE Electron Device Lett.*, **12**, 652 (1991).

Ohm92 T. Ohmi, M. Miyashita, M. Itano, T. Imaoka, and I. Kawanabe, *IEEE Trans. Electron Devices*, **39**, 537 (1992).

Ohm92b T. Ohmi, T. Imaoka, I. Sugiyama, and T. Kezuka, *J. Electrochem. Soc.*, **139**, 3317 (1992).

Ohm93a T. Ohmi, *Proceedings of the 3rd International Symposium on Cleaning Technology in Semiconductor Devices Manufacturing*, New Orleans, LA, 3 (1993).

Ohm93b T. Ohmi, T. Imaoka, T. Kezuka, J. Takano, and M. Kogure, *J. Electrochem. Soc.*, **140**, 811 (1993).

Ohm94 T. Ohmi, in *Proceedings of the Third International Symposium on Cleaning Technology in Semiconductor Device Manufacturing*, Electrochemical Society, Pennington, p.3 (1994).

Ons33 L. Onsager, *Chem. Rev.*, **13**, 73 (1933).

Osh92 S. O'Shea, M. Welland, and T. Rayment, *Appl. Phy. Lett.*, **60**, 2356 (1992).

Ouy88 J. Ouyang, and J. Bard, *Bull. Chem. Soc. Jpn.*, **61**, 17 (1988).

Pal94 T. Palberg and M. Wurth, *Phys. Rev. Lett.*, **72**, 786 (1994).

Pas88 R. Pashley, P. McGuiggan, R. Horn, and B. Ninham, *J. Colloid Interface Sci.*, **126**, 578 (1988).

Ple90 D. Pletcher and F. Walsh, *Industrial Electrochemistry*, Chapter 1, Chapman and Hall, New York (1990).

Pra95 C. Prater, P. Maivald, K. Kjoller, and M. Heaton, *Probing Nano-scale Forces with the Atomic Force Microscpoe*, application notes, Digital Instruments (1995).

Pro88 J. L. Prom, J. Castagne, G. Sarrabayrouse, and A. Munoz-Yague, *IEE Proc., Part I*, **135**, 20 (1988).

Pro91 J. L. Prom, P.Morfouli, K. Kassmi, G. Pananakakis, and G. Sarrabayrouse, *IEE Proc., Part G*, **138**, 321 (1991).

Rea92 Realize Inc., *Technical materials: Breakthrough for scientific semiconductor manufacturing in 2001*(1992).

Red93 J. N. Reddy, *An Introduction to the Finite Element Method*, McGraw-Hill, Boston(1993).

Ric91 A. Richter, P. Steiner, F. Kozlowski, and W. Lang. *IEEE Electron. Dev. Lett.*, **EDL-12**, 691 (1991).

Ril93a D. J. Riley and R. G. Carbonel, *J. Colloid Interface Sci.* **158**, 259 (1993).

Ril93b D. J. Riley and R. G. Carbonel, *J. Colloid Interface Sci.* **158**, 274 (1993).

Ros88 S. Ross and I. D. Morrison, *Colloidal Systems and Interfaces*, John Wiley & Sons, New York (1988).

Rot95 A. L. P. Rotondaro, T. Q. Hurd, H. F. Schmidt, I. Teerlinck, M. M. Hetns and C. Claeys, *Mat. Res. Soc. Symp. Proc.*, **386**, 183 (1995).

Rus89 W. B. Russel, D. A. Saville and W. R. Schowalter, *Colloidal Dispersions*, p.102, Cambridge University Press, Cambridge(1989).

Sad93 J. Sader and L. White, *J. Appl. Phys.*, **74**, 1 (1993).

Sad99 J. Sader and D. Chan, *J. Colloid Interface Sci.*, **213**, 268 (1999).

Sai89 A. Saito, K. Ohta, H.Itoh and H. Oka, *Extended Abstracts of the 21st Conference on Solid State Devices and Manufacturing*, Tokyo, 409 (1989).

Sai93 A. Saito, K. Ohta, H.Itoh and H. Oka, *Proceedings of the 3rd International Symposium on Cleaning Technology in Semiconductor Devices Manufacturing*, New Orleans, LA, 427 (1993).

Sch93 H. F. Schmidt, M. Meuris, P. W. Mertens, S. Verhaverbeke, M. M. Heyns, L. Hellemans, J. Snauwaert, and K. Dillenbeck, *Proceedings of the 3rd International Symposium on Cleaning Technology in Semiconductor Device Manufacturing*, New Orleans, LA, 102 (1993).

Sea92a P. Searson, J. Macaulay, and S. Prokes, *J. Electrochem. Soc.*, **139**, 3373 (1992).

Sea92b P. Searson, J. Macaulay, and F. Ross, *J. Appl. Phys.*, **72**, 253 (1992).

Sen94 T. Senden and W. Ducker, *Langmuir*, **10**, 1003 (1994).

Sen95 T. Senden, and C. Drunnond, *Colloids and Surfaces A*, **94**, 29 (1995).

Sha90 K. A. Sharp and B. Honig, *J. Phys. Chem.*, **94**, 7684 (1990).

Shi91 T. Shimono and M. Tsuji, *Extended Abstracts of the Electrochemical Society*, **91-1**, 278 (1991).

Shi93 T. Shimono and K. Yamamoto, *Mat. Res. Soc. Symp. Proc.*, **315**, 327 (1993).

Smi86 R. Smith and S. Collins, *IEEE Trans. Biomed. Eng.*, **BME-33**, 83 (1986).

Spi74 L. A. Spielman and S. K. Friedlander, *J. Colloid Interface Sci.*, **46**, 22 (1974).

Sze81 S. Sze, *Physics of Semiconductor Devices*, p.50, Wiley Interscience, New York(1981).

Tab77 D. Tabor, *J. Colloid Interface Sci.*, **58**, 2 (1977).

Tak98 M. Takiyama, in *Ultraclean Surface Processing of Silicon Wafers*, ed. T. Hattori, Springer, 42 (1998).

Tat92 B. Tata, M. Rajalakshmi, and A. Arora, *Phys. Rev. Lett.*, **69**, 3778 (1992).

Tat94 B. Tata and A. Arora, *Phys. Rev. Lett.*, **72**, 787 (1994).

Tar95 B. Tata and A. Arora, *Phys. Rev. Lett.*, **75**, 3200 (1995).

Tee95 I. Teerlink, H.F. Schmidt, A. L. P. Potondaro, T. Q. Hurd, P. W. Mertens, M. Meuris and M. M. Heyns, *Extended Abstracts of the Electrochemical Society*, **95-2**, 745 (1995).

Tee96a I. Teelinck, P. W. Mertens, H. F. Schmidt, M. Meuris, and M. M. Heyns, *J. Electrochem. Soc.*, **143**, 3323 (1996).

Tee96b I. Teelinck, P. W. Mertens, M. Meuris, and M. M. Heyns, *Symposium on VLSI Technology Digest of Technical Papers*, 206 (1996).

Tee96c I. Teelinck, P. W. Mertens, M. Meuris, and M. M. Heyns, *Proceeding of the 3rd International Symposium on Ultra Clean Processing of Silicon Surface*, 21 (1996).

Tho89 J. M. C. Thornton and R. H. Williams, *Semicond. Sci. Thechol.*, **4**, 847 (1989).

Tor95 L. Torcheux, A. Mayeux, and M. Chemla, *J. Electrochem. Soc.*, **142**, 2037 (1995).

Tsa87 S. Tsao, D. Myers, T. Guilinger, and M. Kelly, *J. Appl. Phys.*, **62**, 4182 (1987).

Tur58 D. Turner, *J. Electrochem. Soc.*, **105**, 402 (1958).

Tus97 Tushar Dhayagude, Weidong Chen, and Mohsen Shenasa, *Mat. Res. Soc. Symp. Proc.*, **477**, 217 (1997).

Uem95 K. Uemura and K. Shimanoe, *Extended Abstracts of the Electrochemical Society*, **95-2**, 747 (1995).

Uhl56 A. Uhlir, *Bell System Tech. J.*, **35**, 333 (1956).

Una78 T. Unagami and N. Seki, *J. Electrochem. Soc.*, **125**, 1340 (1978).

Una97 T. Unagami, *J. Electrochem. Soc.*, **144**, 1835 (1997).

Ver48 E. J. W. Verwey and J. TH. G. Overbeek, *Theory of the Stability of Lyophobic Colloids*, Elsevier (1948).

Ver92 S. Verhaverbeke, J. Alay, P. Mertens, M. Heyns, W. Vandervorst, M. Murrell, and C. Sofield, *Mat. Res. Soc. Proc.,* **259**, 391 (1992).

Ver93 S. Verhaverbeke, M. Meuris, H. Schimdt, P. Mertens, and M. Heyns, *Proceedings of the 3rd International Symposium on Cleaning Technology in Semiconductor Device Manufacturing*, New Orleans, LA, 176 (1993).

Vis72 J. Visser, *Adv. Colloid Interface Sci.*, **3**, 331 (1972).

Vos98 R. Vos, I. Cornelissen, M. Lus, P. Mertens, M. Meuris and M. Heyns, to be published.

War71 L. J. Warren, *Anal. Chim. Acta*, **53**,199 (1971).

Wei76 H. Weisz, S. Pantel and W. Meiners, *Analytica Chimica Acta*, **82**, 145 (1976).

Wei89 A. Weisenhorn, P. Hansma, T. Albrecht, and C. Quate, *Appl. Phys. Lett.*, **54**, 2651 (1989).

Wei92 A. Weisenhorn, P. Maivald, H. Butt, and P. Hansma, *Phys. Rev. B*, **45**, 11226 (1992).

Who58 P. Whorisky, *J. Appl. Phys.*, **29**, 867 (1958).

Yab86 E. Tablonovitch, D. L. Allara, C. C. Chang, T. Gmitter, and T. B. Bright, *Phys. Rev. Lett.*, **57**, 249 (1986).

Yon87 J. Yon, K. Barla, R. Herino, and G. Bomchil, *J. Appl. Phys.*, **62**, 1042 (1987).

Yon95 K. Yoneshige, H. Parks, S. Raghavan, J. Hiskey, and P. Resnick, *J. Electrochem. Soc.*, **142**, 671 (1995).

Zaz89 L. A. Zazzera and J. F. Moulder, *J. Electrochem. Soc.*, **136**, 484 (1989).

BIOGRAPHICAL SKETCH

Zhan Chen was born on the 14th day of November, 1973, in Dali, China. After completing his primary education in Dali, he attended the Chemistry Department at Peking University, Beijing, China, where he received his Bachelor of Science degree in July 1996. He entered graduate school at the University of Florida in January 1997 after he studied one semester at the Chemistry Department, North Carolina State University.

I certify that I have read this study and that in my opinion it conforms to acceptable standards of scholarly presentation and is fully adequate, in scope and quality, as a dissertation for the degree of Doctor of Philosophy.

Rajiv K. Singh, Chair
Professor of Materials
Science and Engineering

I certify that I have read this study and that in my opinion it conforms to acceptable standards of scholarly presentation and is fully adequate, in scope and quality, as a dissertation for the degree of Doctor of Philosophy.

Cammy R. Abernathy
Professor of Materials
Science and Engineering

I certify that I have read this study and that in my opinion it conforms to acceptable standards of scholarly presentation and is fully adequate, in scope and quality, as a dissertation for the degree of Doctor of Philosophy.

Hassan El-Shall
Engineer in Materials
Science and Engineering

I certify that I have read this study and that in my opinion it conforms to acceptable standards of scholarly presentation and is fully adequate, in scope and quality, as a dissertation for the degree of Doctor of Philosophy.

Stephen J. Pearton
Professor of Materials
Science and Engineering

I certify that I have read this study and that in my opinion it conforms to acceptable standards of scholarly presentation and is fully adequate, in scope and quality, as a dissertation for the degree of Doctor of Philosophy.

Dinesh O. Shah
Professor of Chemical Engineering

This dissertation was submitted to the Graduate Faculty of the College of Engineering and to the Graduate School and was accepted as partial fulfillment of the requirements for the degree of Doctor of Philosophy.

December 2000

M. J. Ohanian
Dean, College of Engineering

Winfred M. Phillips
Dean, Graduate School